UNIVERSITY OF SOUTHAMPTON

Tapered silicon core fibres for optical parametric amplification and wavelength conversion in the telecom band

thesis

in the

Faculty of Physics Sciences and Engineering
Optoelectronics Research Centre

by

Dong Wu

Supervisor Prof. Anna C. Peacock
Co-Supervisor: Dr. Harold M. H. Chong

May 2022

UNIVERSITY OF SOUTHAMPTON

ABSTRACT

Thesis for the degree of Doctor of Philosophy

by Dong Wu

Silicon waveguides have been investigated widely for nonlinear photonics because they have high nonlinear coefficients and can be fabricated with low cost. Among the different platforms for silicon waveguides, silicon core fibres show excellent nonlinear behaviour and also offer potential for seamless integration with other fibre-based devices. In this thesis, silicon fibres with polycrystalline core materials were fabricated via a conventional molten core drawing method. To obtain high nonlinearity, the polysilicon core fibres were subsequently tapered down to have small sub-micron metre core diameters (800 nm to 1.5 μm) and low transmission losses less than 3 dB/cm. After optimisation of the two-step tapering method, several polysilicon core fibres were characterised. Firstly, two submicron sized silicon core fibres with different waist lengths were tapered using the optimized method. Broad-band wavelength conversion using a continuous wave pump in the telecom band was realized, with a bandwidth covering from the S- to L- band, and conversion efficiencies of -30 dB. Then, another silicon core fibre with its dispersion engineered for optical parametric amplification based on four wave mixing was obtained. An optical on-off parametric gain of up to 9 dB was demonstrated, which we believe is the largest parametric gain observed in any crystalline silicon waveguide when using a telecom pulsed pump source. Moreover, 20Gb/s QPSK signals at both the C- and L- band have been successfully converted with the power penalties at a BER of 3.8 $\times 10^{-3}$ less than 1 dB. These results highlight the potential of silicon core fibres for use in nonlinear signal processing within future telecommunication systems.

Contents

List of Figures

List of Tables

Declaration of Authorship

I declare that this thesis and the work presented in it is my own and has been generated by me as the result of my own original research.

I confirm that:

1. This work was done wholly or mainly while in candidature for a research degree at this University;
2. Where any part of this thesis has previously been submitted for a degree or any other qualification at this University or any other institution, this has been clearly stated;
3. Where I have consulted the published work of others, this is always clearly attributed;
4. Where I have quoted from the work of others, the source is always given. With the exception of such quotations, this thesis is entirely my own work;
5. I have acknowledged all main sources of help;
6. Where the thesis is based on work done by myself jointly with others, I have made clear exactly what was done by others and what I have contributed myself;
7. Parts of this work have been published as: See List of Publications.

Signed:..... Date:.....

Acknowledgements

Throughout these years of study, I have received an enormous amount of support and assistance. I would firstly like to thank my supervisors, Dr. Harold M.H. Chong and especially Prof. Anna C. Peacock, whose expertise was invaluable in the research field. Your insightful feedbacks pushed me to sharpen my thinking and brought my work to a higher level.

I would like to acknowledge my colleagues, Dr. Haonan Ren, Dr. Joseph Campling, and Dr. Ozan Aktas, for their wonderful collaboration. I would particularly like to single out Dr. Li Shen. I want to thank you for your patient support and for all of the guidance in furthering my research. I would also like to thank Dr. Peter Shardlow, who gave me enormous assistance with my experimental work in his lab and responded to my request quickly.

I would like to thank my friends I met during my first year in Southampton, Dr. Fayong Liu, Dr. Fei He, Dr. Yongxin Chen, and Dr. Xiaoqing Zhang. They supported me immensely by providing a lovely warm house, which eliminated my fears of living in a strange country to help me get familiar with all my surroundings quickly.

I would also like to thank my friends, who I have known for seven years, Dr. Qiang Fu and Zijian Xu. They are the sweetest couple with kind hearts. They always supported me and stood by me with their great deal of love and care.

I would like to thank my friends, Dr. Xingxuan Zuo, Dr. Peipei Chen, Dr. Meng Ding, Dr. Jie Xu, Yue Zhang, and Dr. Yanli Qi, for their friendly and warm support of my life in the UK. You were always patient in listening to me so that I could come for advice anytime I needed it and particularly when I encountered difficulties in front of the puzzling cross of my life.

I would also like to thank all the other people I have met in ORC and UK for their kindness in making me always feel warm.

Finally, I would like to thank my parents, Mr. Xiaoping Wu and Mrs. Qingxiu Liu, and my young brother Hao Wu, for their unconditional love, understanding, and steady support back in China. Without them, I wouldn't have gone this far in pursuing my degree all these years.

Definitions and Abbreviations

A-Si	Amorphous Silicon
A-Si:H	Hydrogenated Amorphous Silicon
BPSK	Binary Phase Shift Keying
BER	Bit Error Rate
BPF	Band-Pass Filter
CaO	Calcium Oxide
CE	Conversion Efficiency
c-Si	Crystalline Silicon
CW	Continous Wave
EDFA	Erbium-Doped Fibre Amplifier
FCA	Free Carrier Absorption
FWHM	Full Width Half Maximum
FWM	Four-Wave Mixing
FOD	Fourth Order Dispersion
GVD	Group Velocity Dispersion
GNLSE	Generalised Nonlinear Schrödinger Equation
HPCVD	High Pressure Chemical Vapor Deposition
MCD	Molten Core Drawing
NA	Numerical Aperture
OC	Optical Coupler
OL	Objective Lens
OOK	On-Off Keying
OPA	Optical Parametric Amplification
OSA	Optical Spectrum Analyser

PC	Polarisation Controller
Poly-Si	Polycrystalline Silicon
QAM	Quadrature Amplitude Modulation
QPSK	Quadrature Phase-Shift Keying
RMS	Root Mean Square
SCF	Silicon Core Fibre
SMF	Single Mode Fibre
SOI	Silicon-On-Insulator
SPM	Self-Phase Modulation
SRS	Stimulated Raman Scattering
XPM	Cross-phase Modulation
TE	Transverse Mode
THG	Third-Harmonic Generation
TLF	Tapered Lensed Fibre
TPA	Two-Photon Absorption
ZDW	Zero Dispersion Wavelength

Chapter 1

Introduction

1.1 Nonlinear silicon photonics

Silicon photonics has gained increased interest owing to its unique possibilities to integrate optical components with electronic processors. Due to the large refractive index contrast between the silicon core and the silica cladding, light is well confined in silicon waveguides, leading to sub-micronmeter-sized photonic devices with ultra-small footprints [1]. Moreover, silicon has a large third-order nonlinearity, which makes it an excellent material for nonlinear photonics. Hence, nonlinear effects have been studied extensively in silicon waveguides, including self-phase modulation (SPM), two-photon absorption (TPA), cross-phase modulation (XPM), third-harmonic generation (THG), four-wave mixing (FWM) and stimulated Raman scattering (SRS) [2].

Based on these effects, a large number of nonlinear applications in silicon waveguides have been demonstrated. For example, the spectral broadening caused by SPM has been investigated [3] and all optical regeneration has been realized [4]. Cross-TPA modulation has been exploited to achieve all-optical switching [5]. FWM in silicon waveguides has been used to generate new frequencies through photon mixing, which can be exploited for applications ranging from optical parametric amplification (OPA) [6–9], wavelength conversion [10–12], optical regeneration of telecommunication signals [13,14] and more recently quantum signal processing [15,16]. Silicon also has a high Raman gain coefficient, and SRS has been investigated for the development of Raman lasers [17,18], which opens a route for all-silicon-based light sources [19]. Finally, the most extreme nonlinear process of supercontinuum generation has also been widely studied in silicon waveguides from the telecoms band into the mid-infared [8,20–22].

1.1.1 FWM-based wavelength conversion at telecom bands

One of the domain above-mentioned nonlinear applications on silicon photonics is wavelength conversion for all-optical signal processing. Over the past decade, high-performance FWM-based wavelength conversion has been studied extensively, as FWM can be used to modulate or switch high-speed and complex data format signals within silicon waveguides [2,23]. The first FWM-based wavelength conversion using a continuous wave pump in the telecom band was demonstrated in 2005, where a 1.58-cm-long waveguide made from the silicon-on-isolator (SOI) platform was used. The waveguide had linear losses of about 2.4 dB/cm and the maximum conversion efficiency of -35 dB was achieved with the input pump power of 8 dBm [6].

As high-performance FWM requires phase matching of the pump, signal and idler beams, one of the methods to optimize the process is dispersion engineering. By comparing the designs of different SOIs, a bandwidth of 150 nm and peak conversion efficiency of -9.6 dB, with the coupled input pump power of 20 dBm, was realized using a 1.8-cm-long SOI wire waveguide, with a width of 600 nm and height of 300 nm. For these dimensions, the telecom pump wavelength was in the anomalous dispersion region of the SOI waveguide, where the FWM conversion efficiencies are strong [24]. Moreover, by using a rib waveguide structure, the group velocity dispersion (GVD) was placed closer to centre of the telecom C-band wavelengths, enabling broad bandwidth conversion, as seen in the Ref [10]. A silicon rib waveguide was fabricated with a slab of 30 nm, a height of 300 nm and a width of 700 nm. The wavelength conversion reached over $\sim$ 800 nm bandwidth and the maximum obtained conversion efficiency was -18 dB.

Another main limitation of high-performance FWM is the nonlinear losses in silicon, because the telecom band is located where nonlinear losses due to TPA, and TPA-induced free carrier absorption (FCA), is large when high pump powers are applied. An approach to mitigate this is to pump SOIs with ultra-fast pulses, as when the time of the accumulation of the free carriers is longer than the pulse duration, the free carriers absorption gets suppressed [25]. By using a 17-mm-long SOI waveguide, a pulsed pump source with the repetition rate of 70 MHz and width of 3.5 ps, an on/off parametric gain of 5.2 dB was reported in the telecom band with negligible nonlinear absorption [9]. Moreover, it was also demonstrated that reversing biased p-i-n junctions on SOI waveguides help to sweep away the free carriers, thus reducing the nonlinear losses and allowing higher input pump powers for obtaining large conversion efficiency [26]. A conversion efficiency of -8.5 dB was reported using a SOI p-i-n waveguide with a length of 8 cm and continuous wave pumping at 25 dBm [27].

Solutions to obtain high-performance FWM also investigated the use of hydrogenated amorphous silicon (a-Si:H) waveguides and silicon nitride waveguides, as these silicon-based materials have a wider band gap than crystalline silicon, so that pump wavelengths in the telecom bands ($\lambda \sim 1.5\mu$m) are below the TPA absorption edge. For example, a

1.1-cm-long hydrogenated amorphous silicon waveguide with a width of 500 nm and the thickness of 300 nm was used for FWM-based OPA [8]. The obtained parametric gain was 26.5 dB using a pulsed pump at 1.54 μm with a repetition rate of 10 MHz and pulse width of 3.8 ps. Higher parametric gain was achieved using a silicon nitride waveguide with a width of 550 nm, a height of 300 nm and a length of 7 mm [28], as there is no TPA at wavelength of 1550 nm due to its large band gap. By using a pulsed-pump at 1.56 μm with a duration of the 500 fs and repetition rate of 20 MHz, a parametric gain of 42.5 dB was obtained, which represents the largest optical parametric gain to date on a silicon-based platform.

Meanwhile, the FWM-based wavelength conversion on these SOI platforms has been successfully applied for practical signal processing into high speed and high capacity systems. By converting the modulated signals to available bandwidths, the most early demonstrations of optical signal processing in silicon waveguides started vis using on-off keying (OOK) modulation formats [13,27]. As demonstrated in [13], a 17-mm-long SOI wire was used and the authors realized the conversion of 10 Gb/s OOK signals using a low pump power of 18.8 dBm. Complex signals modulation has also been widely reported using SOI platforms to increase the transmission capacity and spectral efficiency in the communication systems [29–35]. The modulation of quadrature amplitude modulation(QAM) single polarization (112 Gb/s) signals were presented in silicon waveguides with 22 Gbauds [31] and 28 Gbauds [32]. In 2016, in a 1-mm-long amorphous silicon waveguide, the binary phase shift keying (BPSK) and quadrature phase-shift keying (QPSK) signals, at the bit rate of 20 Gb/s, were demonstrated and the maximum obtained conversion efficiency of FWM-based wavelength conversion was -26 dB with the pump power of 18.5 dBm [34].

1.2 Silicon core fibres

All these above-mentioned planar-based silicon waveguides using high nonlinear materials like silicon and silicon-nitride offer combined advantages in nonlinear applications such as small device footprints and lower power thresholds owing to its high nonlinearity [9,13,36]. However, there are ongoing challenges to integrating these waveguides and materials with standard fibre components and commonly employed fibre laser sources. For signal processing devices used in practical fibre-based telecom systems, the nonlinear platform must exhibit key features including stability, low cost and compatibility with standard fibre components and pump sources. Thus, by combining the benefits of the highly nonlinear silicon materials and the flexible fibre geometry, a fiberized silicon waveguide platform would be highly advantageous in providing high-performance FWM and efficient fibre integration [37].

1.2.1 Fabrication of SCFs

Dated back to 1996, the first silicon core fibre (SCF) with a silica cladding was successfully grown using the micro pulling down technique [38]. The molten silicon was suspended above the seed crystal within a silica chamber through a graphite crucible which controls the diameter of the drawn fibre. Argon gas was flushed through to prevent oxidation of the silicon. The 15-cm-long single crystal SCF was then fabricated with core diameters ranging from 200 μm to 1.0 mm with growth rates of 0.1 to 5.0 mm/min. However, these early drawn SCFs didn't guide light due to defects such as the dislocations and stacking faults.

In 2006, another method of high pressure chemical vapour deposition (HPCVD) was presented for fabricating the SCFs [39]. By applying high temperatures and high pressures, the silicon can be deposited into the holes of the microstructured optical fibres, which act as the silica cladding. As the precursor silane decomposes, silicon gets conformally deposited on the inside of the smooth walls of the MOFs. The HPCVD method can be used to produce centimetre length silicon fibres with the core diameters varying from less than 1 μm up to 10 μm. The first SCF produced via this method had polycrystalline silicon core and estimated linear losses of 7 dB/cm at 1.5 μm. After the initial work, it was found that the phase of the silicon core could be controlled using the HPCVD method by adjusting the temperature, with amorphous materials deposited at low temperatures and crystalline materials at higher temperatures [40]. In 2010, a hydrogenated amorphous silicon (a-Si:H) core fibre was fabricated at a deposition temperature of ~400°C [41] with the linear losses of 5 dB/cm at 1.55 μm [41]. The incorporation of hydrogen into amorphous silicon core helps to saturate the dangling bonds, thus reducing the losses at telecom bands [42]. The linear losses of these hydrogenated amorphous silicon core fibres were then reported to get reduced to 3 dB/cm [43] by increasing the hydrogen content in the amorphous silicon core. However, the HPCVD method is a time-consuming fabrication procedure that produces fibres with only few centimetres long.

In 2008, another approach, the molten core drawing (MCD) method, was introduced that made use of traditional fibre drawing towers for fabricating the SCFs over long lengths [44]. The preforms are produced by sleeving a silicon rod with the diameter of 3 mm into a silica tube that has the inner diameter of 3.5 mm and the outer diameter of 5 mm. The formed preform then gets melted in a furnace and drawn down to form fibres with a silicon core at the temperature of 1950°C [45]. The temperature was chosen to soften the silica cladding , while still encapsulating the molten silicon core. The initial fabricated SCF were ~30 m long with core diameters between 60 μm and 120 μm, with the cladding diameters ranging from 1 mm to 2 mm. Then in 2009, smaller SCFs with core diameters between 10-100 μm and cladding diameters of 40-240 μm were fabricated by the power-in-tube preform [46]. After that, demonstrations about factors that influence the crystallinity for the silicon core were also studied. They included

studies of the surface roughness [47], the core geometry [48], the grain boundaries, cracks, longitudinal perturbations, the oxide precipitates [49]. Afterwards, in 2013, alkaline oxides were reported for use as interface modifiers, which provides great flexibility to draw small cores silicon fibres [50]. The interface modifiers act to prevent oxygen from diffusing into the silicon core, relieve the thermal mismatch between the core/cladding materials, as well as decrease the viscosity of the boundary between the silicon core and the silica cladding [50]. Among all the alkaline oxides studied, CaO and MgO showed the best performance of improving the uniformity and mechanical properties of the silicon core, and decreasing the defect rate. However, it was shown that due to the significantly different thermal properties of the silicon core and silica cladding, high temperatures can lead to break-up of the core due to Rayleigh instabilities [51], and made it difficult to produce as-drawn SCFs with the core sizes less than $\sim 10\,\mu$m.

Unfortunately, such large cores diameters are not ideal for nonlinear applications. Thus, to address this, post processing methods were introduced to reduce the SCF core sizes such as fibre tapering. Importantly, tapering has the benefits of both decreasing the core diameters and improving the crystallinity of the as-drawn SCFs. A fusion splicer was used to taper an a-Si:H fibre fabricated via the HPCVD method to produced the first SCF with a tapered sub-micron core [52]. Then in 2016, the first polysilicon core fibre fabricated by MCD method was tapered using a filament method, to produce a fire with linear losses of 3.5 dB/cm and a core diameter around $1\,\mu$m [53]. Although the core material was still polysilicon, based on the crystallographic study, it was confirmed that the tapering method can help to reduce the linear losses by increasing the single crystal grain sizes in the micron-sized tapered waist [54]. More recently this process has been improved further to fabricate tapered MCD SCFs with core diameters of $\sim 3\,\mu$m and lengths of 1 cm with linear losses of $\sim$1 to 2.5 dB/cm over the wavelength region from $1.55\,\mu$m to $2.5\,\mu$m [55]. Detailed investigations of the nonlinear parameters have been undertaken in the SCFs, which have revealed that the silicon core retains high Kerr nonlinear parameters consistent with those of planar crystalline silicon waveguides [55].

1.2.2 Recent progress on the application in SCFs

Based on its linear properties, silicon core fibres have been demonstrated for various applications in optoelectronics and photonics. For example, the first all-fibre highly sensitive Fabry–Perot interferometer (FPI) based on the SCF platform was proposed with the ability to provide the extinction ratio of 14 dB and free spectral range of 9.34 nm [56]. The FPI was formed by splicing a standard single mode fibre (SMF) with a SCF of the $34\,\mu$m core size and $125\,\mu$m cladding diameter. The deformation region between the SMF and the SCF was measured to be $38\,\mu$m long. Then in 2019, the fabrication of nano-spikes couplers onto the end facets of the tapered SCFs was achieved for the seamless integration with SMFs. With the cladding diameter of $30\,\mu$m, the nano-spike coupling

losses were measured to be ∼4 dB, which is significantly less than the corresponding free space coupling loss [57]. Bragg gratings have also been written into SCFs successfully using a 517 nm femtosecond laser with the observation of grating reflectivity and stress relieve in the core material [58]. Solar cells have also been fabricated using SCFs produced via the MCD method [59–61]. Finally, silicon Schottky photo detectors (SSPD) have been demonstrated in SCFs at telecom regimes with comparable photo-detection characteristics to the conventional SSPD [62].

In regards to the nonlinear optical applications, the micron-sized SCFs, combined with the high nonlinearity in the silicon core, have also performed well. In 2010, using an a-Si:H fibre with a core diameter of 5.6 μm and linear losses of 1.7 dB/cm at 1.54 μm, the nonlinear transmission was firstly characterised by studying the SPM [43,63]. All-optical modulation scheme that made use of TPA when pumped telecom bands on the same platform was reported [64]. The achieved extinction ratio was more than 4 dB, which indicates the possibilities of the SCFs for high speed signal processing applications. After that, the XPM with an extinction ratio of 12 dB was demonstrated at telecom bands [65]. In 2015, the first micro-spherical resonator using the silicon core fibre platform was fabricated and Kerr-based all-optical modulation was reported using a femtosecond pump pulse, with an obtained extinction ratio of 5.9 dB [66].

In addition to these demonstrations, numerical simulations of tapered SCFs with submicron sizes have been carried out to study parabolic pulse generation [67], soliton propagation [68] and soliton compression [69]. Motivated by this success, experimental FWM and octave-spanning supercontinuum generation (1.64-3.37 μm) was demonstrated by pumping in the mid-infared in 2014, using a 4-mm-long, a-Si:H fibre with a core diameter of 1.7 μm [70]. This work was further extended in 2019, where the generation of a mid-infared supercontinuum spectra, spanning almost two octaves (1.6 μm-5.3 μm) was demonstrated, by employing a novel designed tapered SCF with a core diameter waist of 2.8 μm.

1.3 Motivation of this thesis

As an emerging platform, SCFs combine the benefits of silicon materials and the excellent waveguide properties of the fibre geometry. Thus they offer the potential for realizing efficient all-optical signal processing in compact and robust geometries. Moreover, these SCFs can be produced via a standard fibre drawing procedure, allowing for the rapid production of long lengths of material, significantly reducing costs. Post-processing treatments can also be applied to improve the core material quality for obtaining low loss SCFs and to tailor the core dimensions down to submicron sizes. The ability to control the core size through tapering offers two key benefits. Firstly, it provides a route to engineer the dispersion in the SCFs, which is critical for achieving high-performance

FWM-based wavelength conversion. Secondly, it can be used to tailor the mode properties to improve coupling with conventional fibre components and lasers. With the development of the fabrication techniques for the SCFs, numerous nonlinear applications have been demonstrated. However, prior to the work in this thesis, there had been very few studies of the FWM performance and FWM-based signal processing using SCFs due to challenges in achieving phase-matching.

The work presented here makes use of the above-mentioned tapered SCF platform for demonstrations of FWM-based wavelength conversion and optical parametric amplification. The first focus of this thesis is to obtain low losses, and small core SCFs. As demonstrated in the prior art, linear losses below 3 dB/cm are typically sufficient to show good performance in nonlinear applications and so this formed the target for my work. The second focus is on reducing the core diameter to sub-micron sizes required to obtain small effective mode areas for high efficiency nonlinear processing at telecom band wavelengths. Obtaining small cores is also beneficial to achieving the dispersion profiles required for high gain and wide bandwidth FWM processes. Thus, the ultimate goal is to produce low loss, small core tapered SCFs for the observations of FWM-based wavelength conversion and parametric amplifications. Based on the studies of the FWM behaviours of these SCFs, the research in FWM-based modulated signal processing will pave the way for applying the SCFs into all-optical signal processing system.

1.4 The structure of this thesis

Chapter 2 briefly introduces the background theory. First, the waveguide characteristics are introduced, such as the waveguide structures, mode properties, propagation losses. This is followed by a discussion on the material properties of the different silicon forms, amorphous silicon (a-Si), crystalline silicon (c-Si) and polycrystalline silicon (poly-Si). The dispersion properties and the nonlinear processes used in this thesis are explained, including TPA, SPM and FWM. In the end, the generalised nonlinear Schrödinger equation (GNLSE) used to study nonlinear propagation is presented, together with the split step Fourier method that is used to solve it.

Chapter 3 describes the fabrication and tapering post-processing procedure used to produce the small core SCFs. The MCD method for producing the as-drawn SCFs in this thesis is first introduced. The focus then switches to describing tapering via a filament method to decrease the fibre core size to sub-micron. The tapering method and related tapering parameters are introduced. The measurements of the linear losses and the nonlinear losses are described and the estimation of the nonlinear refractive index and TPA parameter are provided via a comparison with simulations. At last, the procedures for optimizing the tapering process for obtaining sub-micron core SCFs are introduced. It starts with the two-step tapering method for reducing the core size below

a few microns. The related recipes used for the two-step tapering are given. Then the double clad method is explained in order to further increase the cladding/core ratio, with details for the used recipes.

Chapter 4 presents results of FWM-based wavelength conversion using a continuous wave pump in the tapered SCFs. The impact of the SCF profile on the wavelength conversion is discussed. Then, the role of the length dependence on the bandwidth and the maximum conversion efficiency is studied, using two tapered SCFs with the same design but different waist lengths. Furthermore, a tapered SCF is produced with the longest waist length to date, to enhance the conversion efficiency with lower pump powers. As FCA is observed with high input pump powers, the explanation of the FCA in SCFs when using a continuous wave pump is briefly described using numerical simulations.

Chapter 5 focuses on FWM-based optical parametric amplification in the tapered SCFs using a pulsed pump. Firstly, the FWM is characterized together with simulations to describe this parametric amplification process. With the introduction of the coupled wave equations for four-wave mixing, numerical simulations were conducted to study the impact of free carrier absorption on the parametric gain as a function of the pulsed pump parameters. Next, a low-loss dispersion engineered SCF is designed for FWM-based OPA, using the chosen pulsed pump parameters. Finally, the experimental results are compared with the simulations to determine the performance of the tapered SCFs for OPA.

Chapter 6 demonstrates the realization of all-optical signal processing of 20 Gb/s QPSK signals using a tapered SCF. It starts with the characterization of the FWM behaviours with the continuous pump. Then the quality of the wavelength conversion is discussed, using the constellation diagrams and the bit error rate (BER) measurements. Next, the fabrication method to achieve SCFs with nano-spike couplers is also briefly explained.

Chapter 7 concludes the work conducted in this thesis and discusses potential avenues for future work.

Chapter 2

Background

In this chapter, the background theory that supports work in the thesis is discussed. The waveguide structures and their basic properties, such as their mode characteristics and linear propagation losses, are introduced. To characterise the linear losses, the cut-back method is explained first. Secondly, the properties of amorphous silicon (a-Si), crystalline silicon (c-Si) and polycrystalline silicon (poly-Si) are discussed in relation to their optical applications. Thirdly, the dispersion properties are described, in which material dispersion and waveguide dispersion are explained. Fourthly, the nonlinear processes studied within this thesis are discussed, specifically two photon absorption (TPA), self-phase modulation (SPM) and four-wave mixing (FWM). Finally, the generalised nonlinear Schrödinger equation (GNLSE) for nonlinear propagation in a silicon waveguide is given. To solve the equations, the split step Fourier method is explained.

2.1 Waveguide characteristics

2.1.1 Waveguide structure

The silicon waveguides investigated in this report are formed within a fibre platform.

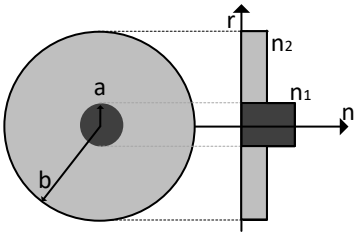

FIGURE 2.1: Schematic illustration of the cross-section and refractive index profile of silicon fibres

Silicon fibres have a cylindrically symmetric silicon core and silica cladding. The circular cross section can be seen in Figure 2.1, where a and b are the radius of the core and the cladding, respectively, and n_1 and n_2 are the refractive index of the core and the cladding, respectively. The difference between n_1 and n_2 allows for the confinement of light within the waveguides. Due to n_1 being higher than n_2, total internal reflection is realized at the core/cladding boundary. Therefore, light is guided in the waveguides cores.

The relative refractive index difference Δ between the core and the cladding is defined as [71]

$$\Delta = \frac{n_1^2 - n_2^2}{2n_1^2}. \tag{2.1}$$

The numerical aperture (NA) is denoted to define the light acceptance angle of the waveguides. NA is related to Δ by

$$NA = \sqrt{n_1^2 - n_2^2} \cong n_1\sqrt{2\Delta}. \tag{2.2}$$

Waveguides with large NA have large acceptance angles, within which injected light rays can propagate at discrete angles. The distributions of the electric field and magnetic field of these light rays are known as guided modes in waveguides. A normalised frequency V parameter determines the number of modes supported by the waveguide M, and is given as

$$V = \frac{2\pi a}{\lambda}\sqrt{(n_1^2 - n_2^2)}, \tag{2.3}$$

where λ is the wavelength of light. Normally, for a step-index waveguide, the condition for single-mode operation is $V \leq 2.405$. For step-index fibres with larger V number, the total guided mode number is approximated as

$$M \approx \frac{V^2}{2}. \tag{2.4}$$

The next section discusses about the mode properties in fibres.

2.1.2 Mode properties

Considering the fibre geometry, a cylindrical coordinate system with coordinates r, θ and z is chosen for detailed discussions about the guided modes. The electric field $\mathbf{E}$ and magnetic field $\mathbf{H}$ in an optical fibre are expressed as

$$\begin{aligned} \mathbf{E} &= \boldsymbol{E}(\boldsymbol{r}, \theta)e^{j(\omega t - \beta \boldsymbol{r})}, \\ \mathbf{H} &= \boldsymbol{H}(\boldsymbol{r}, \theta)e^{j(\omega t - \beta \boldsymbol{r})}, \end{aligned} \tag{2.5}$$

where ω is the angular frequency and β is the propagation constant. Derived from Maxwell's equations, the electric field $\boldsymbol{E}(\boldsymbol{r},\theta)$ and magnetic field $\boldsymbol{H}(\boldsymbol{r},\theta)$ are expressed as two independent components $E_z(r,\theta)$ and $H_z(r,\theta)$ by the two sets of wave equations [71], which are written as

$$\frac{\partial^2 E_z}{\partial r^2}+\frac{1}{r}\frac{\partial E_z}{\partial r}+\frac{1}{r^2}\frac{\partial^2 E_z}{\partial \theta^2}+\left[k^2 n\left(r,\theta\right)^2-\beta\left(\omega\right)^2\right]E_z=0, \tag{2.6}$$

$$\frac{\partial^2 H_z}{\partial r^2}+\frac{1}{r}\frac{\partial H_z}{\partial r}+\frac{1}{r^2}\frac{\partial^2 H_z}{\partial \theta^2}+\left[k^2 n\left(r,\theta\right)^2-\beta\left(\omega\right)^2\right]H_z=0, \tag{2.7}$$

where $\beta\left(\omega\right)$ is the propagation constant of the mode at an angular frequency ω in the z direction, r denotes the position in the plane transverse to the $z-$axis, $r=\left(x^2+y^2\right)^{1/2}$ in Cartesian coordinates and $n\left(r,\theta\right)$ is the refractive index of the waveguide. Using the method of separation of variables, the wave equation of the optical transverse electric field E_z has the solution

$$E_z=A\left(\omega\right)F\left(x,y\right)\exp\left(im\theta\right)\exp\left(i\beta\left(\omega\right)z\right), \tag{2.8}$$

where $F\left(x,y\right)$ describes the mode distribution, $A\left(\omega\right)$ is only dependent on ω and m is an integral. In step index cylindrical fibres, the refractive index in the core and cladding is uniform and the refractive index of the mode distribution is independent of θ, hence it can be simplified as $n(r)$, in which $n\left(r\right)=n_1$, for $r\leqslant a$ and $n\left(r\right)=n_2$, for $r>a$. Substituting Equation 2.8 into Equation 2.6, the general solutions of $F\left(x,y\right)$ of the electric field are the Bessel function $\boldsymbol{J}_m\left(pr\right)$ and the modified Bessel function $\boldsymbol{K}_m\left(qr\right)$, where p and q are defined as

$$\begin{aligned} p&=\sqrt{\left(n_1^2k^2-\beta^2\right)}, r\leqslant a\\ q&=\sqrt{\left(\beta^2-n_2^2k^2\right)}, r>a, \end{aligned} \tag{2.9}$$

where k is the wave number of free space and $k=\omega/c=2\pi/\lambda$. Then the solutions of $F\left(x,y\right)$ are expressed as

$$\begin{aligned} F\left(x,y\right)&=\boldsymbol{J}_m\left(pr\right), r\leqslant a\\ F\left(x,y\right)&=\boldsymbol{K}_m\left(qr\right), r>a. \end{aligned} \tag{2.10}$$

When the boundary condition that the tangential components of $\boldsymbol{E}$ and $\boldsymbol{H}$ are continuous across the core-cladding interface is satisfied, the eigenvalue equations, known as the dispersion equation, can be written as

$$\left[\frac{\boldsymbol{J}_m^{'}(pa)}{p\boldsymbol{J}_m^{'}(pa)}+\frac{\boldsymbol{K}_m^{'}(qa)}{q\boldsymbol{K}_m^{'}(qa)}\right]\left[\frac{\boldsymbol{J}_m^{'}(pa)}{p\boldsymbol{J}_m^{'}(pa)}+\frac{n_2^2}{n_1^2}\frac{\boldsymbol{K}_m^{'}(qa)}{q\boldsymbol{K}_m^{'}(qa)}\right]=\left(\frac{m\beta k(n_1^2-n_2^2)}{an_1p^2q^2}\right)^2, \tag{2.11}$$

where $F\left(x,y\right)$ is the m^{th}-order Bessel solution of the wave equations. For each m, the

eigenvalue equation provides n solutions for the propagation constantβ. Each β_{mn} corresponds to one mode with a field distribution. The indices m and n in β_{mn} represent the azimuthal mode number and the radial mode number, respectively. Detailed solutions can be found in [1,71,72]. In this thesis, only the propagation of the fundamental mode is discussed, because with careful input coupling, most of the power within the guided light is propagated in the fundamental mode [69].

For a single-mode fibre, only two modes of orthogonal polarizations with the same propagation constants are supported and are regarded as degenerate under ideal conditions. The notations HE_{mn} are customary used to describe the modes profiles within fibres. For the silicon core fibres, the notations LP_{mn}, as approximate solutions of Equation 2.11, can be used to describe the linearly polarized modes. To note, the fundamental mode HE_{11} corresponds to LP_{01}.

The propagation properties of each guided mode in a fibre can be well described by the effective refractive index n_{eff} and the effective mode area A_{eff}. The effective refractive index of the mode n_{eff} is defined as

$$n_{\mathrm{eff}} = \frac{\beta(\omega)}{k}. \tag{2.12}$$

The effective mode area A_{eff} is defined as

$$A_{\mathrm{eff}} = \frac{\left[\int_{-\infty}^{\infty}\int_{-\infty}^{\infty} \mid F(x,y) \mid^2 \mathrm{d}x\mathrm{d}y\right]^2}{\int_{-\infty}^{\infty}\int_{-\infty}^{\infty} \mid F(x,y) \mid^4 \mathrm{d}x\mathrm{d}y}. \tag{2.13}$$

As seen here, the effective mode area A_{eff} is related to the mode distribution. Hence, A_{eff} is dependent on the fibre dimensions and the refractive index of the core and the cladding. Especially in our silicon core fibres, A_{eff} is reduced in order to increase the intensities of the input pump power, thus enhancing the nonlinear effects and generally small because of the high index contrast between the silicon core and the silica cladding.

Using FDE (Finite Difference Eigenmodes), the analytical solutions of the eigenvalue equations can be obtained via modelling software such as Lumerical Mode Solutions. Figure 2.2 shows profiles of the fundamental mode, of which the electric field distributions are modelled using Lumerical Mode Solutions with $\lambda = 1550$ nm, $n_1 = 3.45$, $n_2 = 1.45$ and fibres with core diameter of $D = 500\,\mathrm{nm}$, $1.0\,\mu\mathrm{m}$ and $2.0\,\mu\mathrm{m}$. Considering that the light is well confined in these silicon cores within the cladding diameter of $20\,\mu\mathrm{m}$, larger cladding diameter doesn't change the mode properties for the wavelengths less than $2\,\mu\mathrm{m}$. In all cases the cladding diameter is set as of $20\,\mu\mathrm{m}$ (rather than the full $125\,\mu\mathrm{m}$) to make sure all the guided mode is captured whilst ensuring a high computation speed. Figure 2.3 shows the effective refractive indices (a) and mode areas of the fundamental mode (b), dependent on the core diameters with the wavelengths at $1.55\,\mu\mathrm{m}$ and $2\,\mu\mathrm{m}$. The refractive index values used for the silicon core and silica cladding are

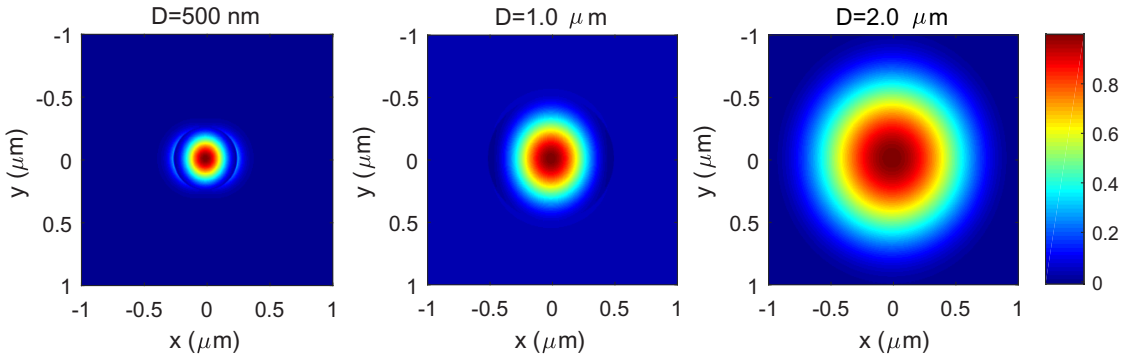

FIGURE 2.2: Fundamental mode profiles of silicon fibre of the core diameter D = 500 nm, 1.0 μm and 2.0 μm at the wavelength of 1.5 μm.

from Ref. [73]. As it is shown in Figure 2.2, the fundamental modes of the fibre core diameter for 1 μm and 2 μm are well confined in the silicon core. However, there are evanescent fields extending into the cladding of the fibre core diameter for 500 nm, which will cause radiated loss from the mode.

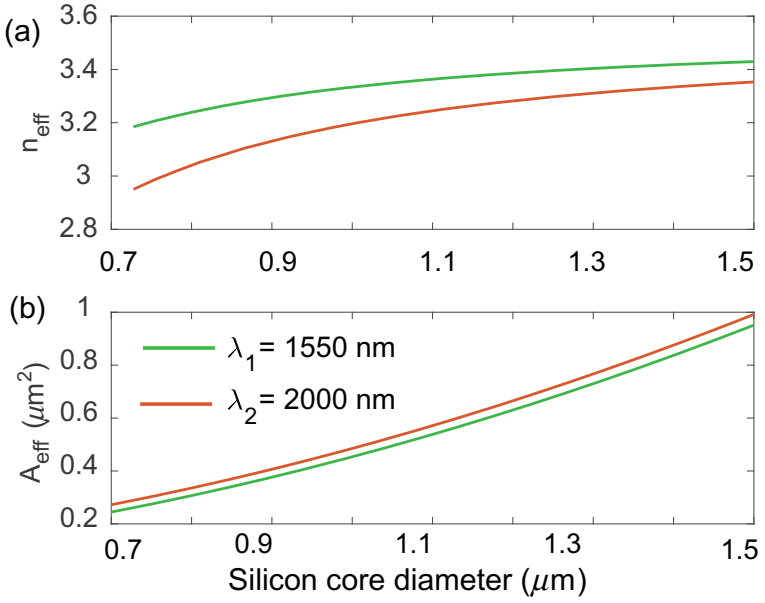

FIGURE 2.3: (a) Effective refractive index and (b) effective mode area as functions of core diameter at wavelengths of 1.55 μm and at 2 μm.

2.1.3 Optical pulses

To access the high peak powers needed to observe nonlinear effects, the pump beam normally consists of short pulses. A description of optical pulses is given as below. The approach in this thesis is simplified by only considering a single polarization component of the electric field along the fibre. The two main temporal profiles used to describe an optical pulse are Gaussian and hyperbolic secant. For the Gaussian form, the pulse

envelope $A(z,t)$ can be expressed as a Gaussian envelope with a phase $\phi(t)$

$$A(z,t) = \sqrt{P_0}\exp\left(-\frac{t^2}{2T_0^2}\right)\exp\left[i\phi(t)\right], \tag{2.14}$$

where P_0 is the peak optical power, T_0 is the pulse width at 1/e intensity point, which is related with the full width at the half maximum (FWHM) pulse width by $T_{\mathrm{FWHM}} \approx 1.665T_0$. Alternatively, for a hyperbolic secant, the pulse envelope can be expressed as

$$A(z,t) = \sqrt{P_0}\mathrm{sech}\left(\frac{t}{T_0}\right)\exp\left[i\phi(t)\right], \tag{2.15}$$

with $T_{\mathrm{FWHM}} \approx 1.763T_0$. The temporal optical field can also be expressed in the frequency domain through the Fourier transform $\mathscr{F}\{A(z,t)\}$ as

$$\tilde{A}(z,\omega) = \int_{-\infty}^{\infty} A(z,t)\exp(i\omega t)\,\mathrm{d}t. \tag{2.16}$$

2.1.4 Fibre losses

Loss describes the attenuation of light during transmission down a waveguide. In a silicon core fibre, there can be both linear losses and nonlinear losses, which originate from three sources: scattering, radiation and absorption [1]. Scattering losses in the silicon core fibres can result from the crystalline defects and dopants within the core, as well as roughness at the interface between the core and the cladding. Radiation loss occurs due to the leakage of the mode from the core into the cladding, which is usually negligible for silicon core fibres because of the tight mode confinement and the large core diameter. The absorption losses can be divided as linear losses and nonlinear losses. For the linear losses, it is mainly caused by the molecular vibrations and the rotations at long wavelength [74]. The nonlinear losses result from the band edge absorption and free carrier absorption at short wavelengths, when the transmitted light has an energy larger than the band gap. More details about the nonlinear losses can be found in Section 2.3.2. To analyse the losses, the definition of the losses are as follows. If the optical power of the input light is P_0, after transmission through a fibre of length L, the output power P_T is given by

$$P_T = P_0\mathrm{e}^{-\alpha_0 L}, \tag{2.17}$$

where the attenuation constant α_0, in units of m^{-1}, is used to describe losses for the waveguide. In general, the loss α is expressed in dB/m for silicon waveguides, and is related to α_0 as

$$\alpha = \frac{10}{L}\log\left(\frac{P_T}{P_0}\right) = 4.343\alpha_0, \tag{2.18}$$

where L is in units of m. To characterise the linear losses, the cutback method is commonly employed. While conducting the measurements, some additional losses occur. They are, for example, coupling losses, resulted from the mode mismatch between the

mode coming from the lens, and that from the fibre end facets, lens absorption losses, caused by the material absorption of the lens, and the Fresnel reflection losses of the fibre end facets. By comparing the optical transmission through a longer length of fibre to that of a shorter one, the cutback method can eliminate the influence of these additional losses. The schematic illustrations for fibres under the cutback method are shown in

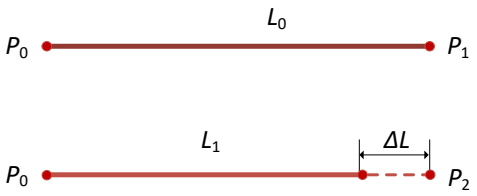

FIGURE 2.4: Cutback method for fibres.

Figure 2.4. The first step is to measure the single pass loss of the fibre as a whole length L_0 and record as α_{L_0}, to note here. At the second step, polish off a length of the fibre ΔL and repeat the loss measurement of the fibre of the second length L_1, obtaining another single pass losses of the fibre as α_{L_1}. For example, between two points, as seen in Figure 2.4, the linear propagation loss α_l (dB/cm) can be estimated as

$$\alpha_l = \frac{10}{\Delta L} \log\left(\frac{P_1}{P_2}\right), \tag{2.19}$$

where P_1 and P_2 are the output powers of the length L_0 and L_1, respectively, and ΔL is in unit of cm. Then, with several repeats of the second step, single pass losses α_n, where n denotes the n-th time of the cutback, with different lengths L_n under the similar experimental condition and materials are achieved. By fitting a curve to the plot of the measured losses $\alpha_{\mathrm{L_n}}$ versus length L_n, the linear losses can be calculated.

2.2 Dispersion

For a short optical pulse, dispersion is a critical parameter to take into consideration during propagation within a waveguide. It relates to the frequency dependence of the effective refractive index with a silicon waveguide. Specifically, dispersion combines both material dispersion and waveguide dispersion that is determined by the waveguide geometry. To describe dispersion within a waveguide, the mode propagation constant β can be expanded in a Taylor series expansions as

$$\beta(\omega) = \beta_0 + \beta_1(\omega - \omega_0) + \frac{1}{2}\beta_2(\omega - \omega_0)^2 + \frac{1}{6}\beta_3(\omega - \omega_0)^3 \cdots + \frac{1}{m!}\beta_m(\omega - \omega_0)^m + \cdots, \tag{2.20}$$

where β_m represents the m-th order dispersion and is denoted as

$$\beta_m = \left(\frac{d^m \beta}{d\omega^m}\right)_{(w=\omega_0)} \quad (m = 0, 1, 2 \cdots) \tag{2.21}$$

β_1 is related to the group velocity v_g, which represents the speed of the phase envelope and is expressed as

$$\beta_1 = \frac{1}{v_g}. \tag{2.22}$$

β_2 is referred as the group-velocity dispersion (GVD) which causes the pulse to spread in time. The dispersion parameter D is related to β_2 as

$$D = -\frac{2\pi c}{\lambda^2}\beta_2. \tag{2.23}$$

In general, the magnitudes of higher order dispersion (β_3, $\beta_4 \cdots$) are much smaller than β_2, hence β_2 is commonly regarded as the main dispersion element. Only when the pump wavelength is near the zero dispersion wavelength, or when the pulse spectral bandwidth is very large, the orders of dispersion higher than β_2, such as β_3 and β_4 need to be considered.

2.2.1 Material dispersion

Currently, there are three different phases of silicon used in silicon waveguides. They are polycrystalline silicon, amorphous silicon and single crystalline silicon. The refractive indices of these materials vary from 3.4 to 3.6 at the wavelength of 1.55 μm, depending on the composition, deposition temperature, and the material structure. Three forms

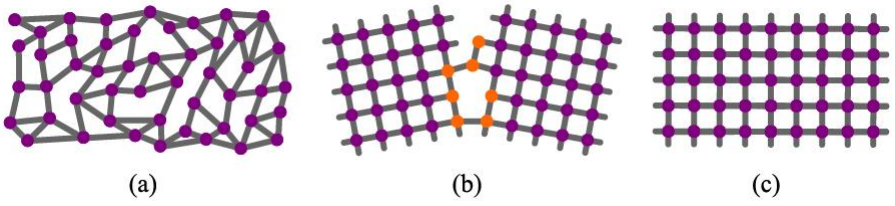

FIGURE 2.5: Schematic illustration of three types of silicon [75], a-Si, poly-Si and c-Si.

of silicon are represented in Figure 2.5, from amorphous silicon, polysilicon to single crystalline silicon. Figure 2.5(a) represents the amorphous silicon structure, of which the bonds between the silicon atoms are randomly arranged. Figure 2.5(c) is crystalline silicon, where the atoms are aligned regularly and Si-Si bond is fully connected. Figure 2.5(b) is the structure of poly crystalline silicon, which consists of single crystal grains held together by an amorphous network. Crystalline silicon has excellent optical and electronic properties, offering great electron mobility and low optical transmission losses.

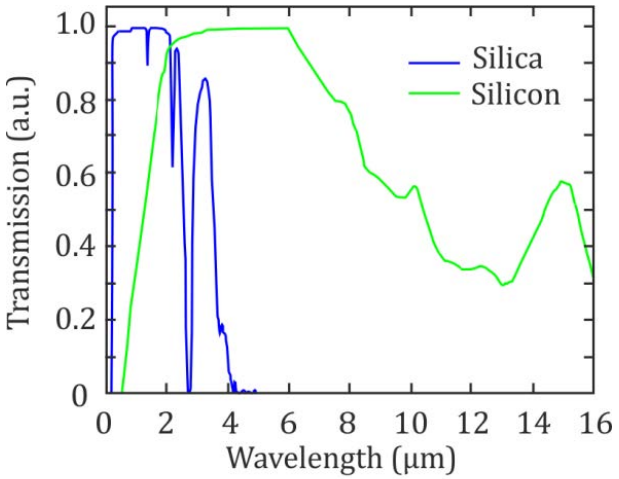

FIGURE 2.6: Transmission properties of c-Si (green curve) and fused silica (blue curve) [76].

As mentioned previously, the silicon core fibres can only be produced with a-Si cores or poly-Si cores. Based on the MCD method, poly-Si core fibres can be produced with long lengths that are suitable for post-processing. The focus of this work is poly-Si core fibres and their transparency covers 1.1 μm to 7 μm, as seen the green curve in Figure 2.6. By making the grain sizes larger via post processing to reduce the scattering and absorption losses, the poly-Si core fibres can approach the optoelectronic properties, comparable to that of c-Si [53]. Thus, the standard refractive index in transmission window can be suitable for these post-processed poly-Si core fibres.

The material dispersion can be determined by the wavelength dependent refractive index through the Sellmeier equation [73]:

$$n^2(\lambda, T) = 1 + \sum_{i=1}^{3} \frac{S_i(T)\,\lambda^2}{\lambda^2 - \lambda_i^2(T)}, \tag{2.24}$$

where

$$S_i(T) = \sum_{j=0}^{4} S_{ij} T^j, \tag{2.25}$$

$$\lambda_i(T) = \sum_{j=0}^{4} \lambda_{ij} T^j. \tag{2.26}$$

$S_i(T)$ and $\lambda_i(T)$ are the oscillation strength and the wavelength of i-th resonance at temperature T. The sum in Equation 2.24 extends over all material resonances that contribute to the frequency range of interest. $S_i(T)$ and $\lambda_i(T)$ can be obtained experimentally by fitting the measured dispersion curve. Because the refractive index for polysilicon has not been well documented, Figure 2.7 plots the refractive index dependent on the wavelength for c-Si, using values as seen in [73]. These are a good approximation as the phase matching calculating will be shown in later sections.

	S_1	S_2	S_3	λ_1	λ_2	λ_3
T^0 term	10.4907	-1346.61	4.42827×10^{7}	0.299713	-3.51711×10^{6}	1.71400×10^{6}
T^1 term	2.08020×10^{-4}	29.1664	-1.76213×10^{6}	-1.14234×10^{-5}	42.3892	-1.44984×10^{5}
T^2 term	4.21694×10^{-6}	-0.278724	-7.61575×10^{4}	1.67134×10^{-7}	-0.357957	-6.90744×10^{3}
T^3 term	-5.82298×10^{-9}	1.05939×10^{-3}	678.414	-2.51049×10^{-10}	1.17504×10^{-3}	-39.3699
T^4 term	3.44688×10^{-12}	-1.35089×10^{-6}	103.243	2.32484×10^{-14}	-1.13212×10^{-6}	23.577

TABLE 2.1: Sellmeier coefficients for crystalline silicon from [73].

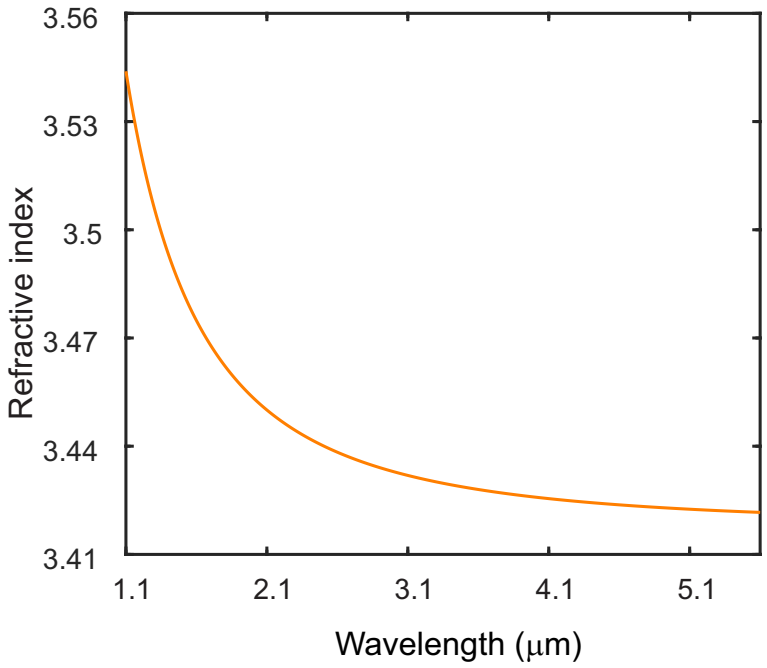

FIGURE 2.7: Refractive index of silicon as a function of wavelength at T= 295 K.

2.2.2 Waveguide dispersion

In step-index fibres, larger wavelengths of arbitrary distribution will have a broad field distribution and thus be less confined than the shorter wavelengths. This dependence of field distribution on wavelength leads to a perturbation in the effective refractive index, thereby modifying the propagation constant and engineering the waveguide dispersion.

As discussed in Section 2.1.2, calculations of β are determined by numerically solving the eigenvalue equations Equation 2.11. Each β relates to an optical fibre's dimensions and refractive indices at a given wavelength, for any mn mode. As an example, Figure 2.8 shows the calculated dispersion curves β_2 of the fundamental mode for different silicon core fibres with three core diameters D= 815 nm, 915 nm and 1015 nm, using Lumerical Mode Solutions. The most notable feature is that the wavelength at which β_2 passes from positive to negative values shifts to longer wavelengths for larger cores. That wavelength is referred to as the zero dispersion wavelength (ZDW) and denoted as λ_D, where λ_{D1}=1467 nm, λ_{D2}=1550 nm, λ_{D3}=1619 nm. As seen from Figure 2.8, if the value

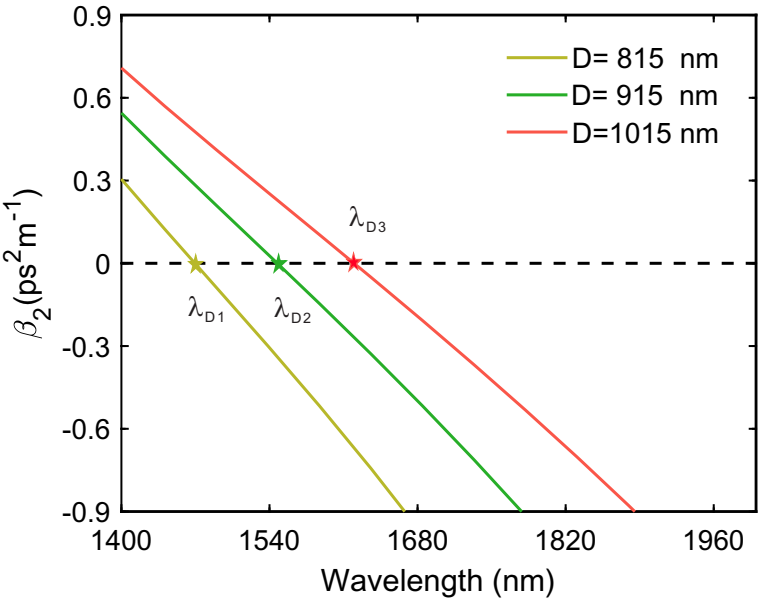

FIGURE 2.8: Simulated dispersion curves β_2 dependent on the wavelength for silicon fibres of different core diameters (D= 815 nm, 915 nm and 1015 nm).

of β_2 is positive and the fibre exhibits normal dispersion, the shorter wavelengths of an optical pulse travel slower than longer wavelengths. If the value of β_2 is negative, then the fibre exhibits the anomalous dispersion, where shorter wavelengths of an optical pulse travel faster than longer ones. If β_2 is close to or equals 0, higher order dispersion should be considered.

2.3 Waveguide nonlinearities

The polarization field P is the response of the electrons in the outer shells of the atoms in a material to the electric field E of incident optical signal. In silicon waveguides, the power density can remain very high, as the light is tightly confined due to the light core/cladding index contrast, which induces a strong nonlinear response in the polarization field P in time domain. This gives rise to several nonlinear effects. The induced polarization P is the contribution of the electric field E and the susceptibility χ and is expressed as

$$P = P_L + P_{NL} = \epsilon_0 \chi^{(1)} E + \epsilon_0 \left(\chi^{(2)} : EE + \chi^{(3)} \vdots EEE + ... \right), \tag{2.27}$$

where $\chi^{(n)}$ is the n-th order of the susceptibility and is a tensor of rank $(n+1)$ $\chi^{(1)}$ contributes to the linear polarization field P_L. Higher order susceptibilities contribute to the nonlinear polarization field P_{NL}. The second-order susceptibility $\chi^{(2)}$ contributes to second order nonlinear effects, such as second harmonic generation, and optical parametric oscillation and etc. For the centrosymmetric structures, such as silicon, $\chi^{(2)}$ is

absent and therefore the third-order susceptibility $\chi^{(3)}$ dominates the nonlinear effects of silicon waveguides. In this case, P_{NL} from Equation 2.27 can be simplified as

$$P_{NL} = \epsilon_0 \chi^{(3)} \vdots EEE. \tag{2.28}$$

Under conditions that the molecular vibrations caused by $\chi^{(3)}$ and third-harmonic frequency generation can be neglected, P_{NL} can be approximated by

$$P_{NL} = \epsilon_0 \epsilon_{\mathrm{NL}} E, \tag{2.29}$$

where ϵ_{NL} denotes the nonlinear contribution to the dielectric constant and is defined as

$$\epsilon_{\mathrm{NL}} = \frac{3}{4}\chi^{(3)} \mid E \mid^2 . \tag{2.30}$$

With the linear polarization, it is customary that the first order of susceptibility $\chi^{(1)}$ relates to the refractive index n and the absorption coefficient α by the relations as

$$n = 1 + \frac{1}{2}\mathrm{Re}\left[\chi^{(1)}\right], \tag{2.31}$$

$$\alpha = \frac{\omega}{nc}\mathrm{Im}\left[\chi^{(1)}\right]. \tag{2.32}$$

However, as derived from the nonlinear polarization with waveguides, the refractive index and the absorption coefficient become intensity dependent as

$$\tilde{n}_j = n + n_2 \mid E \mid^2, \tag{2.33}$$

$$\tilde{\alpha} = \alpha + \alpha_2 \mid E \mid^2, \tag{2.34}$$

where n_2 is the nonlinear refractive index and α_2 is the nonlinear absorption. In a simplified form and assuming the involved waves are linearly polarized along one same axis x, they are respectively given by

$$n_2 = \frac{1}{8n}\mathrm{Re}\left(\chi^{(3)}_{xxxx}\right), \tag{2.35}$$

$$\alpha_2 = \frac{3\omega}{4nc}\mathrm{Im}\left(\chi^{(3)}_{xxxx}\right). \tag{2.36}$$

2.3.1 Self phase modulation

In this section, the nonlinear effect of SPM is briefly discussed. SPM is related to the intensity dependence of the refractive index of material. It gives rise to spectral broadening of light pulses in frequency domain. When the light of intensity I propagates

in a waveguide, the refractive index n changes as

$$n\,(I) = n + n_2 \times I, \tag{2.37}$$

where n_2 follows from Equation 2.35, the temporal phase of the light changes with nonlinear refractive index as

$$\phi_{NL} = n_2 I k z. \tag{2.38}$$

It is worth noting that, on its own, the nonlinear phase shift doesn't affect the pulse shape in the temporal domain and it primarily manifests as a spectral broadening. By analysing the spectral broadening, we can estimate the nonlinear refractive index via solving NLSE and comparing the spectral profiles.

2.3.2 Nonlinear absorption

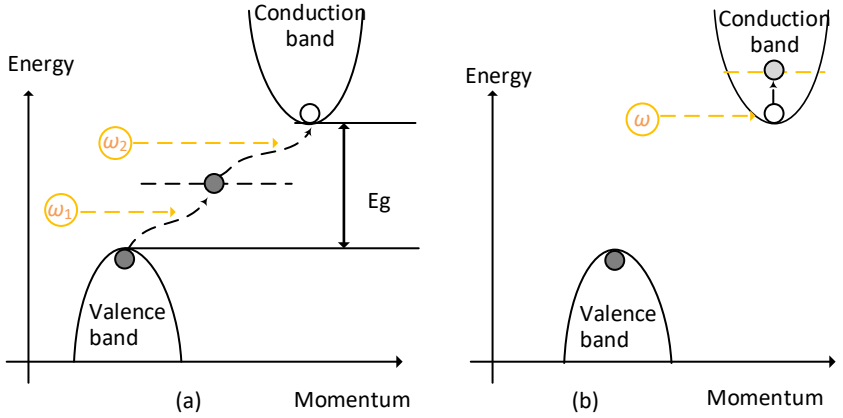

FIGURE 2.9: The diagrams of (a) TPA process and (b) FCA process .

In silicon waveguides, the main nonlinear absorption is TPA, which excites free carriers from the valence band to the conduction band if the sum of the energy of the two injected photons is larger than the band gap energy. The diagram of the TPA process is shown in Figure 2.9(a). These photons can have the same, or different energies, i.e., degenerate or non-degenerated TPA. The creation of a carrier in the conduction band is termed free carrier generation, and in turn this can cause free carrier absorption (FCA) of which the mechanism is shown in Figure 2.9(b). The TPA coefficient β_{TPA} describes the strength at which the pump light is depleted by this process, which is related to the third-order nonlinearity as

$$\beta_{\mathrm{TPA}} = \frac{3\omega}{2\varepsilon_0 c^2 n^2} \mathrm{Im}\left[\chi^{(3)}_{xxxx}\right], \tag{2.39}$$

where ε_0 is the vacuum electric permittivity. The band gap of silicon is around 1.12 eV, which corresponds to a wavelength of ~1.1 μm. β_{TPA} is related to α_2 with the relation of Equation 2.36. Combing the effects of n_2 and α_2, the third order nonlinearity γ is

introduced to describe the strength of nonlinear processes is determined by

$$\gamma = \frac{2\pi n_2}{\lambda A_{\text{eff}}} + \frac{i\beta_{\text{TPA}}}{2A_{\text{eff}}}. \tag{2.40}$$

2.3.3 Four wave mixing

Another important nonlinear effect is FWM, which involves the mixing of four waves with frequencies ω_1, ω_2, ω_3 and ω_4. The total scalar electric field of these four waves is written as

$$E = \sum_{j=1}^{4} E_j \exp\left[i\left(\beta_j z - \omega_j t\right)\right] + c.c.. \tag{2.41}$$

Substituting Equation 2.41 into Equation 2.29, the polarization field P_{NL} consists of four frequency components and is expressed as

$$P = \sum_{j=1}^{4} P_j \exp\left[i\left(\beta_j z - \omega_j t\right)\right] + c.c.. \tag{2.42}$$

For instance, the fourth term of the polarization field P_4 can be written as [72]

$$\begin{aligned} P_4 = \frac{3\epsilon_0}{4}\chi^{(3)}_{xxxx}\big[&\mid E_4 \mid^2 E_4 + 2\left(\mid E_1 \mid^2 + \mid E_2 \mid^2 + \mid E_3 \mid^2\right) E_4 \\ &+ \cdots 2E_1E_2E_3\exp\left(i\theta_+\right) + 2E_1E_2E_3^*\exp\left(i\theta_-\right)\big], \end{aligned} \tag{2.43}$$

where E_n is the electrical field of the wave of frequency ω_n, θ_+ and θ_- are phase mismatch parameters, which will be discussed in Section 2.3.3. Typically, the first term in Equation 2.43 is responsible for SPM and the other three terms containing E_4 are devoted to the XPM effects. The remaining terms contribute to the FWM process [2]. The strength of FWM conversion depends on the overlap between the waves, which all travel at different speeds, and thus phase matching considerations are critical.

2.3.3.1 Phase matching condition

The coupling efficiency of FWM depends on the phase mismatch, governed by θ_- and θ_+ in Equation 2.43. One of the requirements for significant FWM is the phase matching condition, which means either $\theta_- = 0$ or $\theta_+ = 0$. The phase mismatch parameters θ_- and θ_+ are defined as

$$\theta_+ = \left[\beta\left(\omega_1\right) + \beta\left(\omega_2\right) + \beta\left(\omega_3\right) - \beta\left(\omega_4\right)\right]z - \left(\omega_1 + \omega_2 + \omega_3 - \omega_4\right)t, \tag{2.44}$$

$$\theta_- = \left[\beta\left(\omega_1\right) + \beta\left(\omega_2\right) - \beta\left(\omega_3\right) - \beta\left(\omega_4\right)\right]z - \left(\omega_1 + \omega_2 - \omega_3 - \omega_4\right)t. \tag{2.45}$$

Two types of FWM usually operate in silicon waveguides. One concerning θ_+ is the case where the total energies of three photons at frequencies $\omega_1, \omega_2, \omega_3$ transfer to one photon

at the frequency ω_4. FWM of this type with high efficiency is challenging to achieve phase matching condition in silicon waveguides. The other one concerning θ_- is a more general case, where the sum of two photons with energies $\hbar\omega_1$ and $\hbar\omega_2$ get transferred to the other two photons, $\hbar\omega_3$ and $\hbar\omega_4$. In this case, the conservation of energy is satisfied and follows as

$$\omega_1 + \omega_2 = \omega_3 + \omega_4. \tag{2.46}$$

Substituting Equation 2.46 into Equation 2.45, the phase mismatch term Δk can be expressed as

$$\Delta k = \beta(\omega_3) + \beta(\omega_4) - \beta(\omega_1) - \beta(\omega_2). \tag{2.47}$$

When ω_1 equals ω_2, it is called degenerate FWM. The following description in this section will only focus on degenerate FWM as it is the main focus of the research in this thesis. In degenerate FWM, the involved three waves of the frequencies as ω_1, ω_3 and ω_4, are called the pump wave, signal wave and idler wave, respectively, which are denoted as ω_p, ω_s and ω_i in following context. It is noted that

$$\beta(\omega_j) = \tilde{n}_j \omega_j / c, \tag{2.48}$$

where $j = p, s, i$ and $\tilde{n}_j$ is the refractive index at frequency ω_j. Hence, substituting Equation 2.48 into Equation 2.47 and then to Equation 2.45, the phase match conditions can be realized by making $\theta_- = 0$, which is written as

$$2\omega_p = \omega_s + \omega_i, \tag{2.49}$$

$$\Delta k = [\tilde{n}(\omega_s)\omega_s + \tilde{n}(\omega_i)\omega_i - 2\tilde{n}(\omega_p)\omega_p]/c = 0. \tag{2.50}$$

Generally, Δk can be expressed in the form as

$$\Delta k = \Delta k_L + \Delta k_{NL}, \tag{2.51}$$

where Δk_L and Δk_{NL} are respectively, the linear phase mismatch term and the nonlinear phase mismatch term. Δk_L is caused by the dispersion in fibres, which can be expressed as

$$\Delta k_L = (n_s\omega_s + n_i\omega_i - 2n_p\omega_p)/c. \tag{2.52}$$

The frequency difference $\Delta\omega$ is defined as

$$\Delta\omega = |\omega_p - \omega_s| = |\omega_i - \omega_p|. \tag{2.53}$$

In terms of $\Delta\omega$, Δk_L can be expressed by using Equation 2.20 and Equation 2.48. By retaining the expression up to fourth-order terms in $\Delta\omega$, the even-order terms β_1 and

β_3 vanishes, and Δk_L is written as

$$\Delta k_L = \beta_2 \Delta\omega^2 + \beta_4 \Delta\omega^4/12. \tag{2.54}$$

Only considering the fundamental mode and without including the TPA the nonlinear phase mismatch Δk_{NL} is dominated by changes in the refractive index induced by the high power of the pump wave and is expressed as

$$\Delta k_{NL} = 2\gamma_p P_p, \tag{2.55}$$

where γ_p is the real part of the nonlinearity at pump wavelength and P_p is the pump power. Therefore, in FWM, the phase matching condition is satisfied when

$$\Delta k = \Delta k_L + \Delta k_{NL} = \beta_2 \Delta\omega^2 + \beta_4 \Delta\omega^4/12 + 2\gamma_p P_p = 0. \tag{2.56}$$

2.3.3.2 Dispersion engineering

Depending on the magnitudes and signs of β_2, β_4, various phase matching conditions in silicon waveguides can be obtained, which result in different conversion bandwidths [11, 24, 77, 78]. When the pump wavelength is close to the ZDW, and then FOD plays a role, the width of the phase-matching region is obtained from Equation 2.56

$$\Delta\omega = \frac{6}{|\beta_4|}\left(\sqrt{\beta_2^2 + 2|\beta_4|\gamma_p P_p/3} + \beta_2\right), \tag{2.57}$$

where β_2 and β_4 must be opposite in sign in the normal dispersion regime to compensate the positive γ. In the limit of $|\beta_4|\gamma P_p \ll \beta_2^2$, Equation 2.57 can be simplified as

$$\Delta\omega = \sqrt{\frac{12|\beta_2|}{|\beta_4|}}. \tag{2.58}$$

Similar to the nanophotonic silicon waveguides, the group velocity dispersion (GVD)β_2 of the SCFs can be controlled by reducing the core diameter so that the waveguide dispersion can compensate for the large normal material dispersion. For a fixed pump wavelength, the core diameter must be carefully engineered to access the desired dispersion regime and be close to the ZDW for the phase matching conditions.

The propagation constants β of SCFs for several core sizes across different wavelengths are firstly modulated using the Lumerical Mode Solutions. Then, β_2 and β_4 can be obtained via fitting β as a function of the wavelength using a poly-fit function in Matlab. Figure 2.10 shows the dispersion values for β_2 and β_4 at different wavelengths for SCFs with three core diameters (800 nm, 915 nm and 3 μm). From the calculated dispersion profiles shown in Figure 2.10, the SCF with a large core diameter of 3 μm would only exhibit large positive β_2 and the value of β_4 is negligible, which could not realize the

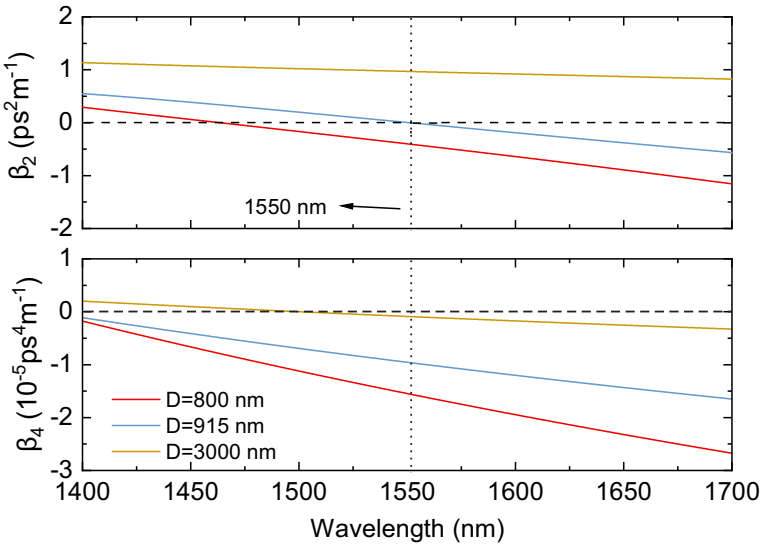

FIGURE 2.10: Calculated β_2 and β_4 dispersion as a function of wavelength for the SCF with different core diameters shown in the legend.

phase matching in the telecom band. For the two smaller cores, the one with 915 nm would exhibit a relatively broad bandwidth of the parametric gain, owing to its small β_2 and negative β_4, while the 800 nm core has a larger negative β_2. As evident from Equation 2.58, the dispersion combination for the 915 nm core permits broadband phase-matching from the pump at the wavelength of 1.55 μm with a conversion bandwidth of $\sim$ 380 nm, spanning almost the entire telecom window [10, 28, 77].

2.4 Pulse propagation

2.4.1 Generalised nonlinear Schrödinger equation

When propagating short pulses with widths ranging from 100 fs to 100 ps within a semiconductor waveguide, dispersion, nonlinear effects and loss can all act to change the pulse shape and spectral components. For our silicon core fibres, taking TPA and FCA into consideration, we define a GNLSE [79] as

$$\frac{\partial A}{\partial z} + \frac{i\beta_2}{2}\frac{\partial^2 A}{\partial t^2} - \frac{\beta_3}{6}\frac{\partial^3 A}{\partial t^3} + \frac{\alpha_l + \alpha_f}{2}A = i\gamma |A|^2 A, \tag{2.59}$$

where A is the slowly varying amplitude envelope of the electric field, z is the propagation distance of the light, t is the propagating time in a reference frame with the pulse , β_2 is the second-order dispersive coefficient, α_l is the linear loss of the fibre, α_f is the contribution of the free carriers [80]. The free carrier contribution α_f is given by

$$\alpha_f = \sigma (1 + i\mu) N_c, \tag{2.60}$$

where σ is the FCA coefficient and μ governs the free carrier dispersion. The number of generated free carriers N_c, is derived as

$$\frac{\partial N_c}{\partial t} = \frac{\beta_{\mathrm{TPA}}}{2h\nu_0} \frac{|A|^4}{A_{\mathrm{eff}}^2} - \frac{N_c}{\tau_c}, \tag{2.61}$$

where τ_c is the carrier life time, ν_0 is the central frequency, $\nu_0 = \omega/2\pi$ and h is the Plank's constant.

2.4.2 Split-step Fourier method

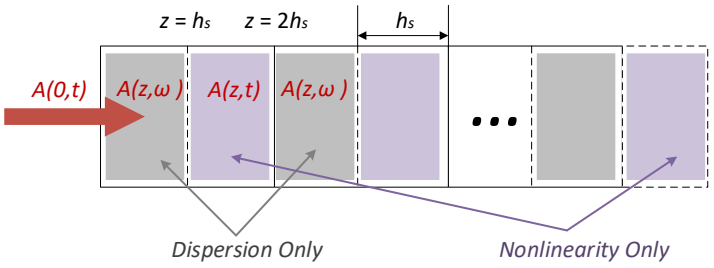

FIGURE 2.11: Schematic illustration of the split-step Fourier method for numerical simulations.

To solve the GNLSE, the split-step Fourier method is generally employed. The main idea is to assume that the propagation of the light happens in two separate steps, the dispersion only region and the nonlinear only region, as seen in Figure 2.11. Thus the equation can be numerically solved in split steps, by writing the GNLSE as

$$\frac{\partial A}{\partial z} = \left(\hat{D} + \hat{N}\right) A, \tag{2.62}$$

where $\hat{D}$ represents the dispersion and linear losses and $\hat{N}$ governs the nonlinear parts. These two operators are given by

$$\hat{D} = -\frac{i\beta_2}{2}\frac{\partial^2}{\partial t^2} + \frac{\beta_3}{6}\frac{\partial^3}{\partial t^3} - \frac{\alpha_l}{2}, \tag{2.63}$$

$$\hat{N} = \left(\frac{ikn_2}{A_{\mathrm{eff}}} - \frac{\beta_{\mathrm{TPA}}}{2A_{\mathrm{eff}}}\right) |A|^2 - \frac{\alpha_f}{2}. \tag{2.64}$$

In the nonlinearity only region, we can assume $\hat{D} = 0$ in Equation 2.62. Then in the second dispersion only step, it can be assumed $\hat{N} = 0$. The whole fibre length L is divided into several parts with the step length as h_s, which is set small enough to get exact results, but not so small to be prohibitively slow to solve. In each step, the corresponding operator is applied and the GNLSE is solved, with the output used as the

input for the next step. For example, at the s-th step, firstly

$$A\left(sh_s, t\right) = \exp\left[\left(\hat{D} + \hat{N}\right) h_s\right] \times A\left(\left(s-1\right) h_s, t\right), \tag{2.65}$$

where $A\left(sh_s, t\right)$ is the solution for Equation 2.62 at the propagation length of $z = sh_s$, as $A = A\left(z, t\right)$ is the complex field envelope at the propagation distance z and time t. Because the $\hat{D}$ denotes the dispersion term and is expressed in terms of time derivatives, by applying a Fourier-transform to Equation 2.63, the term $\frac{\partial}{\partial t}$ can be replaced by $-i\omega$. Thus, solving this term in the frequency domain speeds up the simulations. Equation 2.65 is then split into the first step

$$A\left(\left(s-1\right) h_s, \omega\right) = \mathscr{F}\left\{\hat{N} h_s \times A\left(\left(s-1\right) h_s, t\right)\right\}, \tag{2.66}$$

and the second as

$$A\left(sh_s, t\right) = \mathscr{F}^{-1}\left\{\exp\left(\hat{D}\left(i\omega\right) h_s\right) A\left(\left(s-1\right) h_s, \omega\right)\right\}. \tag{2.67}$$

The split-step Fourier method will be used to solve the GNLSE in the following chapters to investigate nonlinear pulse propagation in the silicon core fibres.

Chapter 3

Fabrication and characterization of silicon core fibres

In this chapter, I will describe the fabrication method, primary characterization tools for the tapered polysilicon (poly-Si) core fibres and the optimization of the tapering process. Firstly, the fibre drawing method for producing the silicon core fibres used in this thesis is discussed. Secondly, post-processing used to taper the fibre core sizes down to dimensions suitable for nonlinear propagation is described. Then, the transmission loss measurements are used to determine the optical quality of the tapered silicon fibres. Next, the two-step tapering is explained with the comparison of different recipes. Finally, the double-clad method for tapering is introduced for increasing the cladding/core ratio.

3.1 Molten core drawing method

There are three main steps in the MCD fabrication process as depicted in Figure 3.1. At first, a silicon rod is sleeved into a silica tube, of which one end is sealed to form a preform. Then, the whole preform is loaded into a furnace and the temperature increased. The temperature of the preform must be sufficiently high that the silicon rod is molten while the whole cladding is viscous, so that the cylindrical geometry is retained [44]. Finally, the preform is drawn down and the SCFs are fabricated. By choosing the appropriate drawing conditions, the fibre core can be produced with crystal grains with lengths of about a few millimetres to several centimetres [81, 82]. Thus, a key advantage of the MCD method is that long fibres can be fabricated using this technique at high speeds.

However, the high temperatures required to draw the SCFs introduce several problems [83]. One of them is that it will result in diffusion of oxygen from the silica cladding to the silicon core [44], which will limit the core size of as-drawn silicon fibres to several tens to hundreds of microns. To solve this problem, a new solution was demonstrated by

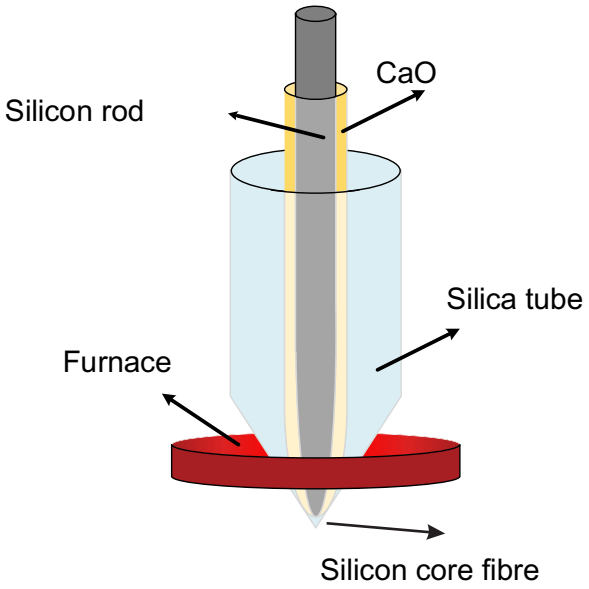

FIGURE 3.1: Schematic of the MCD method.

introducing another layer into the fabrication between the core and cladding that acts as an oxygen getter or diffusion barrier. These barriers can not only isolate the silicon core from oxygen diffusion, but also minimize the cracking and separation between the core and the cladding due to the thermal expansion mismatch of the materials [50]. Using this solution, silicon fibres were reported to be drawn with a core size down to less than 10 μm. The polycrystalline core fibres used in this thesis were fabricated through the MCD method with a thin layer of calcium oxide as the diffusion barrier, as shown in Figure 3.1.

A consequence of the large cores of the MCD fibres is that it limits their use for nonlinear processes. For higher nonlinear effects, small effective mode areas and larger nonlinear refractive indices are preferable. Hence, to enhance the nonlinearity, one way is that we could fabricate fibres using different core materials to obtain larger nonlinearities. An alternative material could be silicon alloy materials, such as SiGe [84]. The other option is to reduce the core size of fibres using post-processing procedures. Tapering via filament heating, as one of the post-processing methods, is discussed below.

3.2 Tapering via filament heating

The large refractive index difference between the silicon core and silica cladding provides good confinement for light propagating within the silicon fibres. However, as previously mentioned, the fibres typically fabricated via the MCD method have core diameters of around 10 μm to 20 μm. Several post-processing techniques exist for conventional silica fibres that can be applied to our SCFs in order to optimise both the quality of the silicon material and the fibre geometry. The two main post-processing techniques involve either

heating the fibres using laser radiation or heating via a filament. Scanning laser radiation along the fibre has been demonstrated to produce low loss fibres with core dimensions as large as 20 μm [85]. But laser radiation can only fulfil one of our two main targets. In contrast, the combination of heating via a filament and stretching the heated fibre, known as fibre tapering, has been investigated lot extensively using conventional silica fibres.

This method can also reach the temperatures required for melting and re-growing the crystal structure of the silicon core to help improve the material properties. Meanwhile, simultaneous tapering of the core is used to tailor the SCFs to the desired dimensions [86]. Tapering via filament heating, therefore, is chosen as the post-processing method to further optimize the as-drawn fibres [87]. Using this approach, the crystallinity of the fibre core has been reported to be improved to levels comparable to what has been obtained with laser heating [52–54]. The process of tapering via filament heating is described in more detail below.

3.2.1 Tapered fibre profile

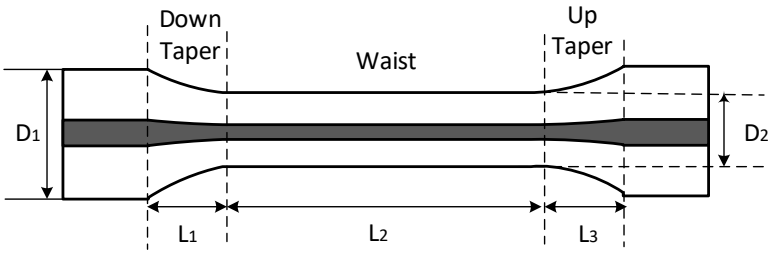

FIGURE 3.2: General design profile of a tapered fibre.

Here, the general profile of our tapered silicon fibres is introduced. The silicon core area is marked dark grey in order to be distinguished from the silica cladding. As seen in Figure 3.2, the fibre section with the narrowest constant core diameter in the middle is the waist region. Between the waist region and the untapered regions, the fibre diameters change along with the axial direction, z axis, which are known as the transition regions. Within them, the region where the fibre diameter decreases from the untapered region to the waist region is called the down taper region and correspondingly, the region where the fibre diameter increases from the waist region to the untapered region is called the up taper region. The fibre lengths of the down taper region, the waist region and the up taper region, are labelled as L_1, L_2 and L_3, respectively. The taper ratio is defined as the ratio of the cladding diameters of the original fibre D_1 and that of the waist region D_2. In practice, even though the lengths of the down taper L_1 and the up taper L_3 are designed to be the same, the profile of the fabricated fiber is asymmetric, with the slightly longer L_1 but shorter L_3.

3.2.2 Taper technique

An automated glass processor (Vytran GPX-3400-V5) was used to conduct the tapering processes. The work station of the processor is seen in Figure 3.3. It consists of a filament-based heater, which provides a stable high temperature for processing, two precision stages, which are also called fiber holders that hold and control the fibres precisely, and a high resolution CCD camera, which monitors the top down view of the sample above. The main tapering schematic via filament heating using the Vytran is depicted in Figure 3.4. The filament used in the processing is the standard graphite filament V4F, which covers a range of cladding diameters from 125-600 μm. This is suitable for tapering most fibres with diameters below 600 μm. The fibre is heated in the filament and when the temperature goes up, resulting in the silicon core melting and the silica cladding softening. By pulling the left part of the fibre and feeding the right part towards the left, the fibre can be stretched down to the desired core/cladding dimensions and the silicon core crystallizes as it cools.

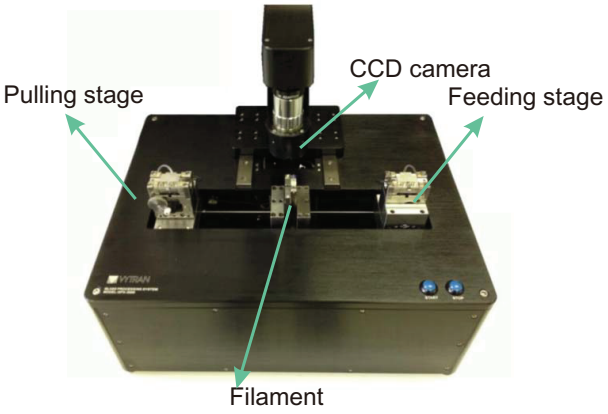

FIGURE 3.3: The workstation of the Vytran processor.

The work station is connected to a personal computer, where software is installed for monitoring and controlling the tapering processes. The in-built software is used to adjust the whole process according to our needs. The window for **Tapering Properties** is seen in Figure 3.5. Based on the designed tapered fibre profiles, the parameters on the first two tabs of the tapering properties, **Taper Dimensions** and **Taper Parameters** are mostly revised. Here, explanations for main parameters will be provided and some important notes will be given, based on personal experimental experiences. Information on the last two pages can be found in the user manual and their settings have been kept as default within the use.

The page for **tapering dimensions** is seen in Figure 3.5. After inputting the fibre properties, L_1, L_2, L_3, D_1 and D_2, as in Figure 3.2, together with the other parameters, such as the tapering speed, the software will automatically calculate and design the taper process based on the input information. The minimum number input for lengths (L_1, L_2 and L_3) is 1 mm and the minimum input for D_1 and D_2 are 80 μm and 10 μm,

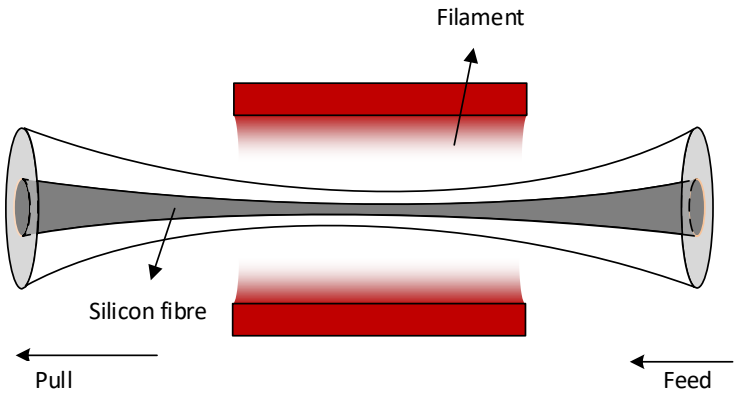

FIGURE 3.4: The tapering scheme using the Vytran processor, in which the filament heats the middle area and the fibre gets tapered.

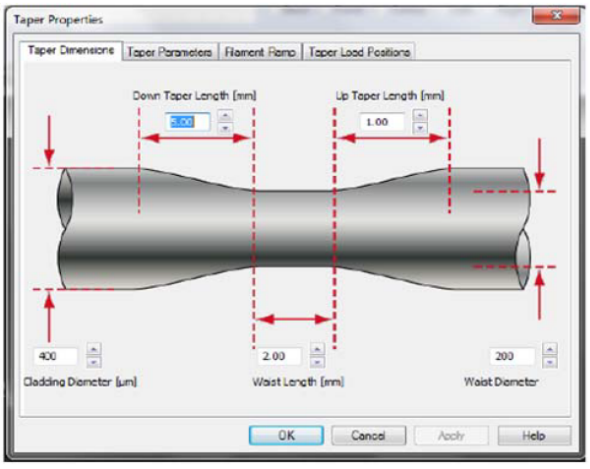

FIGURE 3.5: The GUI window of tapering properties for Vytran GPX 3400

respectively. Therefore, this requires a conversion between the real diameter and the input one if we would like to taper the fibre from 50 μm to 10 μm with the taper ratio of 5.0. In this case, only input D_1 and D_2 as 80 μm to 16 μm, which will ensure the fibre gets tapered under the same taper ratio (5.0=80/16). The adiabatically tapers are guaranteed by limiting the minimum transition length of 1 mm.

The page for **tapering parameters** is seen in Figure 3.6. When the tapering process starts, the software will initiate the filament to move to a certain height so that the fibre is loaded in the middle of the filament. The filament then start to heat up and the tapering can begin. **Furnace Offset** is used to shift the filament along the fibre axial direction to a desired location before tapering is started. Because the reflection mirror for imaging the fibres on the Vytran is at the right side of the filament by around 7 mm, the actual imaged point of the fibre obtained from the mirror is 7 mm away from the

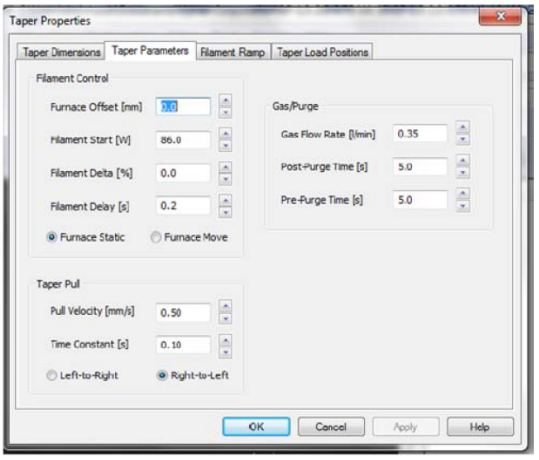

FIGURE 3.6: The editable tapering GUI for Vytran GPX 3400

filament. Hence, in order to taper the fibre starting from the exact point of the image obtained from the reflection mirror, the filament offset must be set accurately every time when it starts to taper. Alternatively, it can be set manually by moving the filament location in the Motor Control window. Here, 7 mm is just an approximate number. Each time after the filament gets replaced, the calibration process will be conducted and the calibrated number for the filament offset shall be updated. Until the next time of filament replacement, this number normally remains the same.

Filament Start P_s will give the filament an initial power to start the tapering process. The initial filament power indicates a certain temperature to which the fibre will get heated. However, the heating temperature does not increase linearly with the power of the filament and its precise value is not obtainable because measurements of the temperature within the filament cannot be conducted accurately. Besides, the filament itself will degrade with multiple uses. Therefore, P_s given in this thesis is presented as a guide value and will need to be revised after a period time of use and for different filaments. Generally, for single mode fibres, the filament start power for a tapering process can be set as 80% of its splice power. In regards to tapering fibres with various cladding and core materials, the filament start power P_s shall always change according to designed fibre profiles and materials.

Filament Delta δ will change the filament power from P_s to $P_s(1+\delta)$ at the start of the waist tapering. Hence, if δ is below zero, the filament power will decrease when the down taper region finished and increase after tapering the waist area. For a fibre designed with a length of $\sim$1 cm, the tapering process can be completed within $\sim$1 min at a tapering speed of 1.0 mm/s. Thus, it is recommended to keep δ at 0 for tapering a SCF with a short waist length, as any drastic temperature change will cause instability during the waist tapering. Most of the tapered fibres fabricated in the thesis had δ set to 0.

Filament Delay τ is the period of time when the filament is kept on before the filament moves up to begin the tapering process. The default is 0.5 s for fibres with cladding diameters of 125 μm. However, for fibres with a cladding diameter of 400 μm, as many of the SCFs have, τ should be changed to 1.2 s.

Gas Flow Rate and **Post-purge Time**, **Pre-purge Time** are used to control the argon gas flow during the tapering process. The default values are 0.2 l/min, 5.0 s and 5.0 s. This means the argon will flow for 5.0 seconds at the rate of 0.2 l/min before and after the fibre is pulled, respectively. These values will normally remain as default, except for some special circumstances.

Pull Velocity represents the constant speed at which the fibres get pulled during the whole tapering process. The value can be changed from 0.2 mm/s to 2.0 mm/s. In this thesis, all fibres are tapered under the speed of 1.0 mm/s.

Time Constant has a default value of 0.1 s, and represents the time for the software to calculate the velocities for the whole system in order to finish the taper process.

3.2.2.1 Tension monitoring

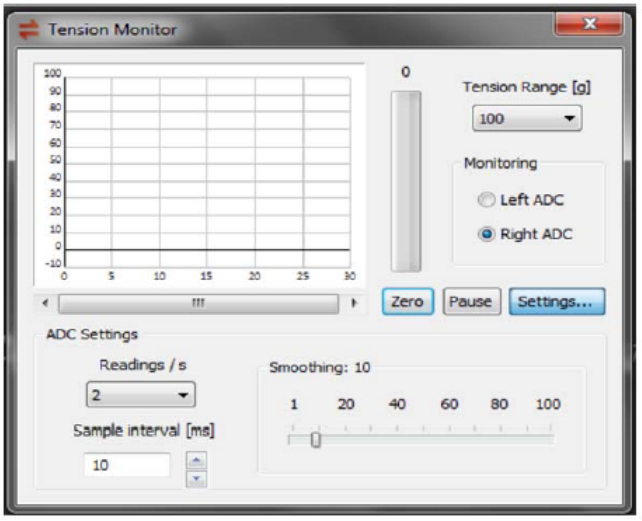

FIGURE 3.7: The window of the tension monitor

The only tool utilized to track the tapering process is a tension monitor on the Vytran, as it can provide feedback of the fibre tension with time during the whole process. The window for the tension monitor is displayed in Figure 3.7. Considering that the temperature can't be measured during the tapering process, we can observe the fibre tension instead because the tension is largely dependent on the temperature during the process. The sensor for measuring the tension is built in the right fibre holder. Even though the displayed tension is measured to be the tension of the fibre held within the right holder, it should be the same across the waist region as the assumption is that the

tension remains the same along the whole fibre in the axial direction. It is worth noting that the tensions must be zeroed in Figure 3.7 before loading the fibre onto the holders to ensure the tension readings are accurate. As an example, a typical relation of the measured tension as a function time during the tapering is shown in Figure 3.8, which was obtained by tapering a fibre with 15 mm waist length.

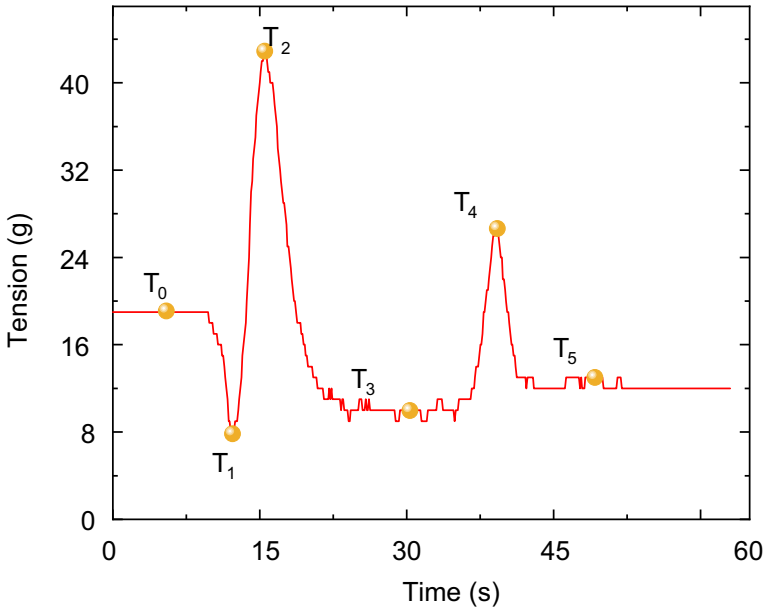

FIGURE 3.8: The typical tension monitor as a function of time, T_0 to T_5 represents six different positions while tapering.

T_0 is the initial tension before the tapering process starts. The value indicates how the fibre gets loaded and initially stretched. A suitable start tension T_0 for a silica-clad fibre with a diameter of 400 μm is typically around 20 g by adjusting the positions of the left and right fibre holders in fine steps. In comparison, for a SCF with the diameter as 125 μm, T_0 is generally set around 10 g.

When tapering starts, the filament will heat up and soften the fibre. T_1 represents the tension when the fibre is fully softened. Its values depends on the given power of the filament P_s and the time of the filament heating delay τ.

During the tapering process, the left fibre holder will pull the fibre to the left and the right one will feed the fibre at a slower speed than the pulling speed. The maximum tension in the whole process will appear as T_2, when the fibre is just about to get pulled by the left fibre holder but the feeding hasn't yet started. T_2 provides an indication of what the temperature in the waist region is. This in return, gives instruction on how the filament power shall get revised. If T_2 is too high, for example larger than 100 g, the power of the filament P_s should be increased because the fibre hasn't softened enough and there is a risk of breaking the small core silicon fibres. Especially for tapering fibres with cladding diameters less 30 μm, 100 g is the maximum tension before it breaks. Negative T_2 indicates that the fibre has been overheated, therefore, it is recommended

to decrease the power P_s. For SCFs, overheating during tapering will mainly cause breakup in the silicon core, making it discontinuous, resulting in poor crystallization of the silicon. However, it is not always harmful. For specific structures, such as SCF with nano-spikes, slight overheating will help to form the nano-spike tip. If the temperature is well controlled, good crystallinity of the silicon could still be realized.

T_3 displays the tension when the waist region is being formed, after the feeding starts. T_4 may appear sometimes when it forms the up taper region. To note, when tapering fibres with the cladding diameter below 30 μm, T_4 needs to be controlled under the maximum breakable tension of the fibre waist region. Otherwise the fibre will easily break at the last step during the formation of the up taper region. T_5 is the measured tension after the whole process is finished.

3.3 Fibre end facet preparation

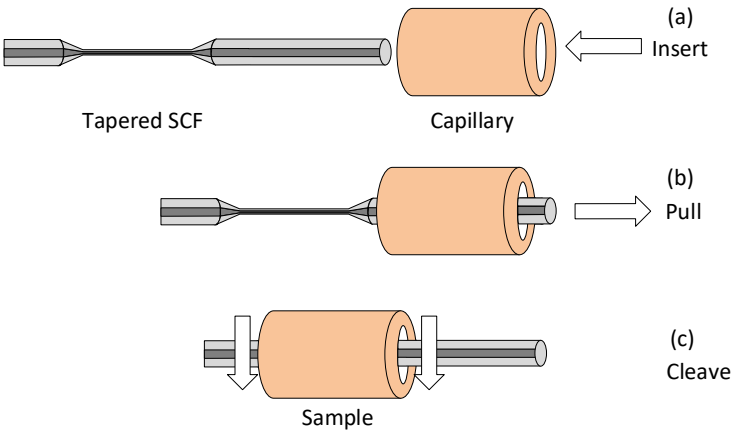

FIGURE 3.9: Diagram of preparing small tapered SCF into a capillary for polishing. (a) Insert the tapered SCF. (b) Pull the tapered SCF to protect the waist region. (c) Cleave off the straight sections of the SCF.

To prepare the end facets for subsequent characterization and nonlinear investigation, the tapered SCF is firstly mounted inside a large silica capillary, whose inner diameter is 250 μm, and outer diameter is 665 μm. As seen from Figure 3.9, a tapered fibre was inserted to a thick silica capillary, which acts as a buffer to secure and strengthen the bare fibres. In order to mount the tapered silicon fibre successfully, especially for small core fibres that have a cladding diameter less than 30 μm in the waist region, some untapered regions, whose length is the same as the total taper length, were kept after tapering at each end. Slowly insert the untapered region in to capillary by moving the capillary towards the SCF, as shown in Figure 3.9(a). After some of the untapered region can be seen outside of the capillary, slowly pull the whole tapered fibre into the capillary until the tapered region including the up- and down- tapers are all in the capillary.

Then carefully cleave off the unwanted SCF sections that are outside the capillary, as in Figure 3.9(c).

Next, to fix the SCF inside the capillary, beeswax with a melting point temperature of 63°C was used. By heating the wax on a hot ceramic plate, the melted wax forms a fluid to fill the gaps between the capillary and the fibre. After the wax fills the entire fibre length, leave the whole sample to cool down to the room temperature, at which point the wax solidifies and the fibre gets fixed robustly in the silica capillary. Figure 3.10(a) shows the longitudinal cross-section of a fibre that has been successfully inserted in to the capillary, with the gap between the fibre and the capillary filled with wax.

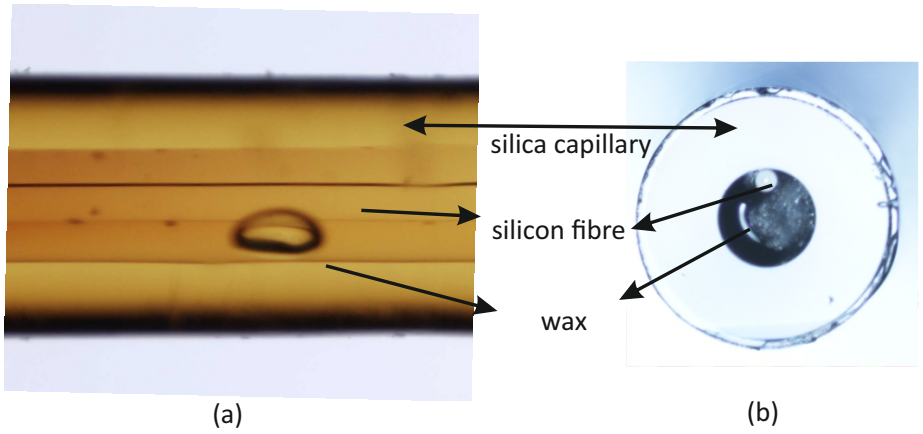

FIGURE 3.10: (a) Longitudinal cross-section plane of the fibre in a capillary. (b) Transverse plane of a polished fibre.

The third step is to prepare two flat, damage- and crack-free facets to couple light into the fibres. A conventional polishing method was used, which employs an Ultrapol polishing machine manufactured by Ultratec. A precision jig was used to maintain the flatness of the fibre facing on the polishing plate. Polishing films were put on the polishing plate and, by using different grades of polishing films in sequences, the end facets of the fibre can be polished by circulating the fibre over those polishing films. The three grades of polishing films used had particle sizes from coarser to finer diameters, 9 μm, 3 μm and 0.3 μm, respectively. Distilled water was added on the 0.3 μm polishing film for obtaining smooth end facets. A successfully polished end facet of a fibre is shown in Figure 3.10(d), where the silicon fibre is surrounded with wax.

3.4 Characterization of tapered silicon core fibres

With the goal of making a small core SCF with low losses, different types of as-drawn fibres have been used for tapering. These fibres were all pre-drawn by our collaborators in Prof. John Ballato's group from Clemson University, with the preforms provided

by Prof. Ursula Gibson's group from Norwegian University of Science and Technology. These specific as-drawn fibres have been successfully tapered to low-loss SCFs. The two fibres are labelled as D429 and O212. The silicon core rod used for the D429 was heavily doped n-type silicon, whereas the silicon material used for O212 has higher purity silicon and higher resistance of 15∼22 Ω·cm [88].These original values were provided by our collaborators. The dimensions of cladding and core, and their cladding core ratio of two fibres are also different, as all listed in Table 3.1.

Label	**Clad diameter**(μm)	**Core diameter**(μm)	**Clad/Core ratio**
D429	144.0	5.5	26.2
O212	376.2	28.5	13.2

TABLE 3.1: Dimensions of as-drawn fibres of two samples.

The as-drawn fibres labelled as D429 and O212 were used for demonstrating the transmission characterization methods in this section. Table 3.2 shows the recipes and structures for fibre 1, 2, 3 and 4, where P_s is the filament start power. D429 was tapered firstly from 144.0 μm to 52.0 μm to obtain fibre 1 with a core diameter of 2.0 μm, and from 144.0 μm to 40.0 μm to obtain fibre 2 with a core diameter of 1.5 μm. Fibre 1 and fibre 2 have the same design for the transition and waist lengths, where L_1, L_2 and L_3, were respectively 7 mm, 15 mm and 7 mm.

Label	**Material**	D_{core} (μm)	D_1 - D_2 (μm)	L_1-L_2-L_3 (mm)	P_s
fibre 1	D429	2.0	144-52	7-15-7	79 W
fibre 2	D429	1.5	144-40	7-15-7	74 W
fibre 3	O212	0.9	376-70	5-13-5	85 W
			70-11	3-5-3	68 W
fibre 4	O212	0.9	376-70	5-13-5	85 W
			70-11	3-5-3	63 W

TABLE 3.2: Recipes for four tapered fibre samples.

As O212 has a smaller cladding/core ratio of 13.2, in order to taper the core size from 28.5 μm down to less than 1 μm, the outer cladding diameter needs to be tailored from 376.2 μm to around 10 μm. Thus, to avoid breaking the fibres due to drastic changes in tension needed during tapering to achieve such a smaller cladding diameter, a two-step tapering process is applied to maintain a continuous and high quality crystalline core. The detailed consideration for the two-step tapering is presented in the following

Section 3.5. But briefly, the first step tapers the fibre down to 70 μm and the second step tapers it down further to a fibre with a diameter of 11 μm. Fibre 3 and fibre 4 have an identical taper design. The transition and waist lengths L_1, L_2 and L_3, were 5 mm, 13 mm and 5 mm, for the first step, and 3 mm, 5 mm and 3 mm for the second step. The core diameter of fibre 3 and fibre 4 were both designed to be 0.9 μm.

3.4.1 Linear loss measurements

To estimate the linear losses of these SCFs, cutback measurements were undertaken using the experimental setup, as shown in Figure 3.11. A mode-locked fibre laser with a central wavelength at 1541 nm (Onefive ORIGAMI) was used as the pump source, with the calibrated pulse width at 650 fs and the repetition rate at 40 MHz. The input average power was kept at a rather low value (around 30 μW), so that only linear process happened in the SCFs. Two beam-splitters (T=92% @ 1 - 2 μm) were mounted in the setup. One in the input arm was used for capturing the reflected light from the input facet of the fibre and the second at the output was used to collect the light propagating through the sample. For the purpose of getting brighter and clear images, these beam-splitters can be exchanged to ones with transmission rates of 55% , which is suitable for small input core fibres. Objectives were used to couple the light from free space into the sample and then out of the sample onto the power meter. A 40× silica objective lens OBL1 with a NA of 0.65 and a 60× lens OBL2 with a NA of 0.80 were used at the input and output, respectively, to couple the light efficiently. These two objective lenses and the sample were all mounted on piezoelectric-controller stages. CCD cameras were used to monitor the input and output beam profiles. By monitoring the beam profile in the camera of the output arm, the single mode can be selected by carefully adjusting the input objective lens OBL1. The optical power meter used was a Thorlab S140c detector.

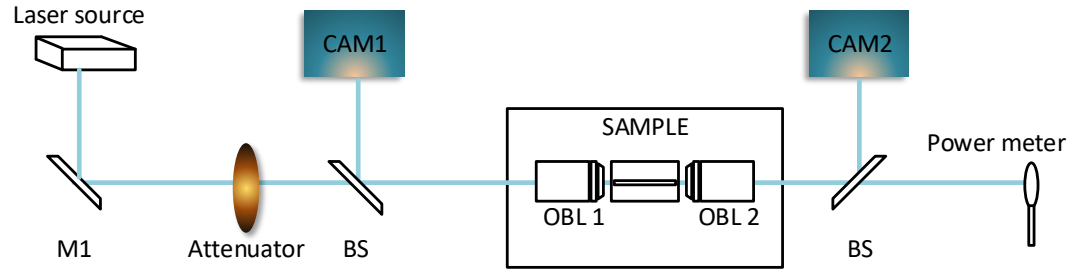

FIGURE 3.11: Experimental set-up for loss measurements.

The total losses of each sample were measured several times and, for each data point, the output power recorded was averaged over a minute time period. The uncertainty in the measured coupling losses was as ±0.2 dB and the uncertainty of the fibre length was as ±0.1 mm. For each data point, the variation in the output measured powers was

very small because the average output power from the pulsed laser source was stable and the main variation is due to the different coupling losses each time. Eventually, the uncertainties of linear losses from the cutback method are calculated from the linear fit with several loss measurements at different lengths via the linear fit function in OriginLab. These error estimations are shown in each figure presented below, where the y error bars include the contributions from the uncertainties in the coupling losses and output powers, and the x errors are due to the uncertainties in the length measurements.

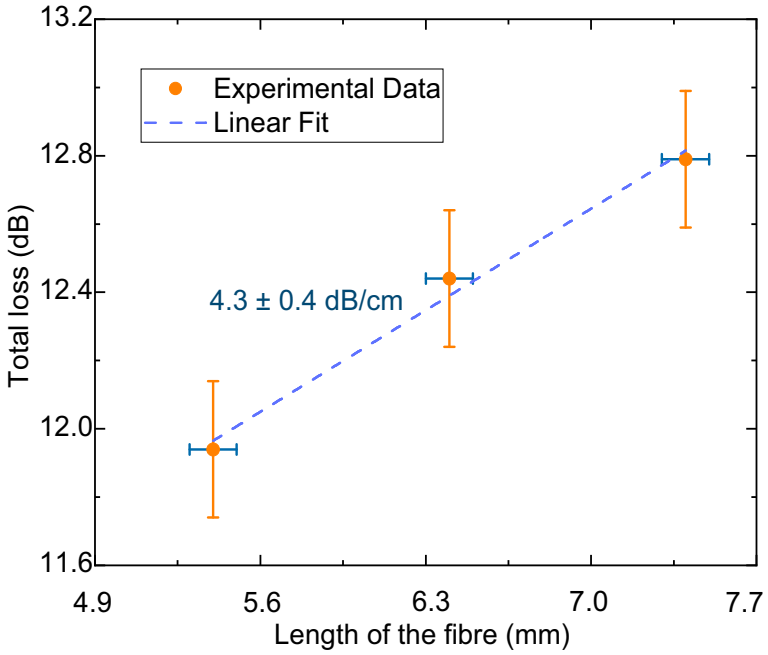

FIGURE 3.12: Transmitted power as a function of fibre length at 1.54 μm for fibre 1, of a core diameter at 2.0 μm

The waist regions of fibre 1 and fibre 2 were kept by removing both transition regions, leaving a straight fibre with constant core diameter. The core diameters of the input and output end facet for fibre 1 and fibre 2 were 2 μm and 1.5 μm, respectively. For fibre 3, the down-taper region was kept. Its input end facet was polished to a core diameter of 4.0 μm and the core diameter of the output end facet was 0.9 μm.

The results for fibre 1 are shown in Figure 3.12. It was polished from 7.4 mm to 6.4 mm and then 5.4 mm and the losses at each length were measured. It can be seen from Figure 3.12 that the linear losses of fibre 1 was 4.3 dB/cm, and at 5.4 mm, the total transmission was about 11.4 dB. The total coupling losses can be calculated as 9.6 dB, by subtracting the linear loss from the total transmission.

Fibre 2 was polished from 9 mm to 7.5 mm, 6.5 mm and 5.5 mm and the measured linear losses are shown in Figure 3.13. The linear loss of fibre 2 was 7.3 dB/cm, and at 9.0 mm, the total loss was about 15.5 dB. The coupling losses can be estimated as 8.9 dB.

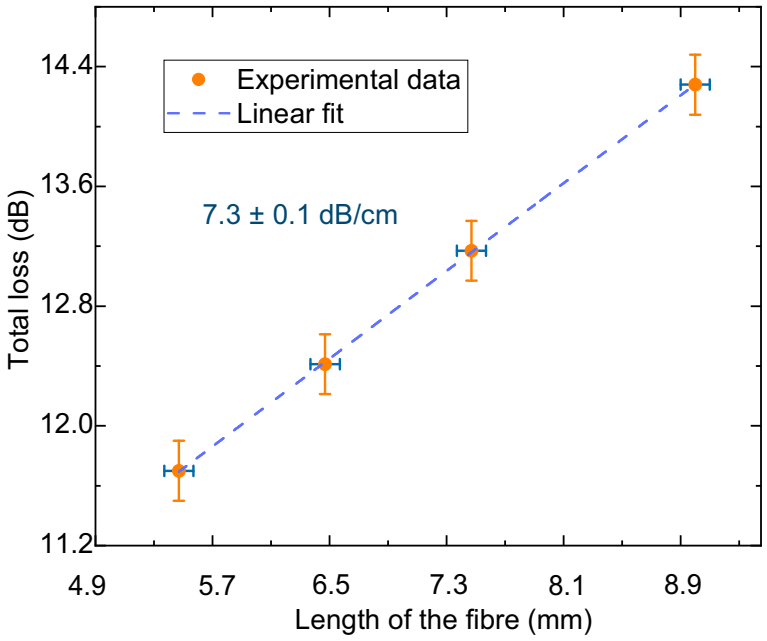

FIGURE 3.13: Transmitted power as a function of fibre length at 1.54 μm for fibre 2, of a core diameter at 1.5 μm.

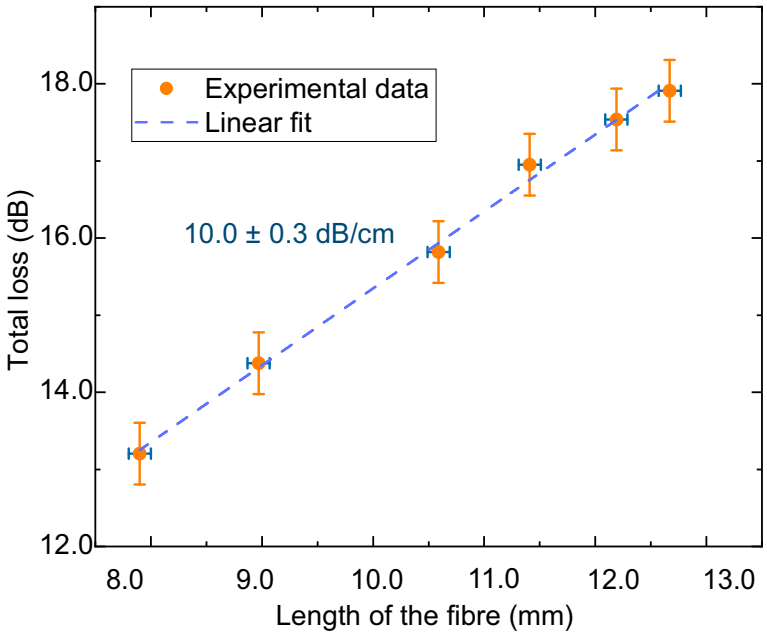

FIGURE 3.14: Transmitted power as a function of fibre length at 1.54 μm for fibre 3, of a core diameter at 0.9 μm.

Linear losses of fibre 3 were measured at 5 different lengths, from 9.2 mm, 8.4 mm, 7.6 mm, 6.0 mm and 4.9 mm. The results for fibre 3 are displayed in Figure 3.14. The linear loss for this taper was about 10.0 dB/cm. The total loss was about 13.1 dB at 4.9 mm. The coupling losses can be calculated as 8.0 dB, lower than that of fibre 1 and fibre 2.

As explained in Section 2.1.4, the total loss is comprised of linear loss, nonlinear losses

and the coupling losses, which mainly result from the Fresnel reflection of the input and output facet($\sim$ 3 dB), the absorption of the lens to the laser source ($\sim$2 dB) and the mode mismatching due to the free space coupling. By injecting light into the fibre 3 whose input core diameter (4.0 μm) is larger than its waist region (0.9 μm), the mode mismatch losses decreased, therefore, its coupling efficiency is better than fibre 1 without the input taper kept. To obtain lower coupling losses for further nonlinear experiments for small SCFs, both transition regions shall be kept to decrease the mode mismatch losses. By using this data, and other measurements for different input/output diameters, we estimated the coupling efficiencies for SCFs with known facet dimensions. Therefore, the linear losses can be estimated by subtracting the fixed coupling losses from the total losses. Under such schemes, the linear losses of the waist region for tapered SCFs can be evaluated and its values should be reasonably accurate without the need for conducting cutback measurements, which are destructive. This provides a fast characterization of the fibre linear losses of the waist instead of damaging the fibres at the first hand.

For example, an estimation of linear losses for fibre 4 is given. By adjust the tapering powers carefully, Fibre 4 was fabricated with the initial filament power P_s of 63 W, which is 5 W lower than that of fibre 3, as seen in Table 3.2. The total length of fibre 4 is 8.0 mm, which includes a 5-mm-length waist region and both the down and up tapers. The input and output facets were both polished down to 4 μm as the core diameter to improve the coupling efficiency. The total loss of 9.0 dB was measured, using the setup in Figure 3.11 with the pump wavelength of 1.54 μm at a low average input power around 30 μW. The propagation loss of fibre 4 was estimated to be 2.5 dB/cm at 1.54 μm, by subtracting the coupling loss of 7.0 dB in total from the total loss, where 2 dB is estimated to be as the mode mismatching losses. This propagation loss represents one of the lowest value reported for a poly-Si sub-micron waveguides [53], which will be confirmed in Section 3.4.2 using the nonlinear measurements.

Label	**Waist diameter**	**Linear losses**	**Total coupling losses**
fibre 1	2.0 μm	4.3 dB/cm	9.6 dB
fibre 2	1.5 μm	7.3 dB/cm	8.9 dB
fibre 3	0.9 μm	10.0 dB/cm	8.0 dB
fibre 4	0.9 μm	2.5 dB/cm*	7.0 dB

TABLE 3.3: Linear losses of four samples tested

In the end, Table 3.3 shows a summary of the results of the loss measurements for these four SCFs. The linear losses of fibre 1, fibre 2, fibre 3 and fibre 4 are respectively 4.3 dB/cm, 7.3 dB/cm, 10.0 dB/cm and $\sim$2.5 dB/cm. The reasons that fibre 4 has shown the lowest linear losses can be attributed to the tapering temperature. As silicon fibres with smaller cores are quite sensitive to the heating and cooling rate, the tapering temperature is one of the key factors of the improving the crystallinity of the poly-Si

core. With the reduction of the tapering power at the second-tapering for fibre 4, the linear losses has been decreased largely.

3.4.2 Two-photon absorption coefficient estimation

In SCFs, nonlinear absorption due to two-photon absorption (TPA) can be observed at high pump powers. When increasing the input peak power, the output peak power starts to saturate due to the increased absorption induced by β_{TPA}. The transmission curve can be obtained by measuring the output power vs increasing input power in gradual steps. β_{TPA} and α_{f} can be estimated reasonably by fitting that curve via solving the GNLSE that describes the pulse propagation in silicon fibres, as discussed previously in 2.4.1. However, as the length of the silicon fibres is shorter than the dispersion length, the effects of dispersion can be neglected during the initial simulations. By substituting Equation 2.40 and the pulse intensity $I = |A|^2/A_{\mathrm{eff}}$ into Equation 2.59 and Equation 2.61, the temporal pulse propagation in the fibre pumped at high intensity can be expressed by the simplified NLSE as

$$\frac{\partial I}{\partial z} = -\alpha_{\mathrm{l}} I - \beta_{\mathrm{TPA}} I^2 - \alpha_{\mathrm{f}} N_{\mathrm{c}} I, \tag{3.1}$$

$$\frac{\partial N_{\mathrm{c}}}{\partial t} = \frac{\beta_{\mathrm{TPA}}}{2h\nu_0} I^2 - \frac{N_{\mathrm{c}}}{\tau_{\mathrm{c}}}, \tag{3.2}$$

where α_{l} in dB/cm is the linear propagation loss.

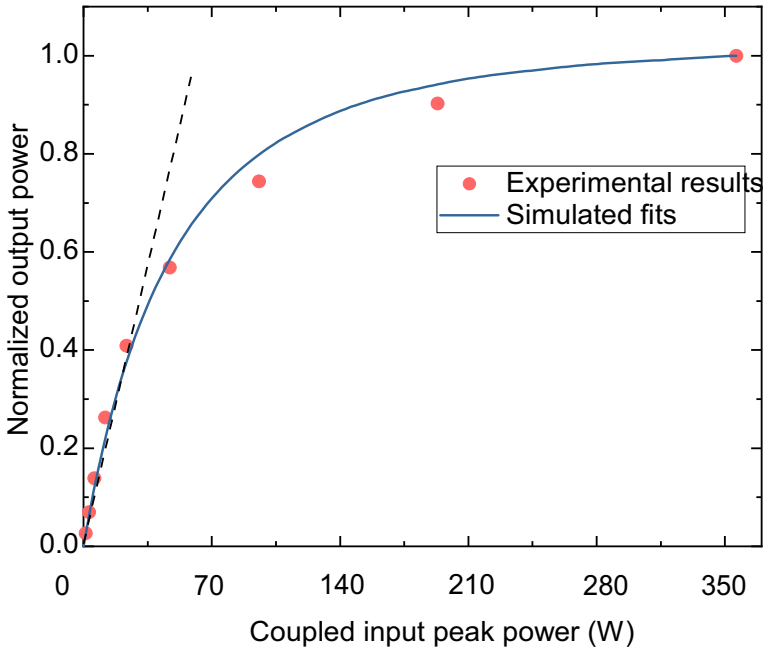

FIGURE 3.15: Output power increasing with input peak power in fibre 2.

Using fibre 2, for example, as this fibre has a consistent core diameter, experimental results of TPA were obtained by using the same setup in Figure 3.11 but using higher input pump powers. The normalized output peak power as a function of input peak power at 1.54 μm is plotted in Figure 3.15, where the orange dots are the experimental results and the continuous blue curve is the simulated results. For fibre 2, α_l = 7.3 dB/cm and the length of 9 mm were used for the simulations. β_{TPA} is estimated as 0.70 cm/GW for the best fitting, with $\alpha_{\text{f}} = 1.0 \times 10^{-16}\text{cm}^2$, τ_{c} = 86 ns, from Ref [64], and $A_{\text{eff}} = 0.97\ \mu\text{m}^2$.

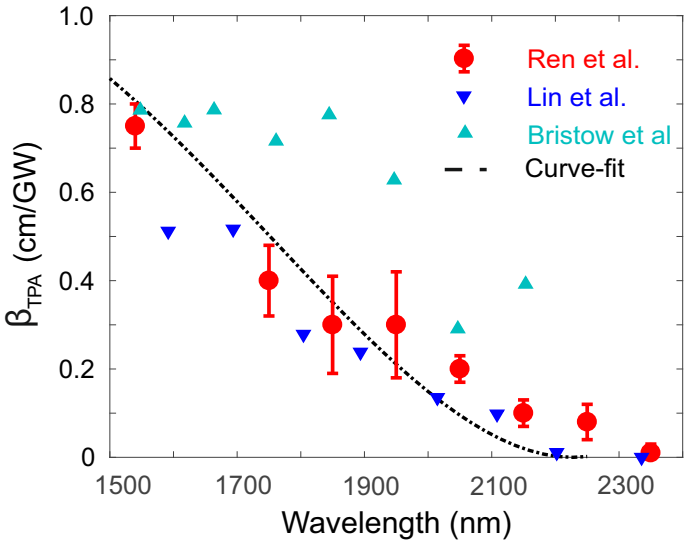

FIGURE 3.16: Measured TPA parameters as a function of wavelength [55, 89, 90].

Wavelength dependent β_{TPA} has been measured for bulk silicon materials and polysilicon fibres in Ref [55, 89, 90] and the results are replotted in Figure 3.16. As seen from Figure 3.16, β_{TPA} decreases the increasing wavelength and tends to zero if the wavelength is over 2.25 μm. It should be noted that the measured β_{TPA} in this section is consistent with the values reported Figure 3.16. The same TPA coefficient was expected for tapered fibre 1 and fibre 2, as they are from the same as-drawn fibre. Fibre 3 and fibre 4 are from the same as-drawn fibres O212, and these were estimated to be approximately 0.75 cm/GW at 1.54 μm.

3.4.3 Nonlinear refractive index estimation

The role played by the nonlinear refractive index is to induce spectral broadening of the pulses, due to SPM, as they propagate with with high peak powers. The experimental setup to observe SPM is similar to that in Figure 3.11, where a 10× silica objective lens with $NA = 0.26$ and a single mode fibre (SMF-28) were now used for capturing the output spectra into an optical spectra analyser. Using the modified setup, the spectral

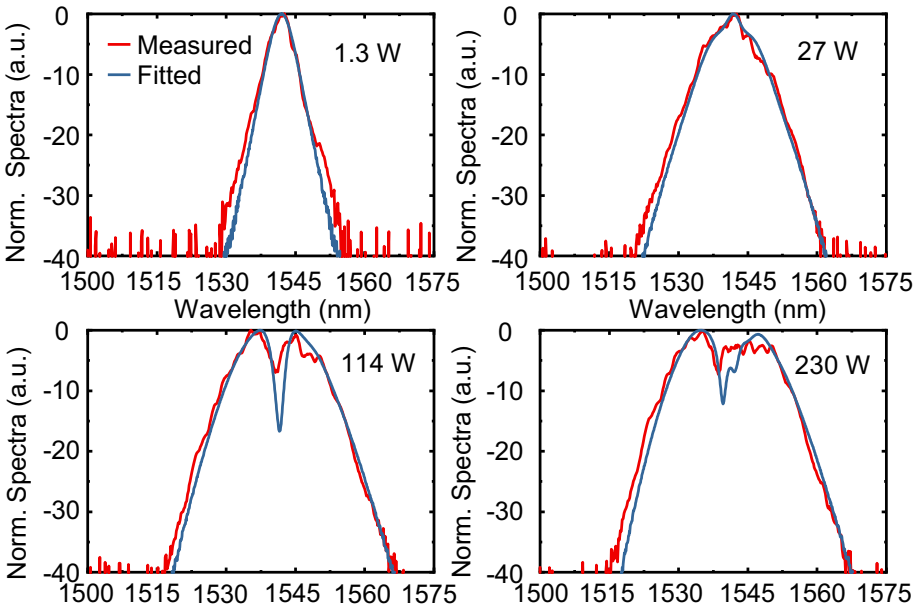

FIGURE 3.17: Experimental spectral evolution dependent on the input peak power for fibre 2.

broadening can be mapped as a function of the coupled input power. Then, n_2 can be estimated via simulations using the full GNLSE and the predetermined loss values by finding the best fitting for spectral broadening dependent on the increasing input peak power. Because the n_2 values are obtained by comparing the experimental data to the calculated results, the fitted values are affected greatly by the estimated input coupling losses. By considering the minimum and the maximum of the input coupling losses, the errors of estimated n_2 can be given.

Figure 3.17 shows the experimental spectral evolution when pumping fibre 2 with different input peak powers (from 1 W to 230 W) as orange curves. When pumping with a peak power of 1 W, the output spectrum was smooth, symmetric with a near hyperbolic secant profile indicating linear propagation. After the input peak power increased to 10 W, the spectrum becomes broadened and a shallow dip appears in the centre, which is mainly due to SPM. The spectra also start to become asymmetric due to the free carrier absorption [80]. Then, with greatly increased input peak power, the spectrum continues to get wider. However, after 190 W of input peak power, the spectral broadening only increases slightly with further increases in the input peak power, which was due to saturation of nonlinear absorption. When the peak power reaches to 190 W, the spectral width could expand around 45 nm, from 1515 nm to 1560 nm. As the input coupling losses for fibre 2 shall range from 4.5 dB to 6.9 dB, the estimated n_2 shall be 3.5-4.5$\times$ 10^{-14} cm^2/W. The best fit was found by using the value of n_2 as 4.0$\times$ 10^{-14} cm^2/W, as seen in the blue curves in Figure 3.17.

The SPM was also investigated in fibre 3 in order to draw a picture about the spectral broadening with a smaller core size. In comparison to our previous reported results in Ref [53], fibre 3 has larger linear loss, but it also showed wider spectra broadening, as

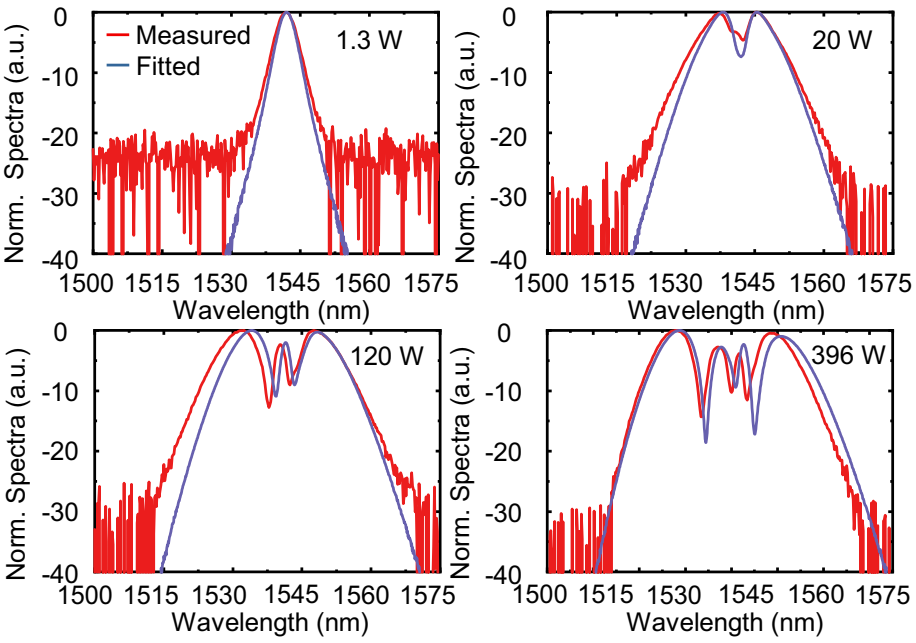

FIGURE 3.18: Experimental spectral evolution dependent on the input peak power for fibre 3.

plotted in Figure 3.18. It is assumed that keeping the down taper region has improved the coupling efficiency and the nonlinearity for the as-drawn fibre is similar to the one in Ref [53], where n_2 was determined to be $5\times\ 10^{-14}$ cm^2/W.

3.5 Two-step tapering of small silicon core fibres

While tapering as-drawn SCFs that have different cladding-to-core ratios, the tapering parameters shall be chosen according to their dimensions and changes in the tapering recipes should be made to reflect these differences. In general, there are two main considerations when setting the tapering parameters. The first one is to obtain the desired dimensions of fibres. To obtain the right geometry, we mainly monitor the cladding diameter as it is assumed that the cladding-to-core ratio is kept constant during the whole tapering process, if no double-clad method is applied. The transition lengths are also kept to long lengths for obtaining slowly varying angles between the taper transitions and the waist, to avoid excessive coupling to cladding modes. The down and up taper regions were set as ∼3 mm.

The second consideration is to realize the optimal crystallization for the silicon core along the whole fibre length. Through precise control of the maximum temperature during the tapering process, the quality of the poly-Si can be improved [91]. The initial power of the filament P_s will determine the maximum temperature during tapering, which needs to reach the melting point of silicon (1440°C) and softening of the silica cladding. Particularly for smaller core fibres, less heating power but more accurate

controll of the temperature is preferred. As the filament temperature will degrade with time of use, an alternative way to monitor the filament temperature is to keep track of the fibre tension during the tapering process, as explained in section Section 3.2.2.1. Among the six tension values, T_2 is the most valuable one. The set values of the used filament power P_s and maximum tension T_2 can be used to repeat the whole tapering process. By mainly comparing these two values, a guidance of the tapering process can be given.

Label	**Clad diameter**(μm)	**Core diameter**(μm)	**Clad/Core ratio**
J895	125	12.5	10

TABLE 3.4: Dimensions of as-drawn fibres of the third sample.

Due to the limited length of as-drawn D429 and O212 fibres, the third as-drawn fibres J895 were used here for the comparison of the recipes, as these are in plentiful supply. The silicon that J895 used has the same nonlinearity to D429 and O212, but the highest resistance, more than 4800 Ω·cm, which will induce less FCA. Therefore, the as-drawn fibres J895 were mostly used for the nonlinear experiments in this thesis. As listed in Table 3.4, J895 has a cladding diameter of 125 μm and a core diameter of 12.5 μm with the cladding core ratio of 10. For small core SCF with core diameter of around 1 μm, the cladding would be around 10 μm. For a fibre with such a small geometry, lower powers will be beneficial for improving the crystallinity for poly-Si cores. By applying the two-step tapering method using J895, the tapering recipes were compared to produce a low-loss tapered small core fibre, via applying different filament powers. All the other settings remained as the default values.

At first, fibres 5-9 were all tapered from 125 μm down to 49 μm with the down-taper and up-taper regions of length 3 mm, and the waist region as 7 mm long. Then, to prepare the end facets for loss measurements, I kept the down and up taper regions and polished the input and output of core diameters to around 6 μm. The total length of these fibres were all the same, about 10.0 mm. The only difference with these fibres were the tapering powers P_s. The maximum tensions T_2 are also given, as seen from Table 3.5. The fibre loss is a convenient parameter to check the crystallinity of these fibres and then decide which recipe is most suitable. For these loss measurements, the total losses α were measured using a CW laser at 1550 nm at low input power. Table 3.5 shows that the total losses for fibres 5-9 were all around 6.0 dB, where the linear losses were estimated to be around 0.5 dB/cm with the coupling losses to be 5.5 dB.

It can be also seen that, when the tapering power P_s decreased, the maximum tension T_2 will go up. The relation of P_s and T_2 is drawn in Figure 3.19, where the red line is the linear fit calculated via OriginLab. It confirms the approximately linear relation between T_2 and P_s. with the linear slope of about -9.1 g/W. Even though slightly different tension and powers are applied, the tapered fibres all show low fibre losses.

Label	α(dB)	D_1-D_2(μm)	L_1-L_2-L_3 (mm)	P_s (W)	T_2 (g)	α_l^*(dB/cm)
fibre 5	6.0	125-49	3-7-3	70	30	0.5
fibre 6	6.0	125-49	3-7-3	69	37	0.5
fibre 7	6.0	125-49	3-7-3	68	40	0.5
fibre 8	6.0	125-49	3-7-3	67	56	0.5
fibre 9	6.0	125-49	3-7-3	66	66	0.5

TABLE 3.5: Recipes of fibre tapering for the first step(taper from 125 μm to 49 μm).

This can prove that filament powers which provide the maximum tension within the range between 30 g and 60 g can be suitable for conducting the first step. Hence, the power of 68 W was chosen as the fixed filament power at the first step tapering for the second step taper comparison.

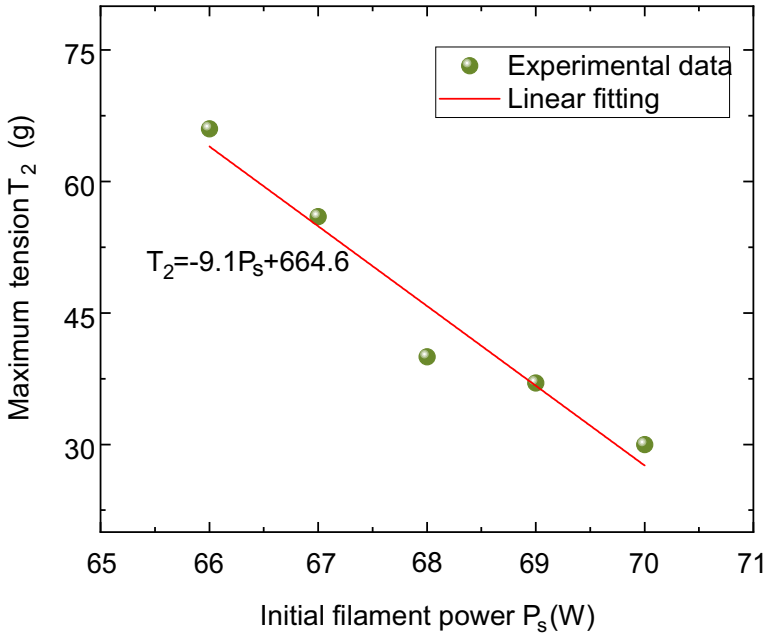

FIGURE 3.19: Measured maximum tension T_2 as a function of initial filament power P_s (taper from 125 μm to 49 μm).

By applying the same recipe for fibre 7 as found from the first step, another 7 fibres (10-16) were tapered in order to compare the second step recipe for small core SCF tapering. The parameters for all of them are seen in Table 3.6. To obtain tapered SCFs with core diameter around 960 nm, the waist diameter of the cladding will be around 9.6 μm. The aim of the second step is thus to taper the outer diameter of the fibres from 49.0 μm to 9.6 μm, with a tapering ratio as 5.1=49/9.6. To note, the Vytran limits the minimum diameter of original fibre for tapering as 80 μm. The second-step tapering can

still be realized by setting the Vytran to taper from 80 μm to 16 μm, considering that the targeted taper ratio of 5.1 will remain the same during the whole process.

Label	α(dB)	D_1-D_2(μm)	L_1-L_2-L_3 (mm)	P_s (W)	T_2 (g)	α_l^*(dB/cm)
fibre 10	high	80-16	3-5-3	59	0	high
fibre 11	high	80-16	3-5-3	58	7	high
fibre 12	high	80-16	3-5-3	57	14	high
fibre 13	8.7	80-16	3-5-3	56	20	1.7
fibre 14	8.8	80-16	3-5-3	55	22	1.8
fibre 15	high	80-16	3-5-3	54	30	high
fibre 16	high	80-16	3-5-3	52	36	high

TABLE 3.6: Recipes of fibre tapering for the second step (taper from 49μm to 9.6μm of the core diameter).

The input and output core diameter were all polished down to 4.6μm and 4.0 μm, respectively, and all the fibres had the same total length of about 9 mm. The total losses were measured as in the same method to test step-one. Table 3.6 shows that with the tension around 20 g, the tapered SCF has the lowest total losses. Higher or lower filament power P_s will result into fibres with high losses, which were above 13 dB. But both 56 W and 55 W could result in fibres with low losses. The total losses within the core diameter of 960 nm were ~8.7 dB and the linear losses were estimated to be ~2.0 dB/cm, assuming the coupling losses to be 7.0 dB. For powers higher than 59 W, break up of the core region appears, as seen in Figure 3.20(b), where Figure 3.20(a) shows the continuous core region as contrast.

Figure 3.21 shows the relation of measured maximum tension T_2 and the initial filament power P_s, while conducting the second tapering step. The linear fit shown as the red line is given using the OriginLab fit. The slope here is about -5.2 g/W. Both Figure 3.19 and Figure 3.21 show that T_2 linearly decreases with P_s within the tension range under 100 g, using the same tapering scheme. But the slope and the inception will change according to different taper profiles. It can be concluded that the suitable tapering range for tapering the SCF using J895 from 125 μm to 49 μm is between 30-60 g. In regard to tapering the fibre from 49 μm to 9.6 μm, tension values located around 20-22 g should be optimal. Appropriate filament powers can be found according to the relations pictured in Figure 3.19 and Figure 3.21 .

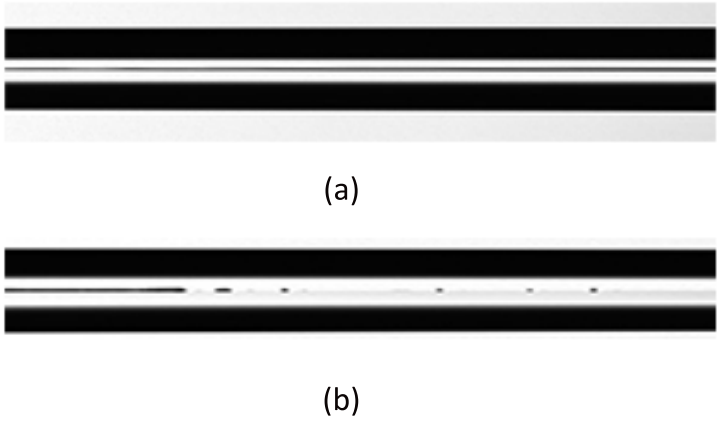

FIGURE 3.20: The topdown view from the Vytran. (a) Continuous core. (b) Breakup of the core.

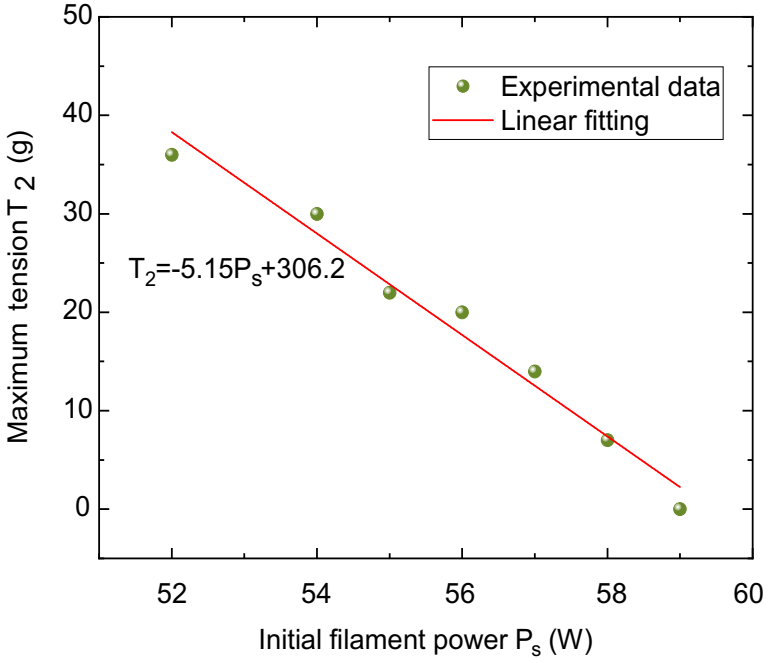

FIGURE 3.21: Measured maximum tension T_2 as a function of initial filament powerP_s for tapering the fibre from 49μm to 9.6μm.

3.6 Double-clad tapering

The starting point for double-clad tapering is to cleave about a 1 centimetre-long section of as-drawn SCF from the whole SCF roll, using a ceramic cleaver, before inserting it into a hollow core silica fibre (inner diameter of 150 μm and outer diameter of 400 μm). The hollow core silica fibre with a SCF inside is called a double-clad SCF. The tapering is then conducted with the SCF part of the double-clad SCF in the middle of the heated region. The double-clad method is useful as it helps to save the as-drawn SCFs material, as only 1 centimetre-long as-drawn SCF is consumed in the processing.

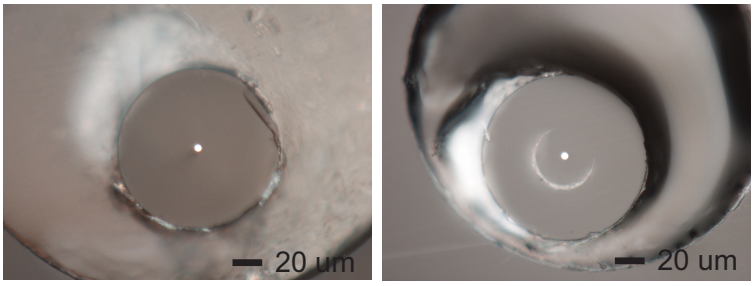

FIGURE 3.22: The end facets of double-clad SCFs

As the J895 fibres have cladding/core ratios of 10, in order to make a fibre with waist diameter of 950 nm, the cladding diameter will be only 9.5 μm. Such a small fibre is difficult to handle, and prepare for measurements, and they break quite often. They also bend when sleeved into capillaries sometimes, which increases the bending losses. Over-bending will break the fibre in the capillary when the wax in the capillary gets solidified or when pulling the fibre from the other side. In comparison, the double-clad tapering method helps to increase the cladding to core ratio by increasing the silica cladding diameter, and also provides more support for the small silicon core.

When using high powers for the tapering, the cladding of the SCF and the side walls of the hollow core fibre merge together, increasing the cladding-to-core ratio to 22-24. The polished fibre end facets of a double-clad fibre can be seen in Figure 3.22 (a). Even if the two claddings don't merge well and a gap still exists between them, the fibres can still be used. Figure 3.22 (b) shows an example of double clad fibres where the ratio was measured to be around 24. Therefore, in order to taper the fibre down to the core diameter of 950 nm, the cladding diameter can be around 21 μm to 23 μm. Handling fibres with these dimension will be less difficult in comparison to fibres with cladding diameter of 9.5 μm. Hence, one of the other benefits for using the double-clad method is because it raises the success rate of preparing these fibres for the transmission measurements.

The two-step tapering is also applicable for double-clad SCFs. Recipes of low loss tapered double-clad SCFs are given in Table 3.7, where the fibre profiles, filament powers P_s, and the maximum tension T_2 are given for comparison. Here, L is the total length of the polished fibre sample, and the linear loss α_l is estimated using the coupling losses of 7 dB. Table 3.7 presents results for tapers produced from double-clad SCF where the diameters are decreased from 400 μm to 125 μm, and then from 125 μm to desired diameter as the second step (~30 μm).

The structure of the two-step double-clad tapered fibre is seen in Figure 3.23. L_{01} is the waist length for the first-step tapered SCF and L_{02} is the total length for the second-step tapered SCF. L_{03} is the length between two transition areas before the second step starts. The schemes for preparing the two-step double-clad tapered SCF at the first step into a measurable sample is seen in Figure 3.23. As the unprocessed fibre for the

Label	α (dB)	L (mm)	α_l^* (dB/cm)	D_1 - D_2 (μm)	L_1-L_2-L_3 (mm)	P_s (W)	T_2 (g)
fibre 17	12	29	1.7	400-125	3-40-3	93	79
				125-30	3-25-3	50	40
fibre 18	9	15	1.3	400-125	3-20-3	95	40
				125-30	3-10-3	51	39
fibre 19	8	15	0.7	400-125	3-15-3	95	38
				125-26	3-10-3	52	37

TABLE 3.7: Recipes of tapered double-clad SCF (taper from 400 μm to 26-30 μm).

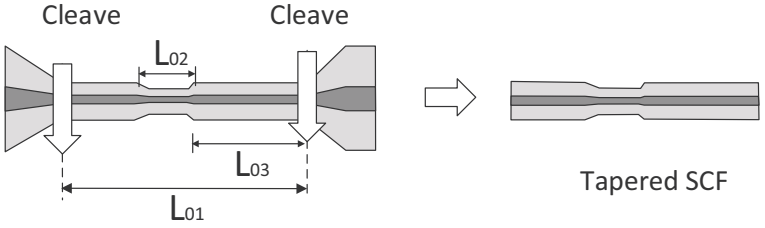

FIGURE 3.23: The first step of sample preparing for two-step double-clad tapered SCF.

double-clad SCF has the cladding diameter of 400 μm, larger than the inner diameter of 250 μm of the capillary, the unprocessed SCF and the transition areas obtained from the first-step tapering shall be cleaved off, before continuing the rest steps of the sample preparing. And L_{03} is generally designed to be slightly larger than L_{02}. The rest of the sample preparing steps are the same as shown in Figure 3.9.

A particular example for the sample preparation is given using the longest fibre 17. At the first step of tapering fibre 17, 40 mm was chosen to be the waist length L_{01}. Before starting the second step tapering, about 35 mm was set as L_{03} and then the total length for the second step tapering L_{02} was about 30 mm. Therefore, the length L_{01} of the waist region for the first step shall be designed to be much longer than the total length L_{02} at the second step, in order to leave room for L_{03}, which is the applied for all fibres 17-22. Moreover, the input and output core diameters of fibres17 to 20 were kept around 4.6 μm.

After measuring the core and cladding diameters of several double-clad tapered SCFs after polishing their end facets, the cladding-to-core ratio of these double-clad SCFs was calculated to be 23.0±1.0. After measuring the cladding diameter under the high-resolution microscope for both fibre 17 and fibre 18, their waist core diameters were

estimated to be around 1304±45 nm. The dimension for fibre 19 was estimated to be 1130±45 nm. Moreover, as it can been seen in Table 3.7, for the first step tapering, the tension T_2 between 30 g to 100 g is suitable for tapering double-clad SCF from 400 μm to 125 μm. And T_2 around 40 g shall be an optimal tension for the second step tapering of the double-clad SCF that needs to be tapered from 125 μm to smaller core dimension, less than 30 μm.

Label	α (dB)	L (mm)	α_l^* (dB/cm)	D_1 - D_2 (μm)	L_1-L_2-L_3 (mm)	P_s (W)	T_2 (g)
fibre 20	8	11	1.1	400-80	3-20-3	102	89
				80-23	3-6-3	58.5	53
fibre 21	7.5	10	0.5	400-80	3-20-3	105	81
				80-21	3-5-3	59	48
fibre 22	9.3	20	1.2	400-80	3-40-3	105	89
				80-19	3-15-3	60	51

TABLE 3.8: Design of tapered double-clad SCF (taper from 400 μm to 19-23 μm).

In addition, another group of recipes for the two-step tapering double-clad SCF is listed in Table 3.8, with the aim to taper SCFs with core diameters down to 1 μm. It shows the recipes for smaller SCFs by starting to taper from 400 μm to 80 μm as the first step. Because the filament temperature increases with time, the powers used for Table 3.8 were lower than in Table 3.7. Also the filament became less stable as it was older than in the previous tests. However, the tension T_2 is still a useful tool to look for the suitable filament powers when such a change happens. As after the first step, the cladding diameter for the waist is 80 μm with the core diameter of around 3.5 μm, the fibre after the second steps will only have the input and output core diameter of no more than 3.5 μm. Therefore, the final samples prepared for measurements following the step in Figure 3.23 were polished to have the input and output core diameters of 3.3 μm. The linear loss α_l is estimated using the coupling loss of 7 dB. Similar to fibre 17, the errors of the core dimensions shall be considered. The core diameters of fibre 20, 21 and 22 are estimated to be around 1000±45 nm, 913±45 nm and 830±45 nm, respectively. It is indicated that the tension suitable for the first step is between 30 g to 100 g for tapering from 400 μm to 125 μm and the second steps shall be around 37 g-40 g for tapering from 125 μm to 26-30 μm.

Chapter 4

Wavelength conversion using silicon core fibres

4.1 Introduction

Wavelength conversion is the key function in all-optical signal processing networks. Based on FWM, it has been demonstrated widely using the silicon waveguides [26, 29, 92, 93]. With the phase-matching condition met, FWM-based wavelength conversion can be realized, where the idler waves can be converted from the signal waves across a wide range either by tuning the signal wave or sometimes tuning the pump wave. The two main considerations to evaluate the effectiveness of wavelength conversion is the bandwidth and the conversion efficiency between the signal wave and the idler wave. This chapter starts with a discussion about the role of the silicon core fibre profile on the wavelength conversion when pumped by a continuous wave source. Then, the role of the length dependence is studied using two tapered silicon core fibres with the same design but different waist lengths. The experimental results are discussed with regard to the bandwidth and the maximum conversion efficiency. To further increase the conversion efficiency, a tapered silicon core fibre is produced with the longest waist length to date. Finally, the wavelength conversion is realized using this fibre, where the FCA is observed with the high pump power as the input. The explanation of the FCA in silicon core fibres with continuous wave pumped is briefly introduced based on the numerical simulations.

4.2 Impact of fibre profiles on wavelength conversion

FWM-based wavelength conversion is realized using continuous wave pump and signal waves, where the signal sees the conversion. The conversion efficiency (CE) of the

wavelength conversion is defined as the ratio between the output idler power and the input signal power. Under the assumption of an undepleted pump and a strong signal wave, CE can be expressed as [94],

$$CE = \frac{P_{\text{idler}}^{\text{out}}}{P_{\text{signal}}^{\text{in}}} = \left[\frac{\gamma P_{\text{p}}}{g}\sinh(gL_{\text{eff}})\right]^2, \tag{4.1}$$

where $P_{\text{idler}}^{\text{out}}$ is the output power of the idler wave, $P_{\text{signal}}^{\text{in}}$ is the input power of signal wave, and g is expressed in

$$g = \sqrt{\gamma P_{\text{pump}}\Delta k_L + (\Delta k_L/2)^2}. \tag{4.2}$$

In order to compare the bandwidth of the wavelength conversion, a 3 dB bandwidth is defined here, using the separation of signal and idler wavelength, when the conversion efficiency drops to half of its maximum value. To realize wavelength conversion in the silicon core fibres, the core diameter and length are the main two profile parameters that should be considered. The fibre core diameter will affect the dispersion properties, and thus the phase-matching conditions, and the fibre length will affect the effective length for parametric gain. At first, I simulated the conversion efficiencies, using two different core diameters, 850 nm and 915 nm, respectively, to explain the influence of the fibre core size on the wavelength conversion pumped in telecom band. The fibre length is set as 10 mm and the linear losses are estimated to be 2 dB/cm. The pump power is set as 18.5 dBm and different pump wavelengths are also considered.

Core diameter (nm)	**850**	**915**
A_{eff} (μm^2)	0.31	0.36
γ(W^{-1}m^{-1})	52.1	45.5

TABLE 4.1: Nonlinear parameters of the tapered SCFs at the wavelength of 1.55 μm.

Figure 4.1 shows the simulated conversion efficiency as a function of signal wavelength using different pump wavelengths, and hence GVD values for the 850 nm core diameter SCF. The nonlinear parameter is given in Table 4.1 at the pump wavelength of 1.55 μm as a reference. As the ZDW of 850 nm SCF is around 1.50 μm, the three pump wavelengths (1.53 μm, 1.55 μm and 1.57 μm) in telecom band are located in the its negative dispersion region. As these pump wavelengths are far away from the ZDW, the $|\beta_2|$ is large and the bandwidth will decrease with the increasing of $|\beta_2|$. The maximum conversion efficiency remains at the same value of -30.3 dB using these three pump wavelengths, which is determined by the input pump power. However, the maximum bandwidth achieved is 154 nm for the pump wavelength of 1.53 μm and the results show that the bandwidth decreases with increasing of $|\beta_2|$. Thus the longer pump wavelengths shorten the tuning

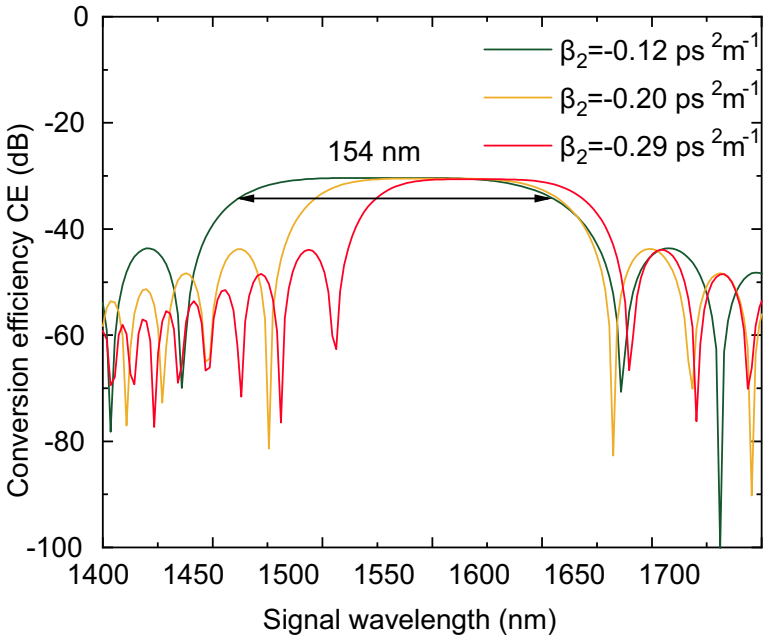

FIGURE 4.1: Conversion efficiencies of the simulated SCF with the core diameter of 850 nm as a function of signal wavelength, pumping at 1.53 μm, 1.55 μm and 1.57 μm, where $\beta_2 = -0.12\text{ps}^2/\text{m}, -0.20\text{ps}^2/\text{m}$ and $-0.29\text{ps}^2/\text{m}$, respectively.

range of wavelength conversion, plus the large $|\beta_2|$ creates more and denser side bands in the tuning curve.

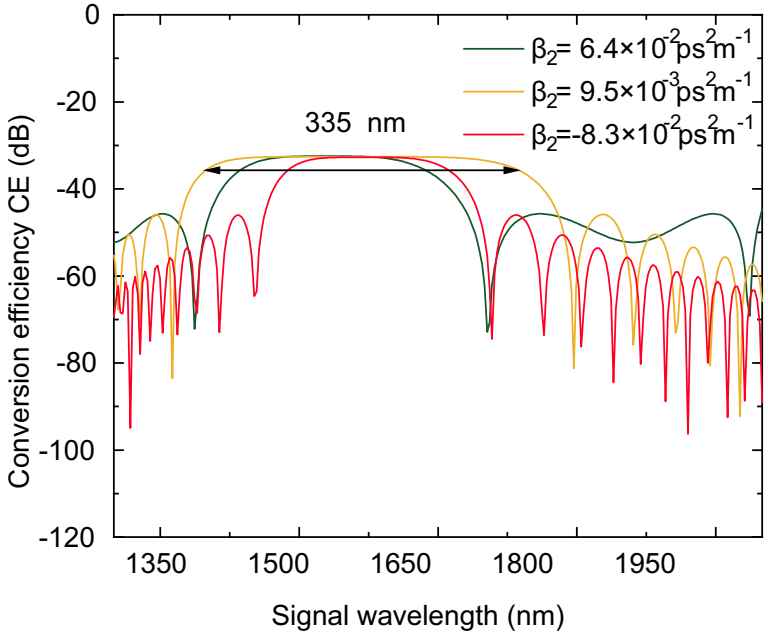

FIGURE 4.2: Conversion efficiencies of the simulated SCF with the core diameter of 915 nm as a function of signal wavelength, pumping at 1.53 μm, 1.55 μm and 1.57 μm, where $\beta_2 = 6.4 \times 10^{-2}\text{ps}^2/\text{m}, 9.5 \times 10^{-3}\text{ps}^2/\text{m}$ and $-8.3 \times 10^{-2}\text{ps}^2/\text{m}$, respectively.

The second SCF is then studied with a core diameter of 915 nm and its CE curves for different pump wavelengths is shown in Figure 4.2. The ZDW for this fibre is closer to the 1550 nm pump, at which the second order dispersion term is positive but rather small

with the value of 9.5×10^{-3}ps^2/m. With a small positive β_2, phase matching can be satisfied together with a negative β_4. The maximum conversion efficiency obtained here is -32.5 dB, which is lower due to the lower input pump intensities of larger core diameter. With pumping at 1.55 μm, the broadest bandwidth of about 335 nm is obtained, covering the whole telecom band. When tuning the pump wavelength from 1.53 μm to 1.57 μm, the bandwidth changes from 198 nm to 175 nm. It can be concluded here that with the same input pump power, SCF with smaller core size would exhibit higher conversion efficiency. However, if the fibre is pumped with its core size close to ZDW, a wider bandwidth can be obtained.

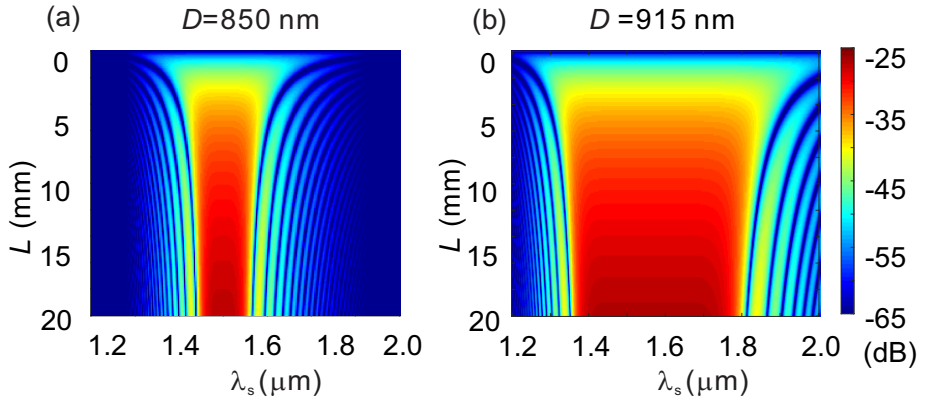

FIGURE 4.3: Conversion efficiencies of the simulated SCFs as a function of fibre length and signal wavelength, pumping at 1.54 μm with the core diameter of (a) 850 nm and (b) 915 nm.

Next, by changing the fibre length from 0 to 20 mm,the simulated conversion efficiency as a function of the SCF length and signal wavelength is plotted in Figure 4.3, when pumping at 1.55 μm using the 850 nm and 915 nm SCF core size, respectively. The input pump power is still set as 18.5 dBm. As shown in Figure 4.3(a) and (b), high-order phase-match bands can be observed in both SCFs. The conversion bandwidth increases from 154 nm to 370 nm, as the core diameter of SCF changes from 850 nm to 915 nm, when the tapered waist length is of 5 mm. The maximum conversion efficiency can reach ∼-30 dB when the SCF length is 10 mm, but the bandwidths are decreased to 126 nm with the core diameter of 915 nm . The highest conversion efficiency of ∼-25 dB can be obtained with the fibre length of 20 mm and the core diameter of 815 nm, but with a further reduction in the bandwidth. In general, a larger conversion bandwidth can be achieved but at a cost of lower conversion efficiency with the decreasing of fibre length.

In contrast, Figure 4.4 shows the contour map of conversion efficiency as a function of pump and signal wavelengths, with a SCF length of 10 mm. When high-order phase-match bands merge with the fundamental band, a maximum conversion bandwidth can be obtained. This can be realized by fine tuning the pump wavelength in the vicinity of the ZDW. As the submicron SCFs exhibit negative β_4 values over a pump wavelength

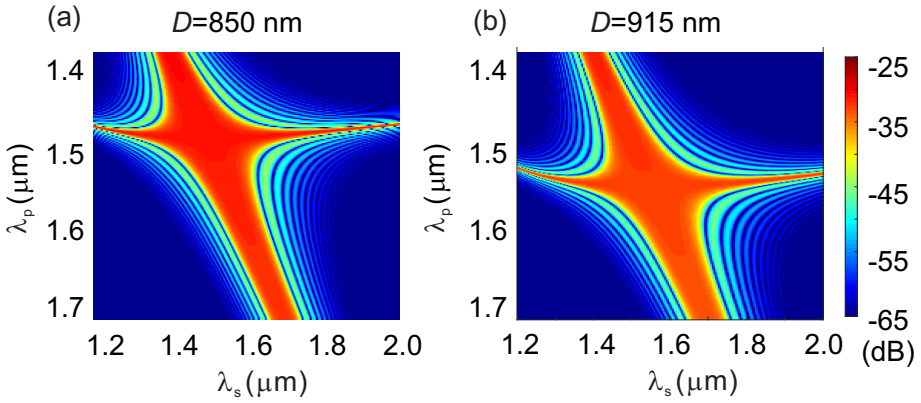

FIGURE 4.4: Calculated conversion efficiencies as a function of pump and signal wavelengths, with a fibre length of 10 mm with the core diameter of (a) 850 nm and (b) 915 nm.

range from 1400 nm to 1700 nm for both of these fibre core sizes, a 3-dB conversion bandwidth of over 60 nm is achievable across the entire tuning bandwidth.

4.3 Wavelength conversion in submicron silicon core fibres

4.3.1 Fibre design

Label	**Fiber I**	**Fiber II**
Waist diameter D_w (nm)	850	850
Waist length L_w (mm)	5	10
Total length L_0 (mm)	9	14
Input diameter D_{input} (μm)	5	5
Output diameter D_{output} (μm)	4.6	4.6
Total loss α (dB)	8.6	9.5
Linear loss α_l (dB/cm)	2.0	1.9

TABLE 4.2: Parameters for Fibre I and Fibre II.

As indicated by the results of the previous section, a SCF with a length of 10 mm can obtain both high conversion efficiency of ∼-30 dB and fairly broad bandwidth, more than 100 nm with continuous wave pumping at 1.55 μm. To verify this experimentally, two tapered SCFs with different waist lengths (5 mm and 10 mm) were fabricated to have core diameters around 915 nm for use as wavelength converters. The SCFs were labelled as Fibre I and Fibre II, respectively. The two step tapering method was applied here. At the first step, the as-drawn fibre J895 fibre was tapered from 125 μm to 49 μm with the filament power of 69 W, and then from 80 μm to 15 μm with the filament power of 56 W. The fibre profile parameters are listed in Table 4.2.

Fibre I and Fibre II include a uniform straight waist region, of a particular length, and two transition regions, the down-taper transition and up-taper transition, respectively. By maintaining relatively slowly varying transition regions, coupling between the various modes supported by the submicron-sized cores and/or the radiation modes of the cladding will be minimal. D_w is the silicon core diameter of the waist region, the actual core diameters are smaller than the target diameter of 915 nm. Even though the main goal is to achieve the core dimensions of 915 nm, the errors induced from the tapering method ended up with the actual core diameter of ~850 nm, measured under the microscope. The values for the total loss (α) of the SCFs were measured using a CW laser at a wavelength of 1550 nm. The linear losses (α_l) of the tapered waist were then estimated by subtracting the coupling losses (~ 7 dB) from the total loss and dividing by the length of the SCF. As it can be seen from Table 4.2, Fibre I and II exhibited linear losses lower than 2 dB/cm, which is the lowest losses obtained for the submicron silicon core fibres to date. As the crystallinity of the silicon core material has been shown to improve with decreasing diameter [54], this loss value represents an upper bound on the loss in the tapered waist, which is considerably smaller than the input and output transitions, and where nonlinear processing occurs.

4.3.2 Experimental setup of wavelength conversion

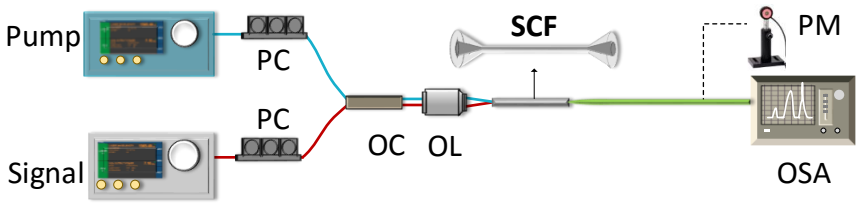

FIGURE 4.5: The experimental setup of FWM. PC, polarization controller; OC, optical coupler; OL, objective lens; TLF, tapered lensed fibre; OSA, optical spectrum analyser; PM, power meter.

Figure 4.5 shows the setup for the wavelength conversion experiments. The pump and signal beams are combined using a 3 dB optical coupler (OC), and then free space coupled into the tapered SCFs. Two polarization controllers (PC) are used to adjust the polarization of the two waves for optimising the conversion efficiency. In order to match the mode size at the input facet of the tapered SCFs, a 40× objective lens (OL) with $NA = 0.65$ was chosen to optimize coupling into the fundamental mode of the SCF [69]. No additional polariser was needed in the input coupling as the cylindrically symmetric SCFs are polarization insensitive. The output light is collected by a tapered lensed fibre (TLF, $NA = 0.40$), or a second microscope objective lens (OL2) with $NA = 0.85$. The output power was measured using a power meter (Thorlab S148C) and the spectrum recorded with an optical spectrum analyser (OSA Yokogawa AQ6370D), operating at a 1 nm resolution bandwidth. For wavelength conversion experiments, the pump source is

a tunable CW laser operating in the C-band. An erbium-doped fibre amplifier (EDFA) is used to boost the average pump power and a tunable band-pass filter (BPF) is used to suppress the amplified spontaneous emission (ASE) noise caused by the EDFA. To investigate the bandwidth of the wavelength conversion, a second tunable CW laser covering 1500 nm to 1680 nm is used as a signal wave.

4.4 Results and discussion

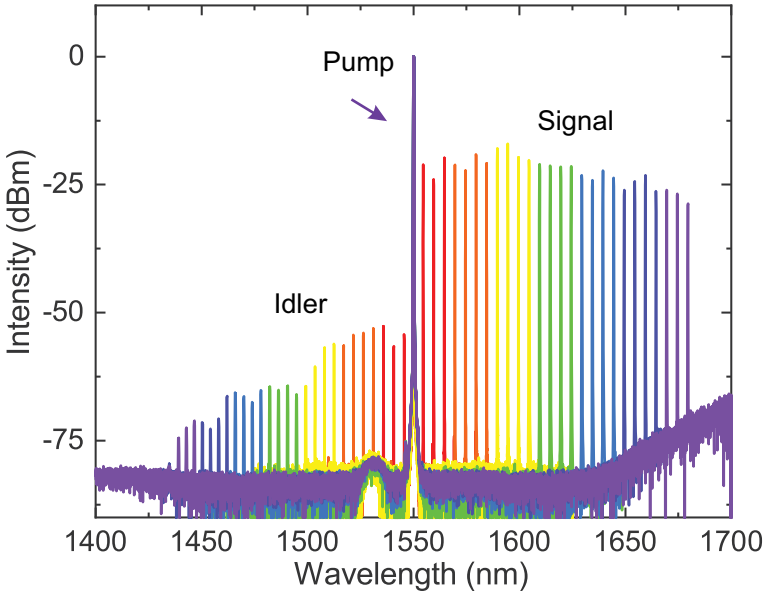

FIGURE 4.6: Measured spectra taken at the output of the SCF as the signal wavelength is tuned from 1555 nm to 1680 nm.

Figure 4.6 shows the spectra taken as the signal wavelength was tuned from 1555 nm to 1680 nm with the tuning step of 5 nm, when the pump wavelength was 1550 nm using Fibre I as a reference. Considering that the signal wave is strong and almost undepleted, the CE can be obtained directly from the readings of the peak powers of the signal and idler in the spectra, and calculated using Equation 4.1 for both signal wavelength tuning and pump wavelength tuning.

To investigate the optimum pump power for FWM wavelength conversion, the efficiency in Fibre II is plotted as a function of the coupled pump power with the signal wavelength set at 1560 nm in Figure 4.7. It can be seen that the conversion efficiency increases linearly from −61.0 dB to −31.2 dB as the coupled pump power is raised from 5.0 dBm to 20.0 dBm. The dashed line is the linear fit which has a a slope of 2. This corresponds to Equation 4.1, where CE is increasing with P^2 linearly, and therefore the relation of CE and P in dBm has a slope of 2. In comparison, Figure 4.8 shows that the CE remains constant when the signal power is varied from −11.1 dBm to 8.0 dBm for a pump power of 20.0 dBm, which suggests that the nonlinear losses are negligible at this power level.

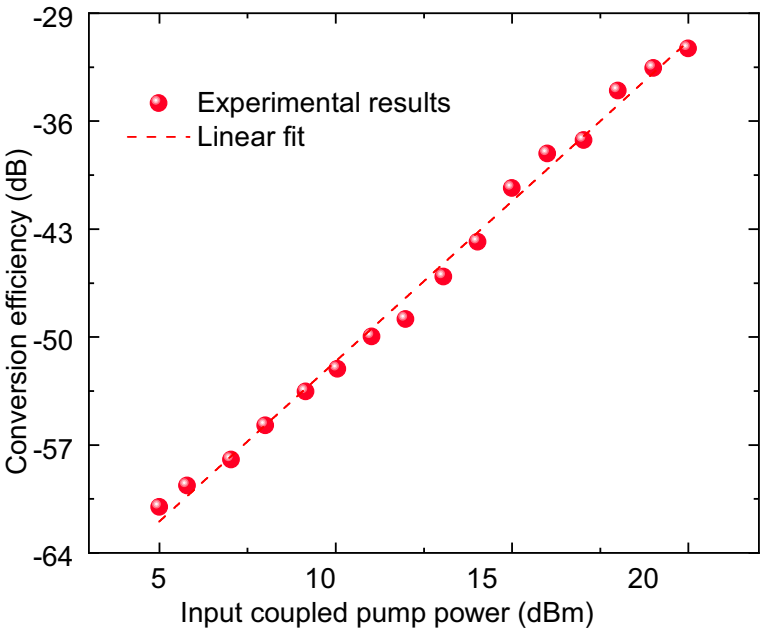

FIGURE 4.7: Conversion efficiency as a function of coupled input pump power with an input signal power of 9 dBm. The pump and signal wavelengths are 1550 nm and 1560 nm, respectively.

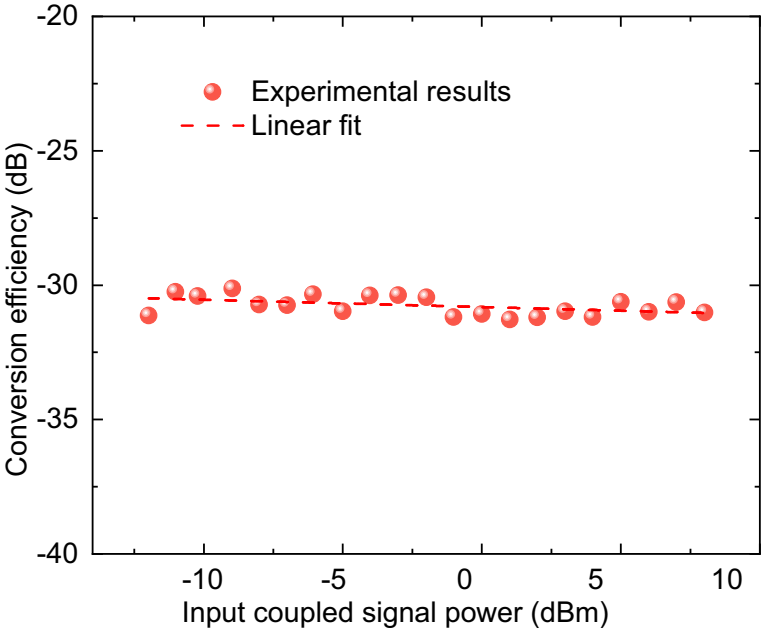

FIGURE 4.8: Conversion efficiency as a function of coupled input signal power with an input coupled pump power of 19.5 dBm. The pump and signal wavelengths are 1550 nm and 1560 nm, respectively.

To investigate and compare the FWM based wavelength conversion in two tapered SCFs, Fibre I and Fibre II, the idler waves were measured by tuning the signal wavelengths with a step of 2 nm. Figure 4.9 to Figure 4.11 display the measured CE dependent on the signal wavelength at three different pumping wavelengths 1540 nm, 1550 nm and

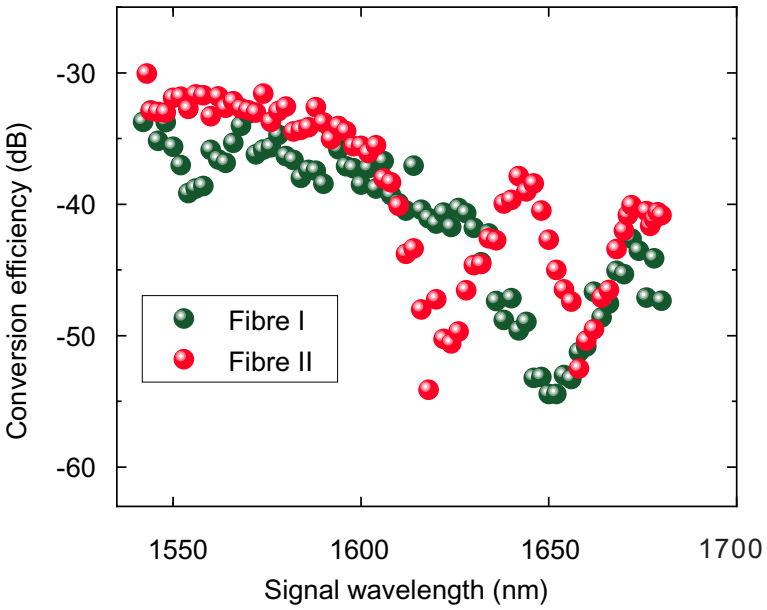

FIGURE 4.9: Measured conversion efficiencies as the signal wavelength which tuned from 1545 to 1680 nm with the tuning step of 2 nm, with the pump wavelength of 1540 nm using Fibre I and Fibre II.

1560 nm, where the coupled optical powers of the signals and the pump in the experiments were set to be −11.0 dBm and 20.0 dBm, respectively, to obtain the maximum conversion efficiency.

As it can be seen from these figures, wavelength conversion can be still observed when the low power CW signal is tuned to 1680 nm for the three pump wavelengths (1540 nm. 1550 nm and 1560 nm). Thus, these results suggest that broadband wavelength conversion (more than 260 nm) can be achieved in our tapered SCFs, covering the entire S-, C-, and L- telecom bands. Moreover, it is important to note that this experimental conversion bandwidth was only limited by the tuning range of our CW source. As can be seen from Figure 4.9, Fibre II exhibits largest 3 dB bandwidth of 144 nm when pumped at 1540 nm. As the pump wavelength moves further from its ZDW (1502 nm), the bandwidth reduces slightly to 122 nm at 1560 nm. This suggests that this SCF exhibits broad bandwidth when the pump wavelength is tuned in the most useful telecom C-band, owing to its relatively low GVD close to ZDW. In regards of Fibre II, the maximum conversion efficiency is higher than that of Fibre I for all three pump wavelengths. In spite of higher conversion efficiency obtained in Fibre II, its conversion bandwidth (∼120 nm) is narrower, due to walk-off between signal and pump waves caused by the longer fibre length, which supports the previous predictions in the numerical simulations as seen in Figure 4.3. Nevertheless, this conversion bandwidth is slightly larger than previous reports of FWM in silicon waveguides using a telecom pump source [24], except in the exotic silicon nano-waveguides. These waveguides were designed to have a 30-nm thin slab layer [10], where the height is 300 nm and the width is between 680 nm and 720 nm with its dispersion engineered.

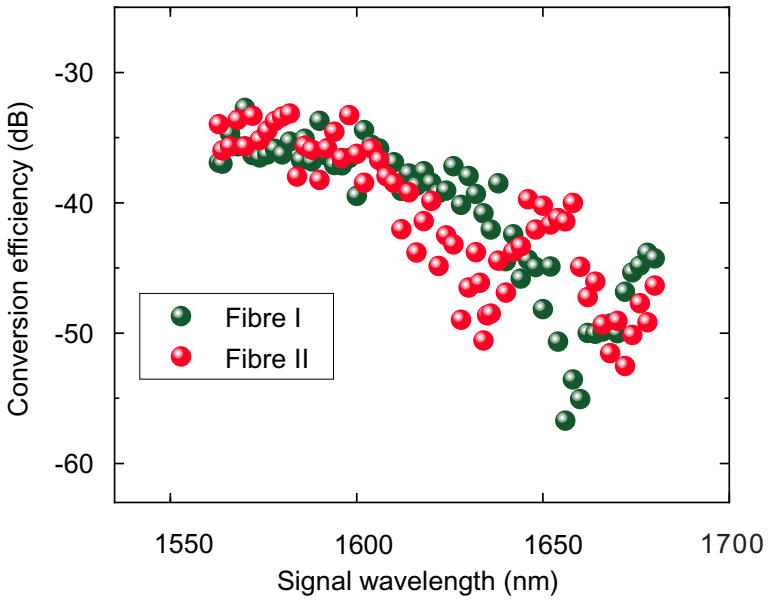

FIGURE 4.10: Measured conversion efficiencies as the signal wavelength which tuned from 1555 nm to 1680 nm with the tuning step of 2 nm, with the pump wavelength of 1550 nm using Fibre I and Fibre II.

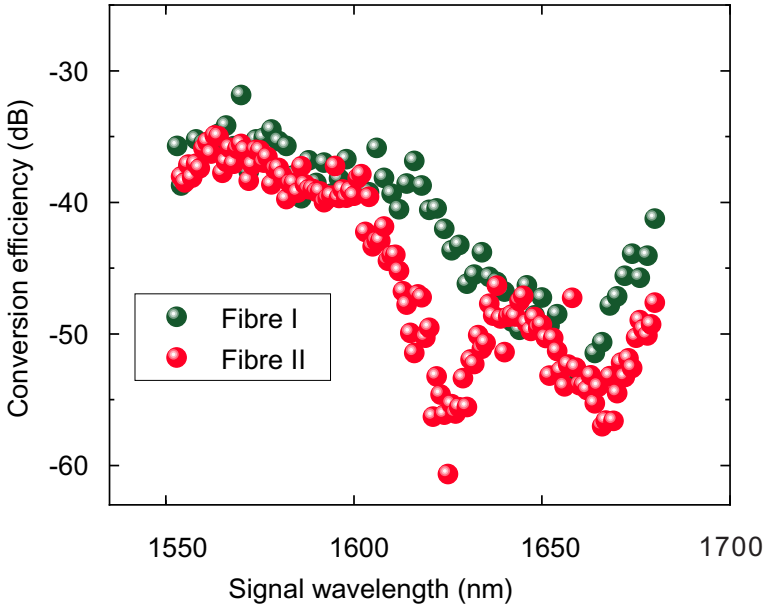

FIGURE 4.11: Measured conversion efficiencies as the signal wavelength which tuned from 1565 nm to 1680 nm with the tuning step of 2 nm, with the pump wavelength of 1560 nm using Fibre I and Fibre II.

In order to verify the relationship between the conversion efficiency and the the tapered SCF design, the theoretical conversion efficiency is then compared with the experimental results, using the calculated dispersion values of $\beta_2 = -0.17$ ps^2/m, $\beta_4 = -1.03 \times 10^{-5}$ ps^4/m at 1540 nm and $\beta_2 = -0.25$ ps^2/m, $\beta_4 = -0.95 \times 10^{-5}$ ps^4/m at 1560 nm. As shown by the shadowed areas in Figure 4.12, the main tuning band of the simulated curves are in reasonable agreement with the measured conversion efficiency. More side bands appear in Fibre I when pumped with 1560 nm and in Fibre II when pumped with

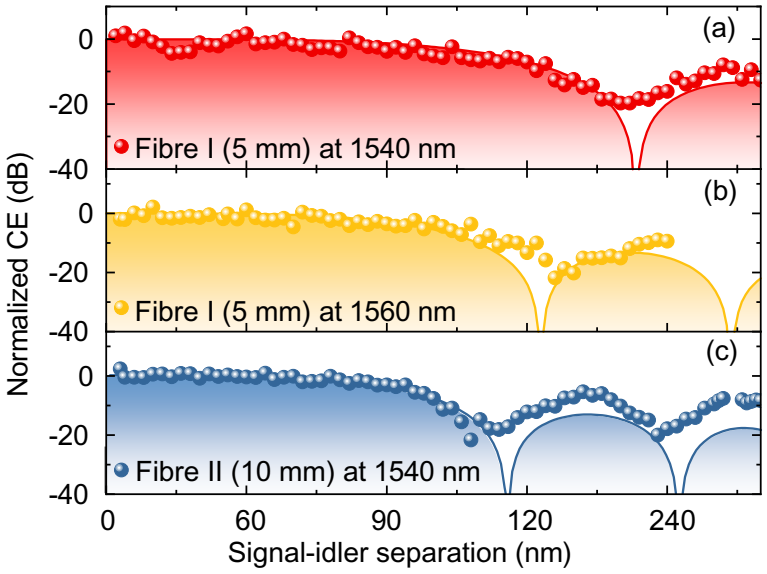

FIGURE 4.12: Measured FWM conversion efficiency (normalized) as a function of signal-idler wavelength separation for different tapered SCFs at selected pump wavelengths, given in the legend. (a) Fibre I (5 mm) pumped at 1540 nm, (b) Fiber I (5 mm) at 1560 nm, and (c) Fibre II (10 mm) at 1540 nm. Solid lines and shaded area show the simulation results.

1540 nm. The drop of the measured maximum conversion efficiency between the main band and the first side band is -10 dB, which is similar to the simulated results. However, the drop between the maximum CE and the first dip in the CE curve is only -20 dB, lower than the simulated results. We attribute this slight mismatch of the side bands to the discrepancies of the estimated FOD dispersion of the SCFs and the detection sensitivity of the OSA.

Label	**Fibre III**
Waist diameter D_{w} (nm)	800
Waist length L_{w} (mm)	15
Total length L_0 (mm)	19
Input diameter D_{input} (μm)	4.6
Output diameter D_{output} (μm)	4.6
Total loss α (dB)	12
Linear loss α_l (dB/cm)	2.6

TABLE 4.3: Parameters for Fibre III.

Considering that longer fibres should help to increase the maximum CE, seen from Figure 4.3, one more tapered SCF with a waist length of 15 mm was fabricated using the two step tapering method with a double cladding, and its parameters are listed in Table 4.3. For the first step, the double-clad fibre was tapered from 400 μm to 80 μm at the filament power of 95 W. In the second step, the fibre was tapered from 80 μm

to 19 μm with the filament power of 60 W. The fibre structure is similar to Fibre I and Fibre II that have the transition regions kept at the input and output facets. The core diameter was measured to be about 800 nm. The linear loss of Fibre III was then estimated to be about 2.6 dB/cm. The slightly higher losses may be induced by the instabilities of temperature control of the used tapering machine during tapering the long sub-micron SCFs.

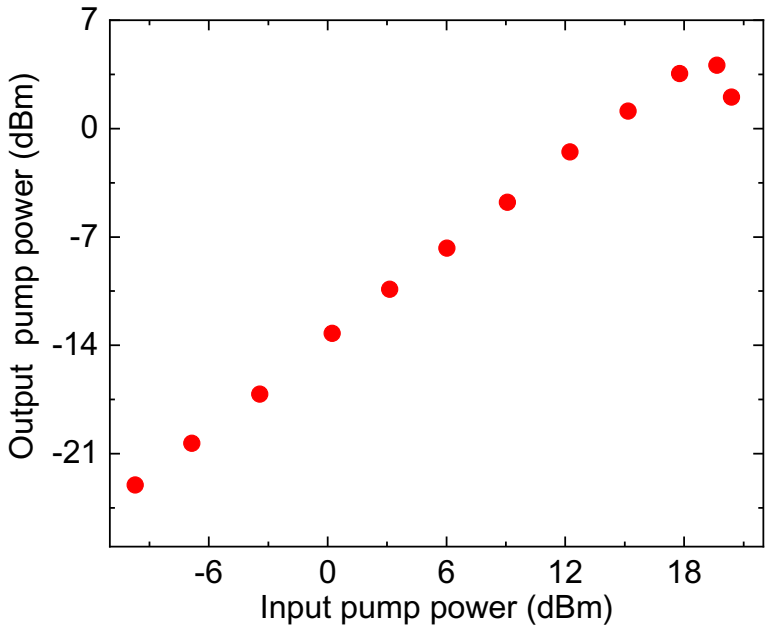

FIGURE 4.13: Measured output power as a function of the input pump power at the pump wavelength of 1550 nm for Fibre III

Using Fibre III, the wavelength tuning was conducted using the same setup seen in Figure 4.5 with the pump wavelength of 1550 nm. Figure 4.13 plots the output pump power as a function of the input coupled pump power. This shows that the nonlinear saturation begins when the input coupled power is more than 15 dBm. And when the input power increases to 16.7 dBm, the output power starts to drop and the total loss goes up by 3 dB. As TPA will be low, when using this level of pump power, we attribute the saturation effects to a build up of FCA associated with the CW pump. Because TPA-induced FCA will increase with a decrease in the core diameter of the silicon core fibre, Fibre III shows stronger FCA than the other two fibres, Fibre I and Fibre II.

Figure 4.14 displays the conversion efficiency as a function of the signal wavelength. It shows that the maximum CE reached is -34 dB, with the input coupled pump power of only 14.8 dBm, which is 5 dB lower than the input pump power(20 dBm) used for Fibre I and II. Assuming no nonlinear loss, if the pump power of 20 dBm was applied to Fibre III, we might expect that the CE could go up to -24 dB, because the CE is proportional with the pump power with the slope of 2. However, as displayed in Figure 4.13, increasing the pump power above14.8 dBm will induce absorption and not bring more enhancement to the conversion efficiency. In other words, using Fibre III, lower pump powers were

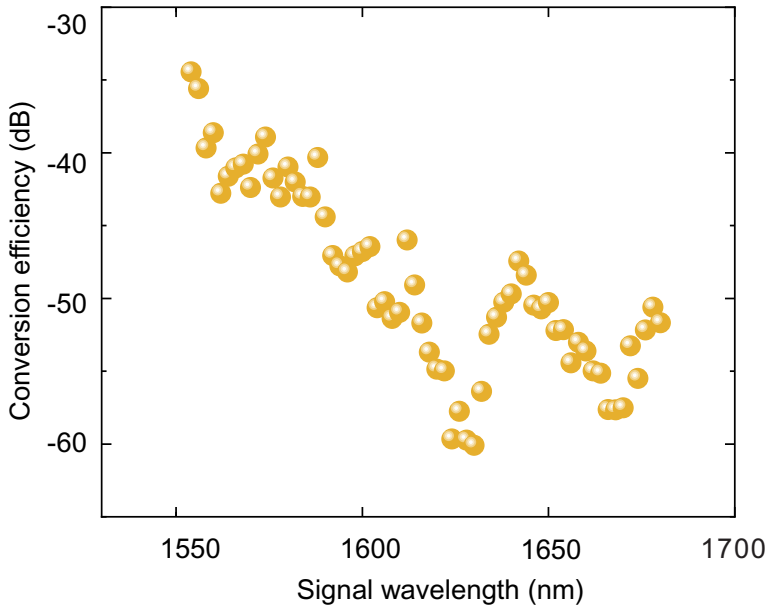

FIGURE 4.14: Measured conversion efficiencies for Fibre III as the signal wavelength is tuned from 1545 to 1680 nm, using tuning step of 2 nm and a pump wavelength of 1550 nm.

required to achieve the maximum CE of -34 dB benefiting from the longer length. But due to the stronger FCA associated with the smaller core, increasing the coupled input pump power any further will not result in an increase of the conversion efficiency.

Parameters	**SOI wire**	**SCF**	**silica-HNLF**
$\gamma(\mathrm{W^{-1}m^{-1}})$	~ 400	~ 45	$\sim 20\times10^{-3}$
$\mathrm{A_{eff}}$ $(\mu\mathrm{m}^2)$	~ 0.1	~ 0.36	~ 11
Propagation loss α_l (dB/cm)	< 1.1	< 3.0	$\sim 0.5\times10^{-5}$
L (mm)	~ 20	~ 20	$\sim 10^5$
Maximum CE (dB)	$\sim$ -10.5	$\sim$ -34	$\sim$ -13.5
P_{pump} (dBm)	~ 24.8	~ 14.8	~ 20
$\eta_{\mathrm{norm}}\%(\mathrm{W^{-2}mm^{-2}})$	~ 24.8	~ 10.9	$\sim 1.1\times10^{-4}$

TABLE 4.4: Comparison of optical parameters of: SOI wire, SCF common silica HNLF at 1.5 μm

Furthermore, for a better comparison of the results to other platforms and taking the device length L and the used pump power P_{pump} into consideration, a normalized efficiency $\eta_{\mathrm{norm}}$is defined as [95, 96]

$$\eta_{\mathrm{norm}} = \frac{100 \times CE}{P_{\mathrm{pump}}^2 L^2}. \tag{4.3}$$

In our case using Fibre III as example, $\eta_{\mathrm{norm}}\% = 10.9\%\mathrm{W^{-2}mm^{-2}}$. As listed in Table 4.4, our result is comparable to that of the SOI wire [24] as $24.8\%\mathrm{W^{-2}mm^{-2}}$, but

much higher than that of the common silica-HNLF [97] as $1.1 \times 10^{-4}\%\mathrm{W}^{-2}\mathrm{mm}^{-2}$, because much longer fibres were needed to achieve high conversion efficiency due to its low nonlinearity.

4.4.1 FCA consideration

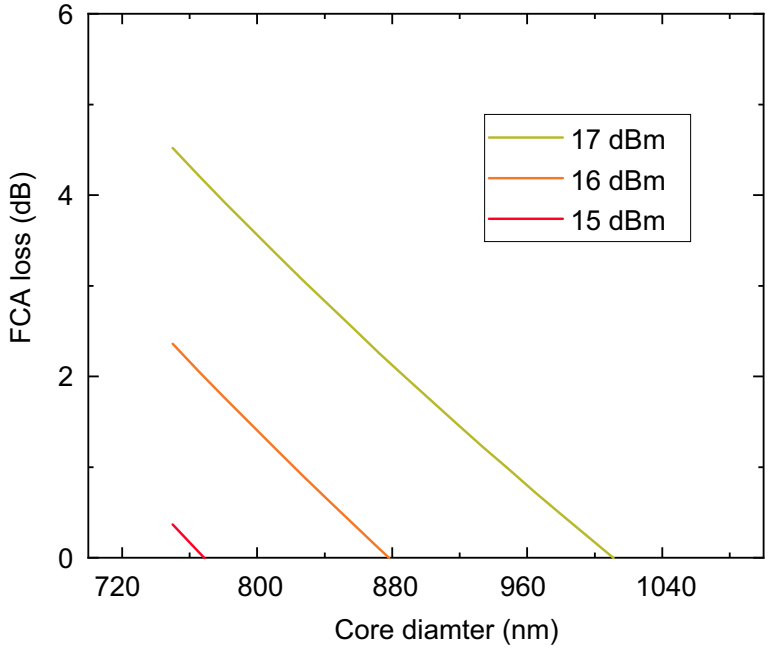

FIGURE 4.15: Calculated FCA dependent on the SCF core diameters, with the pump wavelength of 1.55 μm at different input pump powers shown in the legend.

To understand the effects of FCA on the wavelength conversion in SCF, some simulation work is conducted here. For continuous wave pumping of wave mixing in a SCF, the free carriers will eventually reach to a steady state. This can be expressed via Equation 2.60, where the loss induced by FCA is calculated as

$$\alpha_f = \sigma N_c(z) = \frac{\sigma\tau\beta_{\mathrm{TPA}} I_p^2}{2h\nu_0 A_{\mathrm{eff}}^2}. \tag{4.4}$$

It shows that the FCA increases with the input pump power but decreases as the effective mode area increases, which is dependent on the fibre core dimension. Assuming the free carriers life time is 1 ns and using the parameters in Table 5.1, the FCA induced loss can be calculated. Figure 4.15 shows the simulated FCA as a function of the SCF core diameter, using the pump power of 15 dBm, 16 dBm and 17 dBm, respectively. It can be seen from this figure that the FCA is negligible with the input powers of 15 dBm for SCFs with core sizes larger than 800 nm. Then it increases with increasing input pump power. For the input pump power of 17 dBm, FCA will reach 3.6 dB with fibre core of 800 nm but 1.5 dB with a 915 nm fibre. To reduce FCA, using either a larger SCF or a lower input pump power are desirable.

4.5 Conclusion

In this chapter, using continuous wave sources as the pump beams, the bandwidth of the FWM-based wavelength conversion with different fibre profiles was firstly calculated. The results have shown that broad bandwidth of the wavelength conversion can be obtained using fibres with ZDW near the pump wavelength. For pumping at telecom band, specifically for 1550 nm, SCF around 915 nm would perform the widest signal wave tuning. Long fibre lengths can help to increase the conversion efficiency. With the two-step method applied for tapering, two SCFs with core diameters of 850 nm, but different waist lengths (5 mm and 10 mm), were fabricated. By pumping at 1550 nm, we realized wavelength conversion covering the telecom bands, from S- to C- band, and the maximum conversion efficiency could be as high as -30 dB. To further improve the conversion efficiency, another SCF with a waist length of 15 mm and core diameter of 800 nm was tapered. The conversion efficiency in this SCF reached -34 dB with only half of the input power that was used for the other two fibres. However, the conversion efficiency could not be increased further via increasing the pump power due to the larger FCA in this SCF associated with the smaller core size.

Chapter 5

Optical parametric amplification using silicon core fibres

5.1 Introduction

Optical parametric amplification (OPA) using $\chi^{(3)}$ has been studied wildly using silicon waveguides [6, 9, 13, 27, 98]. This is known as FWM-based OPA. It allows the pump light that propagates in the medium to amplify the converted waves, signal wave (long wavelength) and idler wave (short wavelength), thus building high power light source with the wavelength aside the pump wavelength. Also, OPA has extensively been studied as a means to generate and amplify information [23]. In our silicon core fibres platforms, for obtaining the high parametric gain, the dispersive properties and the pulsed pump needs to be considered carefully. This chapter begins by introducing the coupled wave equations of FWM, which were used to conduct the simulation work and specifically to investigate the impact of free carrier absorption on the parametric gain, with regard to the pulsed pump nature. Next, the design used to realise a low-loss dispersion engineered silicon core fibre suitable for FWM-based OPA is presented for the chosen pulsed pump. Finally, the experimental results are compared with the simulations to determine the performance of the tapered silicon core fibre for FWM-based applications.

5.2 Impact of a pulsed pump on the parametric gain

5.2.1 Coupled wave equations for four-wave mixing

Similar to previous FWM-based OPA demonstrations in planar silicon waveguides, the properties of the pump pulse, mainly its pulse width and the repetition rate, have a significant impact on the parametric gain in the SCFs due to the presence of TPA and

FCA induced by TPA in the telecom band. Therefore, the study of the role of the pulse parameters would be helpful to choose a suitable pump source for obtaining high parametric gain in the FWM-based OPA experiments. In the case of degenerate FWM, assuming that the pump power has a much higher intensity than the signal wave and idler waves, it can be assumed to be undepleted. The coupled wave equations can be written as [99–101]

$$\frac{\partial A_p}{\partial z} + \frac{i\beta_{2p}}{2}\frac{\partial^2 A_p}{\partial t^2} = -\frac{\alpha_p}{2}A_p - \frac{\alpha_{fp}}{2}A_p + i\gamma_p \mid A_p \mid^2 A_p, \tag{5.1}$$

$$\frac{\partial A_s}{\partial z} + \frac{i\beta_{2s}}{2}\frac{\partial^2 A_s}{\partial t^2} = -\frac{\alpha_s}{2}A_s - \frac{\alpha_{fs}}{2}A_s + 2i\gamma_s \mid A_p \mid^2 A_s + i\gamma_s A_p^2 A_i^* \exp\left(-i\Delta k z\right), \tag{5.2}$$

$$\frac{\partial A_i}{\partial z} + \frac{i\beta_{2i}}{2}\frac{\partial^2 A_i}{\partial t^2} = -\frac{\alpha_i}{2}A_i - \frac{\alpha_{fi}}{2}A_i + 2i\gamma_i \mid A_p \mid^2 A_i + i\gamma_i A_p^2 A_s^* \exp\left(-i\Delta k z\right), \tag{5.3}$$

where A_j is the slowly varying amplitude (j=p, s, i), α_j represents linear losses for each wave, $\alpha_{fj} = \sigma_j N_c$ represents the TPA-induced FCA loss, where σ_j is the FCA coefficient, β_{2j} is the second order dispersion. The terms on the left-hand side of Equation 5.1 are related to the pump pulse dispersion. The propagation constants of the fundamental mode in the SCF can be calculated using the finite element method to solve the eigenvalue equation for fibre modes, with the appropriate wavelength dependent refractive indices for the silicon core and silica cladding, more details can be seen in Section 2.1.2. The terms on the right-hand side of Equation 5.1 are responsible for attenuation due to linear absorption and FCA, as well as the nonlinear processes of SPM and TPA, which are included in γ. Equation 5.2 and Equation 5.3 for the signal and idler beams are similar, but the second terms on the right-hand side are responsible for XPM and TPA and the last term describes the energy transfer between the interacting waves. The equation for the carrier density N_c is described as in Equation 2.61 and given here fore convenience as

$$\frac{dN_c(t,z)}{dt} = \frac{\beta_{\mathrm{TPA}}}{2h\nu_p}\frac{A_p^4}{A_{\mathrm{eff}}} - \frac{N_c(t,z)}{\tau_c}, \tag{5.4}$$

where τ_c is the free carrier life time. While using pulse pumping with a pulse width $T_0 \ll \tau$ (at the 1/e-intensity point), the repetition rate R and the pulse width T_0 are significant factors that will affect $N_c(t,z)$, which can be given by

$$N_c\left(t,z\right) \approx \frac{1}{1-e^{-1/R\tau_c}}\frac{\beta_{\mathrm{TPA}}T_0 A_p^4}{2h\nu_p A_{\mathrm{eff}}}. \tag{5.5}$$

Using the split-step Fourier method for the individual equations and the fourth-order Runge-Kutta solver to link the coupled-wave equations, Equation 5.1 to Equation 5.3 can be solved with the optical parameters of the SCF. As it is discussed in chapter 4, the SCF with core diameter of 915 nm has its ZDW located near 1.55 μm. Therefore, 915 nm is chosen as the diameter of the SCF in the simulations and its length is set as 5 mm. For simplification in the simulation work, only the straight waist region is considered,

without the transition regions. The other parameters used for solving the equations are shown in Table 5.1.

Parameter	**Symbol**	**SCF(unit)**
Central wavelength	λ	$1.55\,\mu$m
Linear loss	α_l	$2.8\,$dB/cm
Kerr effect coefficient	n_2	4.0×10^{-18}m^2/W
Carrier life time	τ	1 ns
FCA parameter	σ	1.4×10^{-21}m^2
TPA coefficient	β_{TPA}	4×10^{-12}m/W
Effective mode area	A_{eff}	0.4×10^{-12}m^2
Nonlinearity	γ	40.77 W^{-1}m^{-1}
Dispersion value	β_2	9.5×10^{-3}ps^{2}m^{-1}

TABLE 5.1: Linear and nonlinear parameters for SCF for simulation.

5.2.2 Simulation results and discussion

To obtain high parametric gain, the influence of the pulse duration on the maximum parametric gain together with the repetition rate is studied here, using simulation results. In the examples given here, the pump pulse has the central wavelength of $1.55\,\mu$m and the coupled input peak pump power is set to be 12 W. The input signal is a continuous wave with its wavelength tuned between $1.55\,\mu$m to $1.68\,\mu$m and its power is kept constant as 15 mW, which was the practical value of the tunable laser used in the future experiments. The pump and the signal are launched into the fibre at the same time.

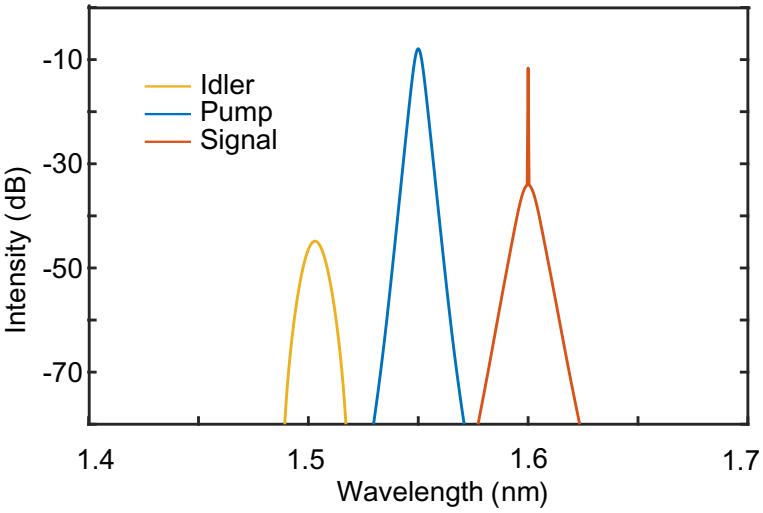

FIGURE 5.1: Simulated output spectra with the signal wavelength at $1.6\,\mu$m.

To begin with, Figure 5.1 shows simulated spectra at the output of the SCF. In order to calculate the amplified output signal pulse, the residual narrow-band continuous wave signal from the seed is first removed numerically by applying a 2 nm band-stop filter. Then the filtered time-averaged signal spectrum is converted using the pulse duty cycle factor $F = 1/(R \times T_0)$. As the conversion efficiency has the same increasing trend as the signal gain, the discussion below will focus on the parametric signal gains.

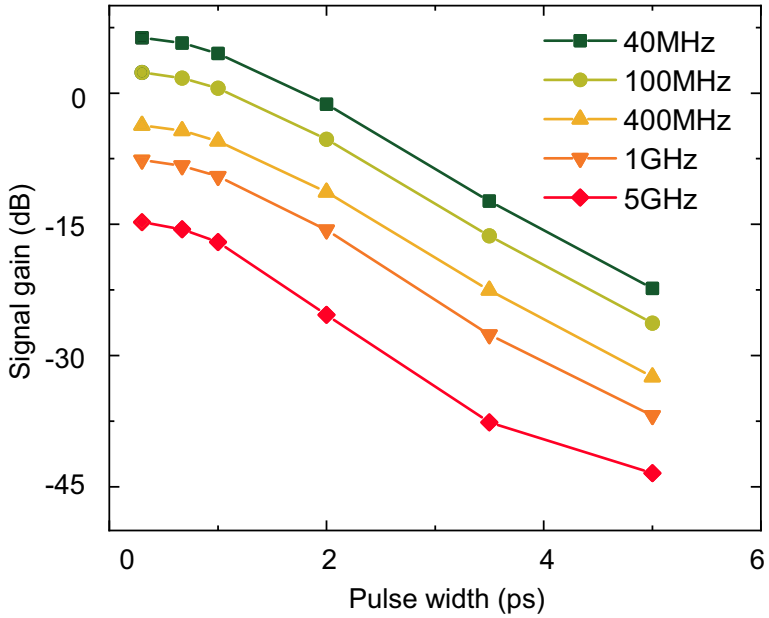

FIGURE 5.2: Signal gain as a function of pulse width, for five different pulse repetition rates (40 MHz, 100 MHz, 400 MHz 1GHz and 5 GHz), with the signal wavelength of 1.6 μm.

Figure 5.2 shows the signal gain dependence on the pump pulse widths for five different pulse repetition rates. As can be seen here, the maximum parametric gain appears with the pump pulse of the shortest pulse width at the lowest repetition rate. This can be explained via using Equation 5.5, that when $R\tau_c \ll 1$, the free carrier density is mostly dependent on the pulse width T_0 and it decreases with T_0. Under the relatively low repetition rate, free carriers produced have enough time to recombine before the next pulse comes, thus FCA will be relatively low and even negligible. However, for pulse widths that are longer than the carrier lifetime with high input peak power, the FCA will be significant as the free carriers created by the starting edge of the pulse will dampen the power at the pulse tail. Inversely, the free carrier absorption will remain relatively low for short pump pulses. To note that, modest pump power shall also be used to reduce TPA, thus decreasing the TPA-induced FCA [102].

When $R\tau_c$ is larger than 1, which means the repetition rate is high or the free carrier lifetime is long, there won't be enough time for the free carriers to get recombined before the next pulse arrives. The pump intensity would get reduced by the increasing e free carrier density, which will be the main obstacle to enhancing the conversion efficiency via increasing the pump power [103]. Figure 5.3 shows the parametric gain versus the

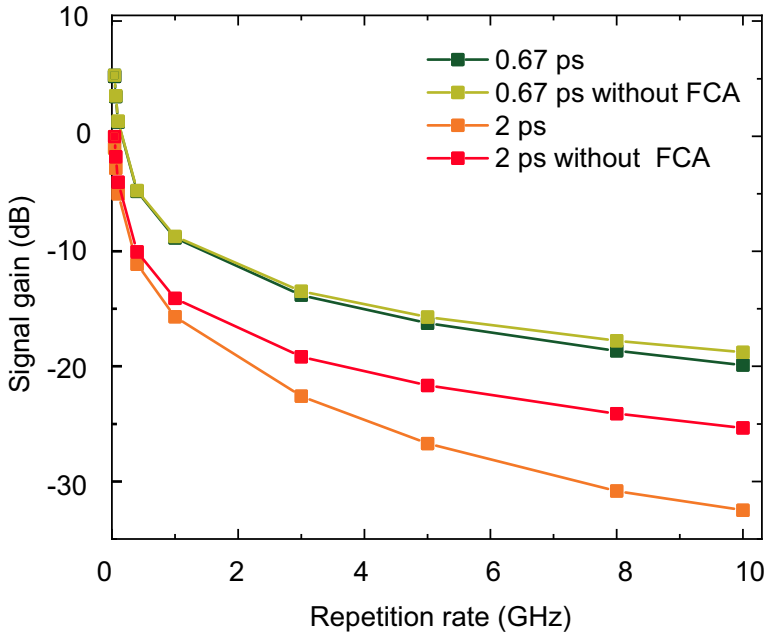

FIGURE 5.3: Calculated signal gain as a function of repetition rates at two pulse widths (0.67 ps and 2 ps) with FCA on and off at the pump wavelength of 1.55 μm and the signal wavelength of 1.6 μm.

pump repetition rates at two pulse widths (0.67 ps and 2 ps) with the FCA on and off, at the CW signal wavelength of 1.6 μm. It can be seen that, when an ultra short pulse is used, the FCA has no significant influence on the parametric gain. Even for the high repetition rates, FCA induced loss is only 1 dB. However, for the longer pulse width, such as 2 ps, the FCA will be a critical factor that affects the parametric gain when the repetition rate is larger than 1 GHz. Therefore, to increase the FWM-based optical parametric gain at a lower price of FCA, an ultra-short pulse widths will be desirable and a moderate pump power should be chosen. Alternatively, a long pump pulse but with relatively low repetition rate could also be considered.

5.3 Optical parametric amplification in submicron silicon core fibres

5.3.1 Fibre design

The fibre used in this work is labelled as Fibre IV. It was produced with input and output core diameters of 4 μm, which were tapered down to a target waist 915 nm over a length of $\sim$ 5 mm in the centre region, as illustrated in the inset of Figure 5.4. By optimising the tapering filament powers, and applying two-step tapering, Fibre IV was successfully tapered down to have a core waist diameter of $\sim$ 900 nm. For the first step, the SCF was tapered from 125 μm to 49 μm at the filament power of 68 W. In the second step, the fibre was tapered from 49 μm to 9 μm with the filament power of 52 W. Its properties

Label	Fibre IV
Waist diameter D_w (nm)	~915
Waist length L_w (mm)	5
Total length L_0 (mm)	8
Input diameter D_{input} (μm)	4.6
Output diameter D_{output} (μm)	4.0
Transmission α (dB)	9.5
Linear loss α_l (dB/cm)	2.8

TABLE 5.2: Parameters for Fibre IV

are given in Table 5.2. The total fibre length was 8 mm including the input and output coupling tapers. The propagation loss of the SCF at the 1541 nm pump wavelength was estimated to be ~ 2.8 dB/cm, by subtracting the input ~ 4 dB and output ~ 3 dB coupling efficiencies from the total 9.2 dB transmission loss, as the output has larger core size thus, less mode mismatch losses. This propagation loss represents a relatively low value reported for a sub-micron SCF [53] and indeed, any planar polysilicon waveguide of similar dimensions in the telecom band [104]. Moreover, as the crystallinity of the core material has been shown to improve with decreasing diameter [53], we expect that this loss value represents an upper bound on the loss in the tapered waist, where the nonlinear processing occurs.

5.3.2 Experimental setup of optical parametric amplification

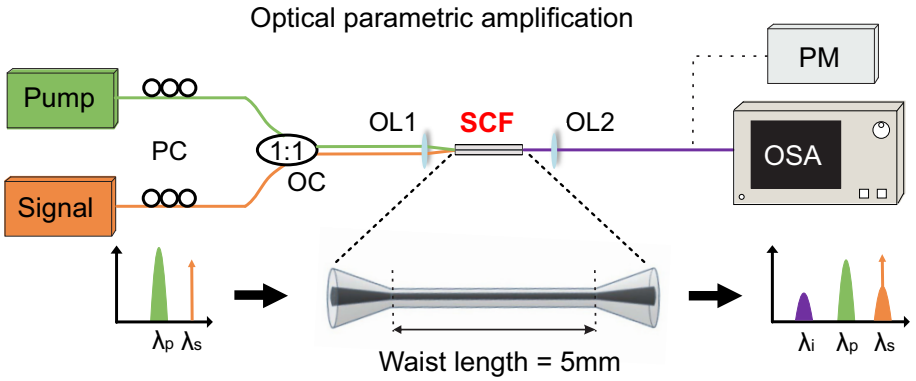

FIGURE 5.4: Schematic of the experimental setup. PC: polarization controller. OC: optical coupler. OL: objective lens. OSA: optical spectrum analyser. PM: power meter. Inset, symmetric tapered SCF profile.

The experimental setup for OPA within Fibre IV is depicted in Figure 5.4. Based on the study in Section 5.2.2, a short pulsed pump source with low repetition rate was chosen. It was a mode-locked erbium doped fibre laser emitting pulses centred at 1541 nm with a

670 fs full-width at half-maximum (FWHM) duration, corresponding to a 3 dB spectral bandwidth of ~ 7 nm (transform limited), and a repetition rate of 40 MHz. A tunable CW laser was used as the signal beam, with a tuning range covering $1570 - 1680$ nm. Two polarization controllers (PCs) were used to align the linearly polarized pump and signal beams to optimize the conversion efficiency. The pump and signal were combined by a 3 dB optical coupler before free space coupling into the SCF. The input coupling was achieved with a microscope objective lens (OL1) with a NA of 0.65, which was chosen to optimize coupling into the fundamental mode [69]. No additional polarizer was needed at the input stage as the cylindrically symmetric SCF is polarization insensitive, which was confirmed by monitoring the output signal power when changing the polarization of the combined input pump and signal beams. The output light was collected by a second microscope objective lens (OL2) with a NA of 0.85 and directed either to a power meter or focused into an optical spectrum analyser (OSA YOKOGAWA AQ6370D). All the spectra were measured with a 1 nm resolution bandwidth of the OSA. It is worth noting that, owing to the high nonlinearity and improved coupling efficiency of the tapered SCF platform, we do not require any additional amplification stages for our pump and signal beams, simplifying the setup and helping to reduce noise levels. All the optical powers were measured by a power meter (Thorlab PDA20H).

5.4 Results and discussion

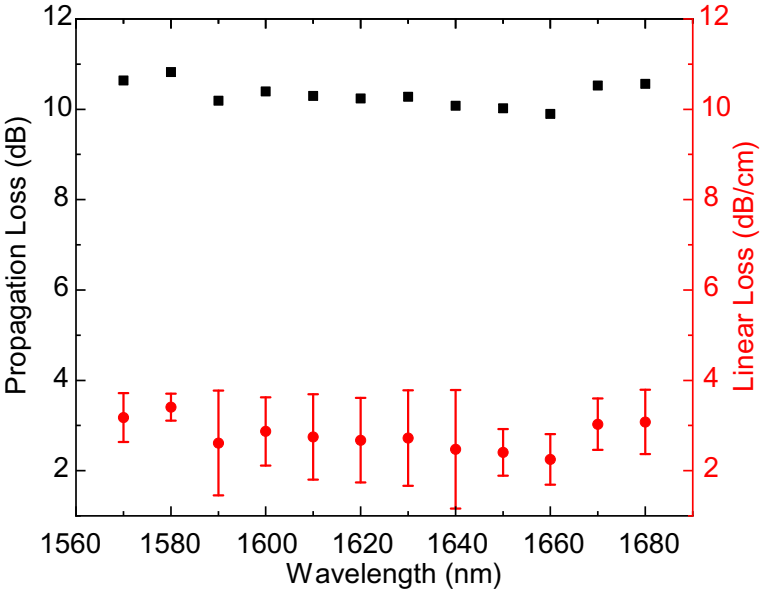

FIGURE 5.5: Transmission properties of the Fibre IV at different wavelengths from 1570 nm to 1680 nm.

Firstly, to characterise the transmission properties of Fibre IV, the insertion loss of the device was measured for signal wavelengths between 1570 nm to 1680 nm, using the low power CW laser source, as shown in Figure 5.5. The black squares are the

measured propagation losses and the red dots are the estimated linear losses. The transmission of the fibre was then estimated by excluding the ∼4 dB input and ∼3 dB output coupling losses induced from mode mismatch and facet reflection. The large error bars are due to inconsistent coupling losses that vary for the different input wavelengths. It can be seen that the insertion losses are between 10 dB to 11 dB and linear losses are fairly constant over the entire signal wavelength range, averaging ∼ 3 dB/cm. Using

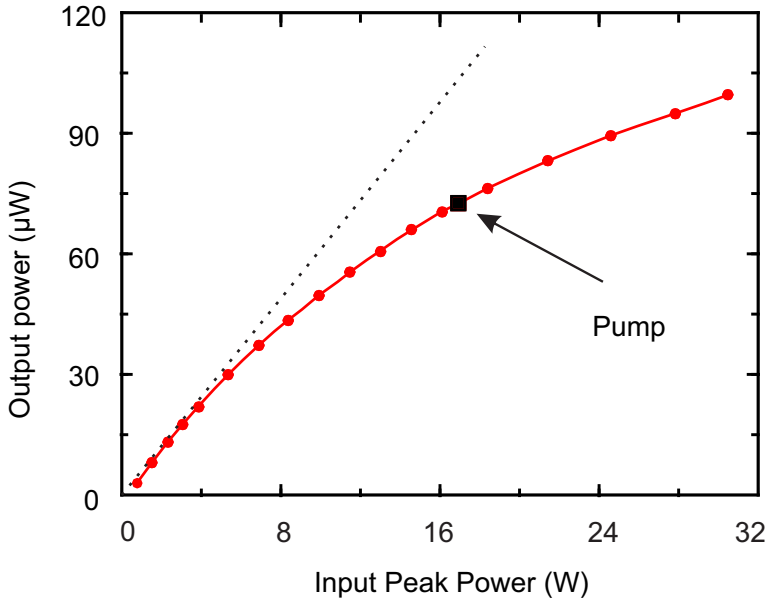

FIGURE 5.6: Measured transmission as a function of input peak pump power. The red curve is the simulated transmission including nonlinear loss from TPA. The dash line (black) indicates the linear insertion loss.

the same experimental setup, the nonlinear transmission properties of Fibre IV were then measured at the pump wavelength, seen in Figure 5.6. In order to minimize the effects of nonlinear absorption and spectral broadening of the pump, a moderate coupled average power of ∼ 0.63 mW (∼ 17 W peak power) was chosen, just below the saturation threshold.

FWM-based OPA was then investigated by simultaneously injecting the pump pulses with low power CW signals (> 1 mW) at different wavelengths. Figure 5.7 shows the optical spectra generated by the degenerate FWM process, with signal wavelengths from 1570 nm to 1680 nm overlaid. Owing to the use of a pulsed pump, the amplified signals and generated idlers also occur as a train of short pulses, which is evident from their broad bandwidths, seen in Figure 5.7. These results clearly show that the signal can be down-converted by ∼ 260 nm (32 THz), from 1680 nm to 1420 nm, covering the entire S-, C- and L- telecom bands. It is important to note that this experimental conversion bandwidth was only limited by the tuning range of our CW source and it should be possible to extend this over the full ∼ 380 nm, as predicted by Equation 2.58. Nevertheless, this conversion bandwidth is larger than previous reports of OPA in silicon waveguides using a telecom pulse pump source, thanks to the low GVD, and the bandwidth could

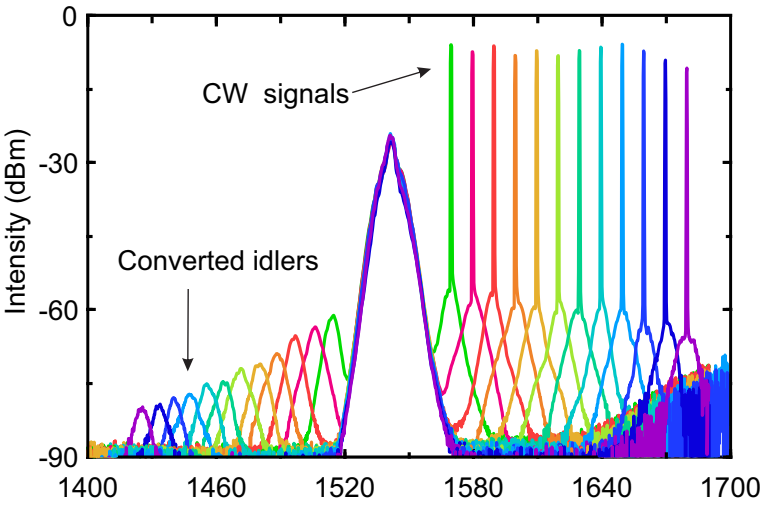

FIGURE 5.7: Transmission spectra taken at the output of the SCF as the signal wavelength is tuned from 1570 to 1680 nm.

be further improved by carefully tailoring the core diameter to reduce the FOD at the pump wavelength, seen in Equation 2.58.

The method used to extract the conversion efficiency from the measured spectra is explained below, and follows the same method described in Ref [9,28,105]. To understand the approach easily, all the powers are expressed in dBm. As the units used is in dBm, the multiplication factors in the expressions can be switch to additions, which makes this process easier to understand. Generally, the time-averaged powers of signal/idler $P_{\text{avg\_signal/idler}}$ can be obtained by integrating the average power distributed of the wavelength $P_{\text{avg\_OSA\_signal/idler}}(\lambda)$ from the spectra in Figure 5.7. Then the peak power of signal/idler is obtained by

$$P_{\text{peak\_signal/idler}} = F + P_{\text{avg\_signal/idler}} = F + \left(\int P_{\text{avg\_OSA\_signal/idler}}(\lambda) d\lambda \right), \quad (5.6)$$

where $F = 1/(R \times T_0)$ is the duty cycle factor, and in the unit of dB, is written as $F = 10\log\left(1/(40\text{ MHz} \cdot 670\text{ fs})\right)$, due to the pulsed nature of our pump wave. Again a 2-nm wide band-stop filter was numerically used for the time-averaged signal spectrum to exclude any remaining power from the CW wave. For signal wavelengths close to the pump (1570 nm, 1580 nm and 1590 nm) shown in Figure 5.7, where the amplified outputs overlap with the pump, the output signal and idler spectra are reconstructed assuming that they are symmetric. The output CW signal power was measured with the pump off, denoted as $P_{\text{signal\_out\_pump\_off}}$, which is then converted to the input signal power $P_{\text{signal\_in}}$ by

$$P_{\text{signal\_in}} = P_{\text{signal\_out\_pump\_off}} + \alpha, \quad (5.7)$$

where α in dB is the measured propagation loss through the 8 mm fibre, which is dependent on the signal wavelength, as seen in Figure 5.5.

Considering that the OSA attenuates the measured optical power for protecting the sensitive components, the spectra in Figure 5.7 only displays the relative power within each wavelength. Therefore, we used the pump power as a reference for obtaining the loss due to both the OSA attenuation and the coupling losses from free space to the OSA at each signal wavelengths measures. Then we denoted the whole losses as α_{OSA} in dB, which is expressed as

$$\alpha_{\mathrm{OSA}} = P_{\mathrm{meaured\_pump}} - P_{\mathrm{avg\_pump\_OSA}}, \tag{5.8}$$

where $P_{\mathrm{meaured\_pump}}$ is the measured average output pump power in free space after the output objective lens and $P_{\mathrm{avg\_pump\_OSA}}$ is the integrated averaged power of the spectra obtained from the OSA. Then, the output power of the idler wave $P_{\mathrm{idler\_out}}$ and that of the signal wave $P_{\mathrm{signal\_out}}$ were obtained by taking into account both the loss of the OSA and the propagation loss by

$$P_{\mathrm{idler\_out/signal\_out}} = P_{\mathrm{peak\_idler/peak\_signal}} + \alpha_{\mathrm{OSA}}. \tag{5.9}$$

Finally, the idler gain η of the idler wave is defined as the difference between the peak power of the idler wave and the input signal wave, by $\eta = P_{\mathrm{idler\_out}} - P_{\mathrm{signal\_in}}$. The on-chip parametric gain is obtained by $G = P_{\mathrm{signal\_out}} - P_{\mathrm{signal\_in}}$. Error bars were derived from the uncertainties in the propagation loss and the contribution of the OSA noise accumulated when integrating the signal/idler power.

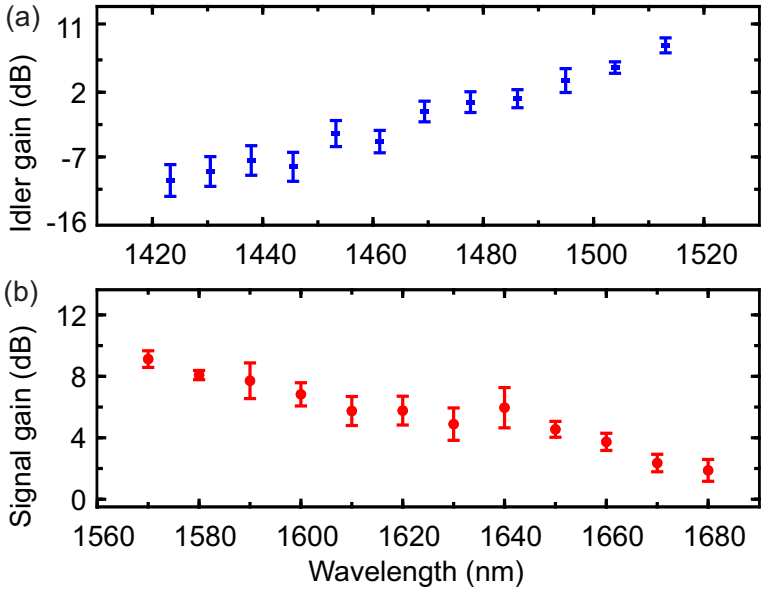

FIGURE 5.8: Idler conversion gain (a) and on/off parametric signal gain (b) as a function of wavelength. The error bars in the parametric gain data are derived from the uncertainty in the total propagation loss and the OSA noise.

The extracted values of the parametric signal gain and idler conversion gain are plotted in Figure 5.8(a) and (b), respectively. The experimental data reveal that a large

maximum on/off signal gain of $\sim 9\,\text{dB}$ is achieved at a wavelength of 1570 nm, with a corresponding idler conversion gain of $\sim 8.5\,\text{dB}$. Such a large on/off parametric signal gain in our tapered SCF is sufficient to overcome the moderate fibre insertion losses (7 dB), demonstrating a 2 dB net off-waveguide gain. The maximum signal gain obtained in our 8 mm long SCF exhibits more than a 3 dB improvement over the current highest record in a 17 mm nanophotonic silicon waveguide in the telecom band, which was obtained with a picosecond pulsed pump [9]. We attribute this increased gain to the lower overall losses in our system, which is due in part to the larger core size of the fibre, and also the reduced free carrier absorption associated with our shorter pump pulses. For both the signal and idler beams, the gains decrease as the signal wavelength moves away from the pump, which follows the theoretical predictions for waveguides pumped in the normal dispersion region [101, 106]. Although the maximum measured idler conversion gain is also higher than previous reports, it is slightly lower than the signal gain, which we attribute to the larger linear losses at the shorter wavelengths for polysilicon fibers [107].

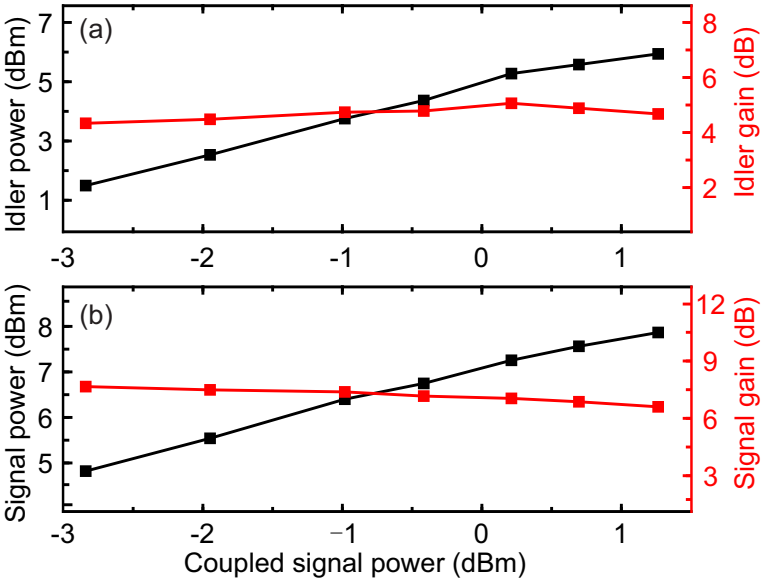

FIGURE 5.9: (a) Measured amplified idler power (black) and conversion gain (red) as a function of signal power (1590 nm) at the SCF output. (b) Measured signal power (black) and gain (red) as a function of signal power (1590 nm) at the SCF output.

Additional experiments were carried out to investigate the gain dynamics with the signal wavelength set at $\lambda = 1590\,\text{nm}$, so that both the signal and idler beams were far away from the pump bandwidth. In the regime of negligible nonlinear losses, the parametric gain should remain constant when the signal power is varied. This can be seen from the linearly increasing trend of the idler and signal output powers as the coupled signal power is raised from -3 dBm to 1.3 dBm, as shown by the black lines in Figure 5.9(a) and (b), respectively. The slope efficiency, plotted as the red curves in Figure 5.9(a) and (b), represent the idler and signal gains as a function of power, which yield values of $\sim 4.8\,\text{dB}$ and $\sim 6.5\,\text{dB}$, with a fluctuation of less than 1 dB. These measurements

reveal that there is no significant gain saturation in Fibre IV for peak pump powers up to $\sim 17\,\mathrm{W}$, which are easily attainable using conventional cost-effective fibre lasers, and the powers could be reduced further by increasing the SCF length.

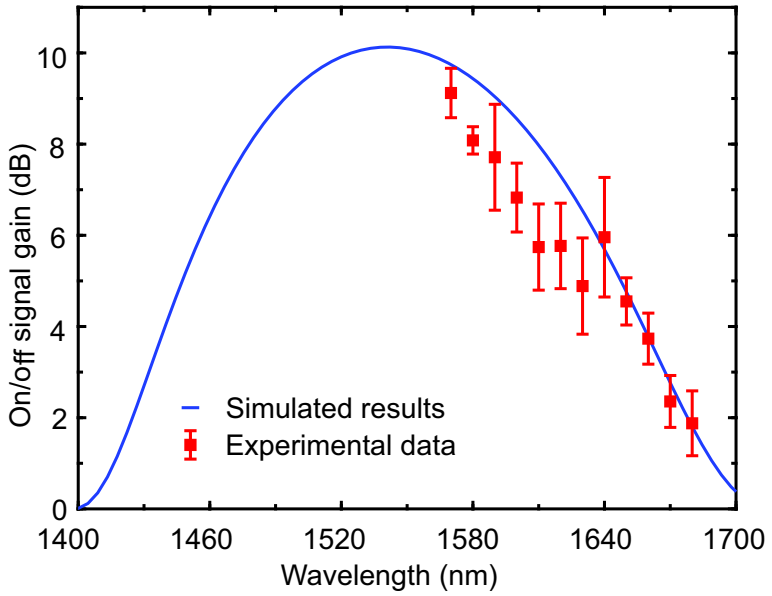

FIGURE 5.10: Calculated (blue solid line) and measured (red squares) on/off signal gain as a function of signal wavelength, using a pump with $\sim 17\,\mathrm{W}$ peak power centred at 1541 nm.

As a final comment, in order to understand the relationship between the on/off parametric signal gain and the dispersion properties of Fibre IV, the measured gain is replotted as a function of signal wavelength in Figure 5.10 (red squares). Here, we neglected FCA due to the use of a sub-picosecond pump pulse with a low repetition rate. This gain distribution can be compared with the theoretical predictions for the signal gain as [23] [94] with the assumption of an undepleted pump. The parametric gain for signal wave can be then expressed as

$$G_s = \frac{P_s(L)}{P_s(0)} = 1 + \left[\frac{\gamma P_\mathrm{p}}{g}\sinh(gL_\mathrm{eff})\right]^2, \tag{5.10}$$

where $P_s(L)$ is the signal power at the fibre output facet, $P_s(0)$ is regarded as the input signal power, and $L_\mathrm{eff} = (1 - \exp(-\alpha \mathrm{L})/\alpha$ is the effective fibre length, taking into account the linear propagation loss α. The parametric gain coefficient g is given in Equation 4.2. The signal gain was calculated by substituting the values in the Table 5.1 and the dispersion parameters (β_2 and β_4) into Equation 5.10. However, instead of fixing the values of β_2 and β_4 to those obtained from Figure 2.10, here we leave them as free parameters to achieve the best fit to the experimental data. The blue curve plotted in Figure 5.10 was obtained with the estimated values $\beta_2 \sim 0.042\,\mathrm{ps}^2\,\mathrm{m}^{-1}$ and $\beta_4 \sim -0.3 \times 10^{-5}\,\mathrm{ps}^4\,\mathrm{m}^{-1}$, corresponding to a coefficient of determination $\mathrm{R}^2 \sim 0.8$ which agree well with the calculated dispersion parameters assuming the target core diameter of 915 nm.

We attribute the discrepancy between the fitted curve and the measured gain at the wavelengths close to the central frequency of the pump to difficulties in calculating the peak signal power when the signal and pump bandwidths overlap, resulting in an underestimation of the gain in this region. Nevertheless, such agreement is fairly reasonable when we consider how sensitive these values are to the precise core size in such a high-index contrast waveguide and that we are approximating the dispersion of our polysilicon core material with that of single crystal silicon. Thus these results are further evidence of the high quality of the SCF core materials and our ability to precisely control the dimensions of the tapered profiles.

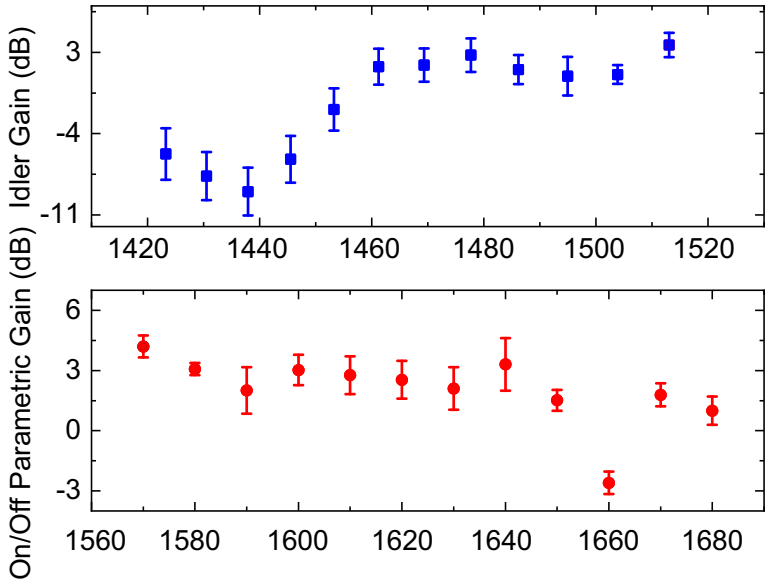

FIGURE 5.11: Idler conversion gain (a) and on/off parametric signal gain (b) as a function of wavelength for Fibre I. The error bars in the parametric gain data are derived from the uncertainty in the total propagation loss and the OSA noise.

FWM-based OPA were also conducted using Fibre I and Fibre II that have smaller core diameter than Fibre IV, but different fibre lengths (5 mm and 10 mm). Their properties were listed previously in Table 4.2. The experimental up is the same in Figure 5.4. The input peak power of the pump was kept at 17 W. The measured parametric signal and idler gains using these two fibres are seen in Figure 5.11 and Figure 5.12. It shows that using Fibre I, the maximum on/off signal gain of $\sim$ 4.2 dB is achieved at a wavelength of 1570 nm, with a corresponding idler conversion gain of $\sim$ 3.6 dB. Higher parametric gain was obtained using the Fibre II due to its longer waist lengths. The maximum parametric on/off gain for Fibre II is $\sim$7.2 dB with a corresponding idler conversion gain of $\sim$ 7 dB. This indicates that the fibre waist length of 10 mm helps to increase the parametric gain as well in FWM-based OPA. However, in both Fibre I and Fibre II, the side band is obvious throughout the whole tuning range. For Fibre I, the first side band starts at the signal wavelength of 1660 nm, and for fibre II, it begins at 1650 nm. These side bands correspond to the previous results for wavelength conversion, seen in Figure 4.9. In comparison to measured results of Fibre IV in Figure 5.8, it can be

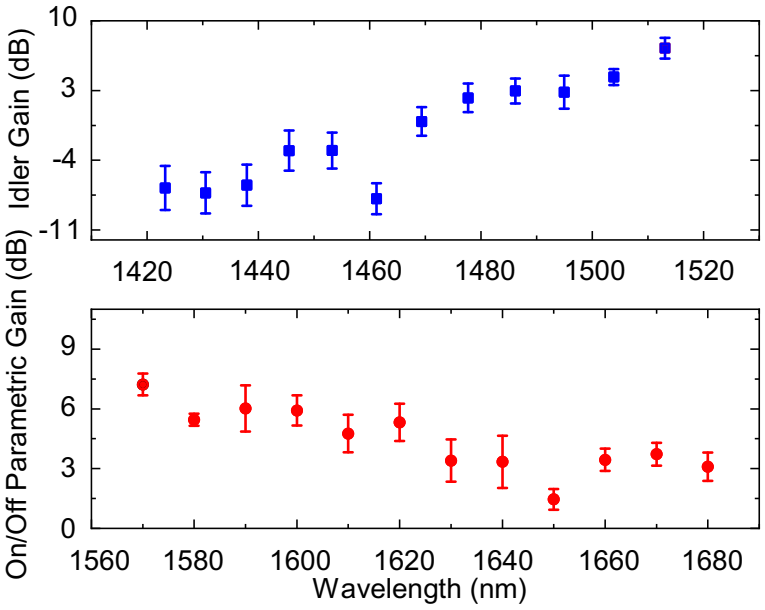

FIGURE 5.12: Idler conversion gain (a) and on/off parametric signal gain (b) as a function of wavelength for Fibre II. The error bars in the parametric gain data are derived from the uncertainty in the total propagation loss and the OSA noise.

assumed that Fibre IV has the ZDW closer to the pump wavelength than the other two fibres, Fibre I and Fibre II but with fairly similar maximum conversion efficiency. For further FWM-based applications, Fibre IV would also be the preferred choice as it exhibits a flatter tuning curve.

5.5 Conclusion

In this chapter, I carried out simulation work to investigate the influence of free carrier absorption and the role of the pulse pump parameters on FWM-based OPA. The results show that for repetition rates less than 100 MHz and femtosecond pulse widths, the influence of FCA on the parametric gain in telecom band was minimal, allowing for high net gain. Therefore, I chose a laser with a repetition rate of 40 MHz and pulse width of 670 fs as the pulsed pump to realize the OPA with high parametric gain in telecom band. Then, I fabricated a low-loss SCF that had been tapered down to have a submicron core diameter. Owing to the high coupling efficiency and negligible nonlinear absorption in this SCF, a signal gain as high as 9 dB was achieved with a moderate pump peak power of 17 W. To the best of our knowledge, this is the highest parametric gain reported in a crystalline silicon waveguide using sub-picosecond pump pulses at a telecommunications wavelength, resulting in the first demonstration of net off-waveguide gain in this regime. The experimentally measured conversion bandwidth of $\sim$ 260 nm covers the entire S-, C- and L- telecom bands and this could be extended further with careful design of our tapered structure. We expect that continued efforts to reduce the transmission losses will significantly improve the practicality of this platform, opening a

route for the development of compact and efficient all-fibre nonlinear signal processing systems.

Chapter 6

All-optical signal processing using silicon core fibres

6.1 Introduction

FWM-based wavelength conversion is the widely investigated nonlinear effects used in all-optical signal processing. As it has been discussed in previous chapters, submicron tapered SCFs have shown high conversion efficiencies and a wide tuning bandwidths for FWM-based wavelength conversion, due to their high nonlinearity and dispersion tailoring. Thus in this chapter, I explore the possibility to convert high-speed amplitude and phase modulated optical signals directly to the corresponding idler wavelengths based on the SCF platforms. After characterizing the SCF, the investigation starts with details of the signal modulation scheme, quadrature phase-shift keying (QPSK), which is a type of digital modulation that is used to convey data by changing the phase of the input carrier wave. Following this, the realization of all-optical signal processing of 20 Gb/s QPSK signals using a tapered SCF is described. The quality of the wavelength conversion is discussed, using the constellation diagrams and the bit error rate (BER) measurements. Finally, the fabrication method of the nano-spike coupler is introduced for realizing the all-optical signal processing using SCFs.

6.2 Characterisation of four-wave mixing

The tapered SCF Fibre IV with a core diameter of 915 nm is used here to investigate broad band wavelength conversion of QPSK signals, as this fibre offered the best performance in terms to CE and bandwidths. The profile and properties of Fibre IV were given previously in Table 5.2. Experiments to characterize the FWM performance were conducted, using the setup in Figure 4.5. The first goal is to investigate the optimum

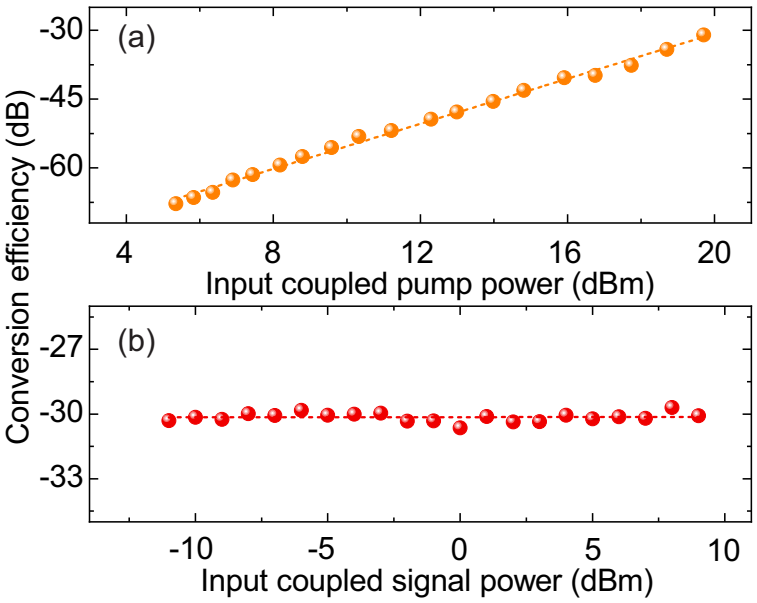

FIGURE 6.1: (a) Conversion efficiency as a function of coupled input pump power with an input signal power of 9 dBm. (b) Conversion efficiency as a function of coupled input signal power with an input coupled pump power of 20 dBm. The pump and signal wavelengths are 1550 nm and 1563 nm, respectively.

pump power and signal power to reach high conversion efficiency for the wavelength conversion. The conversion efficiency is plotted as a function of the input coupled pump power with the signal wavelength set at 1563 nm in Figure 6.1(a), with the idler wavelength of 1537 nm. It can be seen that the conversion efficiency increases linearly from -67.8 dB to -30.1 dB as the coupled signal power is raised from 5.4 dBm to 19.5 dBm. Figure 6.1(b) shows that the conversion efficiency remains constant when the signal power is varied from -11 dBm to 9 dBm for the input pump power of 20 dBm, which shows that nonlinear absorption at this level can be neglected. For the purpose of keeping the output idler power at its highest level for the signal processing system, the powers of the signal and pump were kept at 15 dBm and 19.5 dBm, respectively.

The second characterization conducted here is to determine the wavelength tuning for Fibre IV. The results are plotted in Figure 6.2, which shows that the 3 dB bandwidth is about 36 nm from the pump wavelength to the signal wavelength. Moreover, the signal-idler separation is up to 72 nm, covering from S-band to L-band. The wide tuning range and the high conversion efficiency of Fibre IV make it promising for use in multi-channel signal processing systems, thus wavelength division multiplexing (WDM).

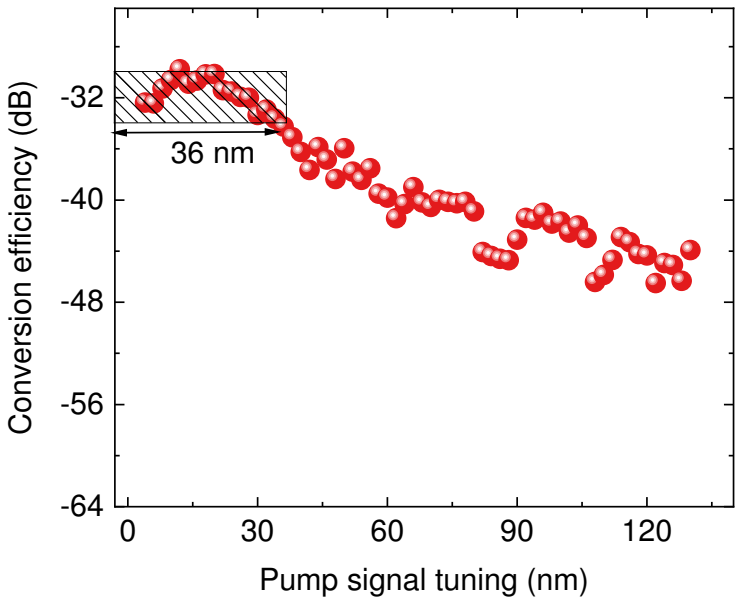

FIGURE 6.2: Measured conversion efficiencies for Fibre IV as the signal wavelength is tuned from 1555 to 1680 nm with a tuning step of 2 nm and a pump wavelength of 1550 nm.

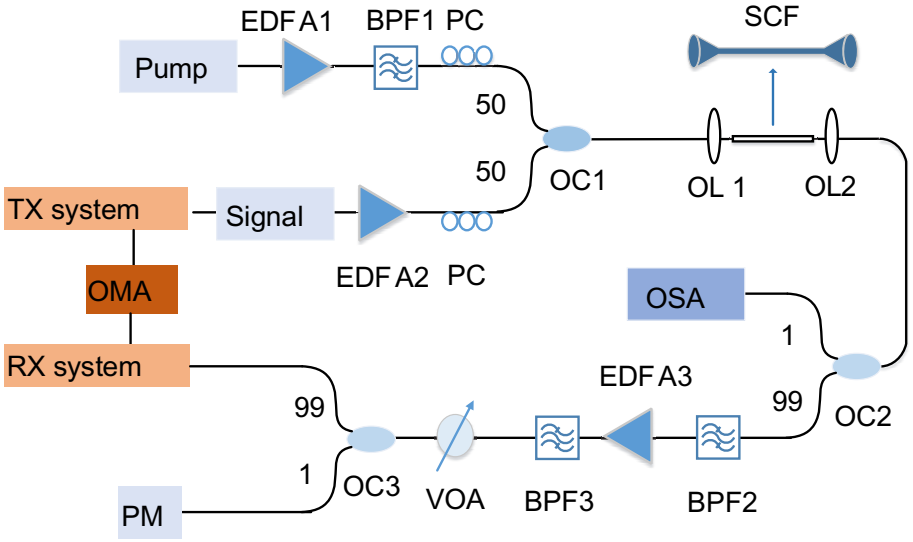

FIGURE 6.3: The experimental setup for signal processing of 20 Gb/s QPSK signals. OMA, optical modulation analyser; BPF, band pass filter; PC, polarization controller; OC, optical coupler; OL, objective lens; OSA, optical spectrum analyser; VOA, variable optical attenuator; PM, power meter.

6.3 Experimental setup for the 20 Gb/s QPSK signals processing

The experimental setup for the wavelength conversion of widely used QPSK signals is plotted in Figure 6.3. The pump wave originates from a laser emitting light at 1550 nm

which is amplified by a high-power erbium-doped fibre amplifier (EDFA) for the FWM process. A band pass filter (BPF1) is used to suppress the amplified spontaneous emission (ASE) noise. QPSK optical signals are generated at 10 Gbaud using an optical modulation analyser (OMA), which is connected to a tunable laser as the input seed signal wave. Due to the limitation of the OMA system, the signal wavelength can be tuned up to a maximum of 1580 nm. Therefore, the two channels we chose to investigate for signal processing are positioned at 1563 nm (C-band) and 1580 nm (L-band). The modulated QPSK is then used as the signal wave for the FWM process and gets amplified by a second EDFA. The two EDFAs used here are meant to increase the output power of the converted idlers from the SCF. Two polarization controllers (PCs) were employed to align the polarization states of the pump and signal waves to achieve the optimum conversion efficiency. The pump and the modulated signal are then combined together by a 50:50 fibre coupler and free space coupled into the SCF using a 40× objective lens (OL1). The output is coupled from the SCF by another objective lens2 (OL2, 63×) and sent for detection. A 99:1 tap coupler is used to accurately monitor the output power and spectrum by an OSA. The converted idler is selected using the BPF2 and sent to the EDFA3. The BPF3 is then used to suppress the ASE noise. The received power level is controlled by using a variable optical attenuator (VOA). Finally, the light is measured by a power meter and sent to a real time OMA that allows us to assess the performance of the wavelength conversion, both in terms of constellation diagrams and bit error ratio (BER) measurements.

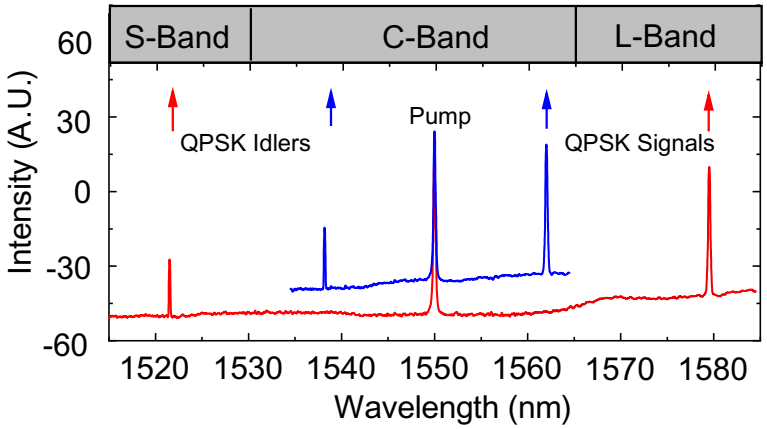

FIGURE 6.4: Measured spectra for wavelength conversion of 20 Gb/s QPSK data at two signal wavelengths of 1563 nm and 1580 nm , corresponding to the idler wavelengths of 1537 nm and 1521 nm, respectively. The blues curve of the FWM spectra is offset by 10 dB, for clarity.

Figure 6.4 shows the optical spectra measured at the output of tapered SCFs, for modulated signals at 1563 nm (C-band) and 1580 nm (L-band). The conversion efficiency with two signal wavelengths both achieved -30 dB. The back to back (B2B) signals were measured by taking the SCF out of the system. Both back to back and converted idler constellation diagrams are recorded by the OMA and plotted in Figure 6.5 for the modulated signals at 1563 nm (C-band) (a) and 1580 nm (L-band)(b). From the constellation

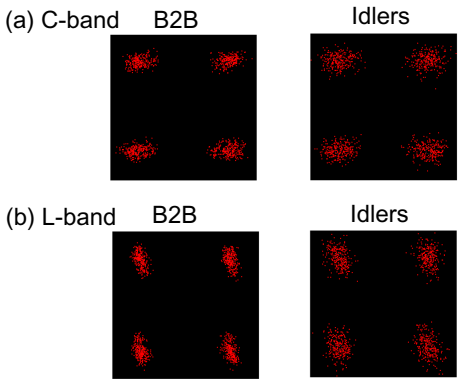

FIGURE 6.5: Measured constellation diagrams for wavelength conversion of 20 Gb/s QPSK data at C-band (a) and L-band (b) with the signal wavelengths of 1563 nm and 1580 nm, for the B2B signals and the converted idlers.

diagrams, it can be clearly seen that the modulated data has been successfully converted with moderate additional noise.

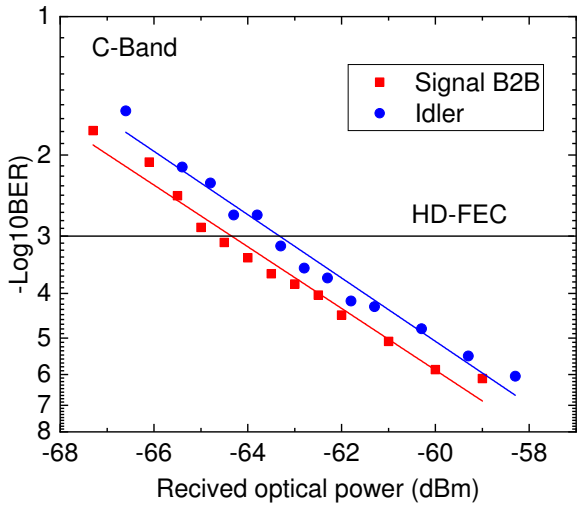

FIGURE 6.6: BER curves as a function of the calibrated received power for the 20 Gb/s QPSK data of the signals from C-band.

The quality of the signal processing system based on Fibre IV was also evaluated quantitatively by measuring the BER as a function of the calibrated received power, with the results shown in Figure 6.6 and Figure 6.7 for the different idlers. The received power is compromised mainly by the poor coupling efficiency to fibre based optical detector and secondly by the insertion losses of BPFs. However, the results still reveal that a successful conversion has been achieved with a power penalty of 1 dB at a BER of 3.8 $\times 10^{-3}$ (the hard-decision forward error correction (HD-FEC) limit) for the signals in C-band. Similar results can be seen for the signal wave length of 1580 nm at L-band shown in Figure 6.7, with the power penalty of 0.9 dB at a BER of 3.8 $\times 10^{-3}$.

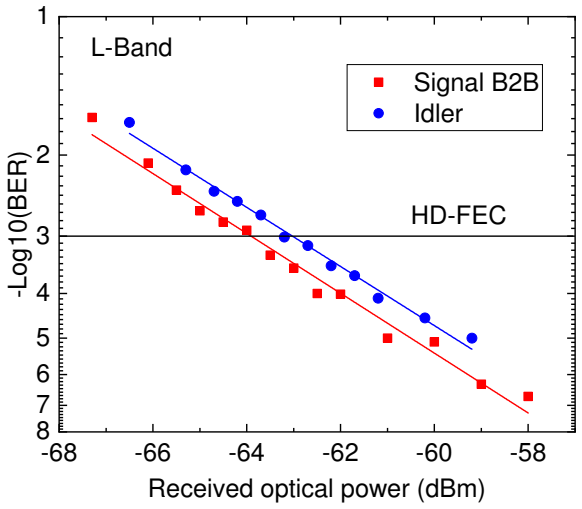

FIGURE 6.7: BER curves as a function of the calibrated received power for the 20 Gb/s QPSK data of the signals from L-band.

As the 3 dB bandwidth of Fibre IV is of 72 nm for the signal-idler separation, even wider wavelength conversion of 20Gb/s QPSK signals should be possible with similar low power penalty achieved. Also, because the power penalty is around 1 dB for all measured optical powers both in the C- and L- bands, this SCF shows potential for the wavelength conversion at even higher speeds, for example 32 Gbaud QPSK signals, and larger volume signal sequences, such as 16-Quadrature amplitude modulation (QAM) or 64-QAM.

6.4 Silicon core fibres with nano-spike coupler

Early in 2007, as reported in [57], full integration between the SCFs and SMF can be realized by incorporating nano-spike couplers onto the end facets of the SCFs. The nano-spike couplers can help to match the modes and also reduce the reflection at the interface between the SMF and SCF. Up to date, in 2019, a successful nano-spike coupler was demonstrated for all-fibre optical processing by Huang Meng *et.al* in our group [108]. The core size of the straight waist area for the SCF with nano-spike structure was 1.1 μm and the obtained FWM tuning range was 6 nm, which smaller than ours mainly is because of the ZDW is far from the pump wavelength. Nevertheless, wavelength conversion of 20Gb/s QPSK signals were achieved with the power penalty of 1 dB at a BER of 3.8 $\times 10^{-3}$. Significantly, my more recent work has shown the possibilities of wider tuning bandwidths using the SCF with smaller core sizes, which helps bring the telecom pump wavelengths closer to the ZDW. Thus, by combing these new designs with the nano-spike integration in [57], we can anticipate high efficiency, all-fibre based all-optical signal processing systems capable of supporting multiple channels with advanced

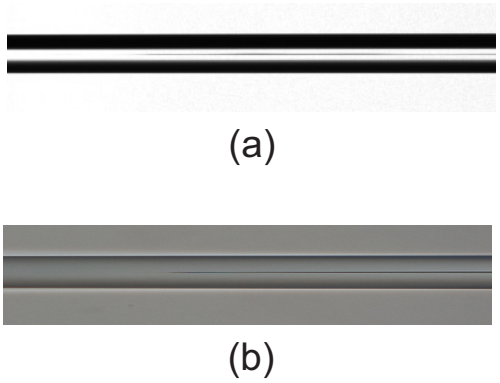

FIGURE 6.8: Transverse image of a successful nano-spike: (a) obtained via camera in Vytran, (b) obtained via high-resolution microscope.

signal formats. In this section, the fabrication method of the nano-spike couplers of SCFs with submicron core sizes are introduced, with some recipes given as references.

Generally, excessive heating will compress the silicon and create a discontinuous core that doesn't guide light, as seen in Figure 3.20(b). But if the overheating process is controlled well, and combined with tapering, the silicon core can be shaped into a nano-spike structure. There are two method of forming the nano-spike structure. One is tapering the fibre with a filament power that is just about to induce a break up of the continuous core. The recipe used to taper the nano-spike SCF via this method is described below.

Label	α (dB)	D_1 - D_2 (μm)	L_1-L_2-L_3 (mm)	P_s	δ	T_2
A	10	400-125	3-15-3	91W	0	34g
		125-26	3-15-3	60W	-10	10g

TABLE 6.1: Recipe of nano-spike SCFs (the first method).

Firstly, the double clad method was applied using the as-drawn fibre J895. δ of -10% was set at the second step with the filament start power P_s as 60 W, so that the filament power can decrease to 54 W when it moves to the waist region for tapering. And the tension used for nano-spike SCF is lower that that for small core tapered SCFs. By applying a slightly higher temperature, the nano-spike will form in the middle of the waist area. Using the parameters given in Table 6.1, a nano-spike SCF was formed as seen in Figure 6.8. However, this method require precise temperature controlling and the position of where the nano-spike is formed in the SCF couldn't be exactly controlled.

The second method of forming the nano-spike coupler is introduced. During the tapering process, a void gap will always appear at the beginning of the tapered region, due to

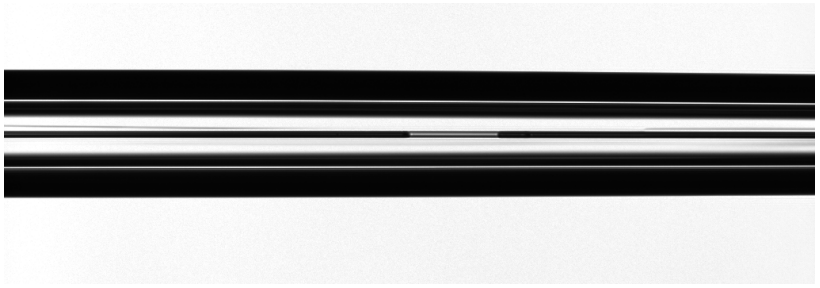

FIGURE 6.9: The void gap in the SCF.

melting and relaxing of the strained as-drawn silicon core, which is seen in Figure 6.9. By tapering the area that includes the void gap, the nano-spikes can subsequently form.

The detailed scheme is pictured in Figure 6.10. At the first step, the as-drawn SCF is heated for 2 mm long, seen in Figure 6.10(a). The void gap will appear in the beginning of the heated region. The second step is to taper the fibre including the void region. After moving the void gap region to the right of the originally heated centre by 1.35 mm, the tapering process can be started as shown in Figure 6.10(b). Here, the optimised recipe in the previous sections of tapering the small core fibres can be applied. In the end, the nano-spike will be fabricated successfully in the tapered region as seen in Figure 6.10(c).

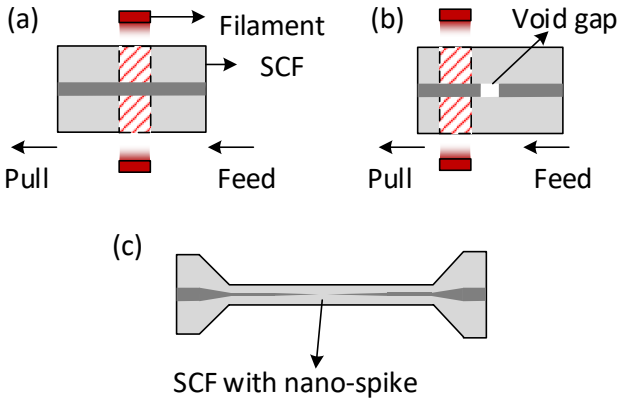

FIGURE 6.10: The schemes of the fabricating the nano-spike in SCF.

After fabricating the nano-spike in the SCF, the next step is to integrate with the SMF. At first, SMF-28 is tapered down to have the same outer diameter as the SCF cladding diameter of the nano-spike area. This is to match the cladding dimensions between the two fibres for better mechanical integration and matching of the modes. Next, as seen in Figure 6.11(a), carefully cleave the SCF part with nano-spike at the facet. The way we cleave is using a sharp blade and taped it next to the filament of Vytran. As filament can be controlled to move up and down via the software of Vytran, after firmly attaching the

blade to the filament, the blade can be controlled precisely together with the filament. When the tension is applied along the fibre, and the blade was raised up about to touch the fibre, a quick cleave could give us a clean end facet for splicing at the next step.

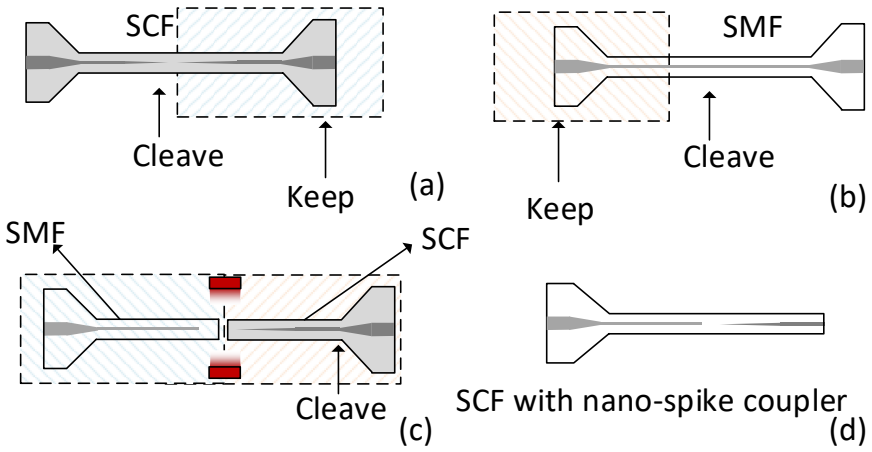

FIGURE 6.11: The integration of the nano-spiked SCF with the tapered SMF.

Normally, the formed nano-spike exhibit better quality on the right side of the SCF, hence, we mainly keep the right part of the SCF with the nano spike. Next, as seen in Figure 6.11(b), the tapered SMF is cleaved using the same method and half of it is kept. In the third step, the SMF and the SCF with nano-spike coupler are spliced together. The third cleave is needed to cleave of the up-taper region of the SCF, as depicted in Figure 6.11(c). Finally, the SCF with the nano-spike coupler that is integrated with SMF is formed as shown in Figure 6.11(d).

Step	D_1 - D_2 **(μm)**	L_1-L_2-L_3 **(mm)**	P_s	T_2
Step 1	400-125	3-15-3	93W	45g
Step 2	125-125	1-2-1	47W	0g
Step 3	125-30	3-15-3	51W	30g
Step 4*	30-30	—	33W	–

TABLE 6.2: Recipes of nano-spike SCFs (the second method).

The recipes used for the method above are given in Table 6.2. In order to fabricate nano-spike onto the ends of sub-micron core silicon fibres, the optimised double-clad method was also applied. Step 1 shows the fibre gets tapered from 400 μm down to 125 μm with the maximum tension T_2 of 45 g. The second step heats the fibre in the middle at the power of 47 W with the tension dropping down from 13 g to 0 g. Next at the third step, the fibre gets tapered down to 30 μm using the filament power as 51 W

with T_2 of 30 g.To note, the filament power for forming the void gap at the second step is lower than that for tapering. In the fourth step, the splice between the nano-spike SCF and the tapered SMF was performed with P_s as 33 W. EW32

Finally, a SCF with the nano-spike coupler was fabricated. Its core size of the straight waist area was estimated to be 0.9 μm and the length of the straight waist area was about 2 mm. The total length of the device including the SMF area was about 0.5 m. The nano-spike coupler was then characterised using the similar setup as shown in Figure 3.11. Differently, the pump laser was connected directly to the SMF using a the fibre adaptor. The output coupling was still the free space coupling, with the 60× lens applied. The output beam profile was monitored using a CCD camera that was connected to a monitor screen.

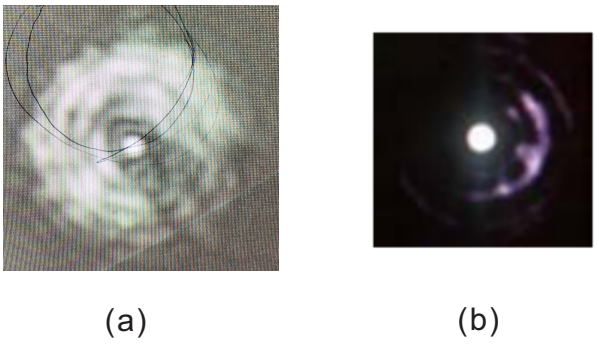

FIGURE 6.12: The output spot image of the nano-spike SCF: (a) with the submicron core size, (b) with 1.1 μm core size.

The output spot profile on the monitor is then seen in Figure 6.12(a) after spatial filtering. Comparing to the output profile, as displayed in Figure 6.12(b) obtained by Ren et.a. [57], the output mode of our nano-spike coupler was mostly scattered from the silicon core to the silica cladding. This may be resulted from the poor integration between the SCF and the SMF. The total losses for the device was measured to about 13 dB, with the input pump power of 10 mW at the wavelength of 1550 nm. Unfortunately, no significant nonlinear process was observed using this nano-spike coupler when a pulsed pump (670 fs, 40 MHz) was applied at a higher input power of 20 mW. The reasons are still under investigation. Possible reasons can be attributed to the poor quality of the formed nano-spike and the integration between the SCF and the SMF. These factors will reduce the coupled-in pump intensity into the silicon core of the SCF, thus limiting the conversion efficiency greatly. The splicing between the SCF and the SMF also needs to be considered more carefully due to the optical mode mismatching, especially when the submicron core was used. Further improvements can be mainly optimising the parameters as shown in Table 6.2, but also reducing the complexity of the nano-spike couplers.

6.5 Conclusion

In this chapter, we characterized the FWM-based wavelength conversion for Fibre IV with a core diameter of 915 nm and a waist length of 5 mm. It has a tuning range of 36 nm. Then, we chose two signal wavelengths 1563 nm and 1580 nm for conducting the signal processing experiments. The 20Gb/s QPSK signals at both the C-and L-band have been successfully converted, with conversion efficiencies as high as -30 dB, using the SCF. The power penalties at a BER of 3.8 $\times 10^{-3}$ are less than 1 dB. Finally, the fabrication method to achieve SCFs with nano-spike couplers is explained. By combing the small core SCFs designs with the nano-spike couplers, we anticipate that successful high speed wavelength conversion of more advanced signals could be demonstrated in our SCFs with improved coupling and conversion efficiency. Moreover, this work paves the road for all-fibre optical signal processing systems when the SCFs are connected to conventional fibres via nano-spike couplers, indicating the potential for them to find use in practical telecom applications.

Chapter 7

Conclusions and future work

7.1 Conclusions

This thesis is focused on FWM-based nonlinear applications using tapered silicon core fibres.

The first main achievement is based on optimization of the tapering process, such as the two-step tapering and the double-clad tapering methods. Using these methods, several sub-micron core sized silicon core fibres were tapered successfully with linear losses less than 3 dB/cm, with the improved crystallinity of the poly-Si core. The longest tapered SCF has the waist length of 15 mm to date.

The second is by using these tapered sub-micron SCFs with different waist lengths, FWM-based wavelength conversion using a continuous wave pumped at 1550 nm was firstly demonstrated, covering the telecom bands, from S- to L- band. The maximum conversion efficiency was obtained as high as -30 dB, which is comparable to the value obtained on the sub-micron poly-Si planar waveguides.

The third key demonstration was to use a tapered SCF with its ZDW designed close to the pump wavelength to achieve FWM-based optical parametric amplification. By using a carefully chosen pump, the OPA could reach as high as 9 dB. This was the first demonstration of the optical parametric amplification in a poly-Si waveguides and represents the highest gain in any crystalline silicon waveguide using a pulsed pump at telecom wavelengths to date. Moreover, thanks to the favourable dispersion, broadband wavelength conversion could also be realized, crossing the S- to L- band.

Lastly, the 20 Gb/s QPSK signals at both the C- band and L- band have been successfully converted using a tapered SCF. The power penalties at a BER of 3.8 $\times 10^{-3}$ are less than 1 dB. This was the broadest FWM-based wavelength conversion realized using the SCF platform.

With further optimization of the crystallinity of the fibre core to enhance the FWM conversion efficiency, we anticipate successful high speed wavelength conversion of more advanced signals could be demonstrated in our SCFs. By connecting the SCFs to conventional fibres via nano-spike couplers, this work could lead to all-fibre optical signal processing systems suitable for use in practical telecom applications.

7.2 Future work

Even though the submicron core SCFs have been successfully applied to FWM-based signal processing systems, there are more areas to investigate for the application of SCFs nonlinear systems. The proposals for this work to improve are listed as below.

1. By further improving the tapering process, the linear losses for the tapered submicron core fibres could be reduced down to the scale of SOI wire as 0.1 dB/cm, with core sizes smaller than 1 μm. Such a low loss, small core SCF will help to realize higher parametric FWM gain at telecom bands.

2. The FWM-based wavelength conversion can be extended further by tuning the pump wavelength from 1.5 μm to 2.0 μm using larger SCF with the core diameter around 1.2 μm. As the TPA of silicon at wavelengths greater than 2.2 μm is negligible, higher conversion efficiency and wider tuning range can be expected.

3. One key benefit of the silicon core fibres is their potential compatibility with silica fibre infrastructures. Even though nanospike coupling has been realised within a silicon core fibre that can be directly spliced to a SMF, more improvements could be made to these structures so that they could be used for the nonlinear processing work.

4. Although a lot of work has been conducted on Raman amplification in silicon planar waveguides in the telecoms band, nothing has yet been demonstrated in the mid-IR. Our large core silicon fibres offer low linear and nonlinear losses in this region and so the investigation of the use of SCFs for the construction of mid-IR Raman amplifiers and lasers would be another fruitful avenue of research.

List of publications

Journal

1. Meng Huang, Shiyu Sun, **Dong Wu**, Haonan Ren, Li Shen, Hawkins W. Thomas, John Ballato, Ursula J. Gibson and Anna C. Peacock. Continuous-wave Raman amplification in silicon core fibers pumped in the telecom band. APL Photonics, 6(9), 096105 (2021).

2. **Dong Wu**, Li Shen, Haonan Ren, Joseph Campling, Hawkins W. Thomas, John Ballato, Ursula J. Gibson and Anna C. Peacock. Net optical parametric gain in a submicron silicon core fiber pumped in the telecom band. APL Photonics, 4(8), 086102 (2019).

3. **Dong Wu**, Li Shen, Haonan Ren, Meng Huang, Cosimo Lacava, Joesph Campling, Hawkins W. Thomas, John Ballato, Ursula J. Gibson and Anna C. Peacock. Four-wave mixing-based wavelength conversion and parametric amplification in submicron silicon core fibers. IEEE Journal of Selected Topics in Quantum Electronics, 27(2), 43001111 (2020).

4. Li Shen, Haonan Ren, Meng Huang, **Dong Wu** and Anna C. Peacock. A review of nonlinear applications in silicon optical fibers from telecom wavelengths into the mid-infrared spectral region. Optics Communications, 463, 125437 (2020).

5. Haonan Ren, Li Shen, **Dong Wu** , Ozan Aktaş , Hawkins W. Thomas, John Ballato, Ursula J. Gibson and Anna C. Peacock. Nonlinear optical properties of polycrystalline silicon core fibers from telecom wavelengths into the mid-infrared spectral region. Optical Materials Express, 9(3), 1271-1279 (2019).

6. Shiyu Sun, Meng Huang, **Dong Wu**, Haonan Ren, Li Shen, Hawkins W. Thomas, John Ballato, Ursula J. Gibson and Anna C. Peacock. Raman enhanced four-wave mixing in silicon core fibers. Optics Letters, 47(7), 1626-1629 (2022).

Conference Papers

1. **Dong Wu**, Li Shen, Cosimo Lacava, Periklis Petropoulos, Hawkins W. Thomas, John Ballato, Ursula J. Gibson and Anna C. Peacock. Tapered submicron silicon core fiber for broadband wavelength conversion. Conference on Lasers and Electro-Optics, Virtual. 09 - 14 May 2020.

2. **Dong Wu**, Li Shen, Haonan Ren, Hawkins W. Thomas, John Ballato, Ursula J. Gibson and Anna C. Peacock. Broad-band optical parametric amplification in a tapered silicon core fiber pumped in the telecom band. Conference on Lasers and Electro-Optics Europe and European Quantum Electronics Conference, International Congress Centre, Germany. 22 - 26 Jun 2019.

3. Meng Huang, Haonan Ren, Li Shen, **Dong Wu**, Shiyu Sun, Hawkins W. Thomas, John Ballato, Ursula J. Gibson and Anna C. Peacock. Stimulated Raman scattering in a tapered submicron silicon core fiber. Conference on Lasers and Electro-Optics, Virtual. 09 - 14 May 2021.

4. Shiyu Sun, Meng Huang, **Dong Wu**, Li Shen, Haonan Ren, Hawkins W. Thomas, John Ballato, Ursula J. Gibson, Goran Z. Mashanovich and Anna C. Peacock. Raman enhanced four-wave mixing in silicon core Fibers, IEEE Photonics Conference, 18 October, 2021.

Bibliography

[1] G. T. K. Reed, *Silicon Photonics - Introduction*, November (John Wiley & Sons Ltd, 2004).

[2] J. Leuthold, C. Koos, and W. Freude, "Nonlinear silicon photonics," Nature Photonics **4**, 535–544 (2010).

[3] S. V. Smirnov, J. D. Ania-Castanon, T. J. Ellingham, S. M. Kobtsev, S. Kukarin, and S. K. Turitsyn, "Optical spectral broadening and supercontinuum generation in telecom applications," Optical Fiber Technology **12**, 122–147 (2006).

[4] R. Salem, A. C. Turner, A. L. Gaeta, M. A. Foster, D. F. Geraghty, and M. Lipson, "All-optical regeneration on a silicon chip," Optics Express **15**, 7802–7809 (2007).

[5] T. K. Liang, L. R. Nunes, T. Sakamoto, G. R. A. Priem, M. Tsuchiya, H. K. Tsang, T. Kawanishi, R. Baets, P. Dumon, D. Van Thourhout, and K. Sasagawa, "Ultrafast all-optical switching by cross-absorption modulation in silicon wire waveguides," Optics Express **13**, 7298–7303 (2005).

[6] H. Fukuda, K. Yamada, T. Shoji, M. Takahashi, T. Tsuchizawa, T. Watanabe, J.-i. Takahashi, and S.-i. Itabashi, "Four-wave mixing in silicon wire waveguides," Optics Express **13**, 4629–4637 (2005).

[7] L. Liu, R. Kumar, K. Huybrechts, T. Spuesens, G. Roelkens, E. J. Geluk, T. De Vries, P. Regreny, D. Van Thourhout, R. Baets, and G. Morthier, "An ultrasmall, low-power, all-optical flip-flop memory on a silicon chip," Nature Photonics **4**, 182–187 (2010).

[8] B. Kuyken, X. Liu, R. M. Osgood Jr., R. Baets, G. Roelkens, and W. M. J. Green, "Mid-infrared to telecom-band supercontinuum generation in highly nonlinear silicon-on-insulator wire waveguides," Optics Express **19**, 20172–20181 (2011).

[9] M. A. Foster, A. C. Turner, J. E. Sharping, B. S. Schmidt, M. Lipson, and A. L. Gaeta, "Broad-band optical parametric gain on a silicon photonic chip," Nature **441**, 960–963 (2006).

[10] A. C. Turner-Foster, M. A. Foster, R. Salem, A. L. Gaeta, and M. Lipson, "Frequency conversion over two-thirds of an octave in silicon nanowaveguides," Optics Express **18**, 1904–1908 (2010).

[11] X. Liu, B. Kuyken, G. Roelkens, R. Baets, R. M. Osgood, W. M. J. Green, R. M. O. Jr, and W. M. J. Green, "Bridging the mid-infrared-to-telecom gap with silicon nanophotonic spectral translation," Nature Photonics **6**, 667–671 (2012).

[12] K. Guo, L. Lin, J. B. Christensen, E. N. Christensen, X. Shi, Y. Ding, K. Rottwitt, and H. Ou, "Broadband wavelength conversion in a silicon vertical-dual-slot waveguide," Optics Express **25**, 32964–32971 (2017).

[13] R. Salem, M. A. Foster, A. C. Turner, D. F. Geraghty, M. Lipson, and A. L. Gaeta, "Signal regeneration using low-power four-wave mixing on silicon chip," Nature Photonics **2**, 35–38 (2008).

[14] M. A. Foster, A. C. Turner, M. Lipson, L. Alexander, and A. L. Gaeta, "Nonlinear optics in photonic nanowires," Optics Express **16**, 1300–1320 (2008).

[15] K. I. Harada, H. Takesue, H. Fukuda, T. Tsuchizawa, T. Watanabe, K. Yamada, Y. Tokura, and S. I. Itabashi, "Frequency and polarization characteristics of correlated photon-pair generation using a silicon wire waveguide," IEEE Journal on Selected Topics in Quantum Electronics **16**, 325–331 (2010).

[16] D. Bonneau, J. W. Silverstone, and M. G. Thompson, "Silicon quantum photonics," Topics in Applied Physics **122**, 41–82 (2016).

[17] D. Dimitropoulos, V. Raghunathan, Y. Han, R. Claps, and B. Jalali, "Observation of stimulated Raman amplification in silicon waveguides," Optics Express **11**, 1731–1739 (2010).

[18] O. Boyraz, B. Jalali, B. Jalali, S. Yegnanarayanan, T. Yoon, T. Yoshimoto, I. Rendina, and F. Coppinger, "Demonstration of a silicon Raman laser," Optics Express **12**, 5269–5273 (2004).

[19] H. Rong, S. Xu, Y.-H. H. Kuo, V. Sih, O. Cohen, O. Raday, and M. Paniccia, "Low-threshold continuous-wave Raman silicon laser," Nature Photonics **1**, 232–237 (2007).

[20] I.-w. Hsieh, X. Chen, X. Liu, J. I. Dadap, N. C. Panoiu, C.-y. Chou, F. Xia, W. M. Green, Y. A. Vlasov, and R. M. Osgood, "Supercontinuum generation in silicon photonic wires," Optics Express **15**, 15242–15249 (2007).

[21] S. D. Jackson, Y. Yu, C. Grillet, D. D. Hudson, S. Madden, A. Casas-Bedoya, P. Atanackovic, S. Palomba, B. Luther-Davies, A. Read, B. J. Eggleton, N. Singh, D. J. Moss, and S. G. Duvall, "Midinfrared supercontinuum generation from 2 to 6 μm in a silicon nanowire," Optica **2**, 797–802 (2015).

[22] N. Singh, M. Xin, D. Vermeulen, K. Shtyrkova, N. Li, P. T. Callahan, E. S. Magden, A. Ruocco, N. Fahrenkopf, C. Baiocco, B. P. Kuo, S. Radic, E. Ippen, F. X. Kärtner, and M. R. Watts, "Octave-spanning coherent supercontinuum generation in silicon on insulator from 1.06 μm to beyond 2.4 μm," Light: Science and Applications **7**, 171311–171318 (2018).

[23] J. Hansryd, P. Andrekson, M. Westlund, Jie Li, and P. O. Hedekvist, "Fiber-based optical parametric amplifiers and their applications," IEEE Journal of Selected Topics in Quantum Electronics **8**, 506–520 (2002).

[24] M. A. Foster, A. C. Turner, R. Salem, M. Lipson, and A. L. Gaeta, "Broad-band continuous-wave parametric wavelength conversion in silicon nanowaveguides," Optics Express **15**, 12949–12958 (2007).

[25] Z. Fang and C. Z. Zhao, "Recent progress in silicon photonics: a review," ISRN Opt. **2012**, 1–27 (2012).

[26] A. Gajda, A. Peczek, C. Schubert, E. Liebig, I. Sackey, K. Petermann, and L. Zimmermann, "1.024 Tb/s wavelength conversion in a silicon waveguide with reverse-biased p-i-n junction," Optics Express **25**, 21229–21240 (2017).

[27] H. Rong, Y.-H. Kuo, A. Liu, M. Paniccia, and O. Cohen, "High efficiency wavelength conversion of 10 Gb/s data in silicon waveguides," Optics Express **14**, 1182–1188 (2006).

[28] K. J. Ooi, D. K. Ng, T. Wang, A. K. Chee, S. K. Ng, Q. Wang, L. K. Ang, A. M. Agarwal, L. C. Kimerling, and D. T. Tan, "Pushing the limits of CMOS optical parametric amplifiers wixth USRN:Si7N3 above the two-photon absorption edge," Nature Communications **8**, 1–10 (2017).

[29] H. Hu, H. Ji, M. Galili, M. Pu, C. Peucheret, H. C. H. Mulvad, K. Yvind, J. M. Hvam, P. Jeppesen, and L. K. Oxenløwe, "Ultra-high-speed wavelength conversion in a silicon photonic chip," Optics Express **19**, 19886–19894 (2011).

[30] J. Wang and Y. Long, "On-chip silicon photonic signaling and processing: a review," Science Bulletin **63**, 1267–1310 (2018).

[31] M. Chagnon, M. Spasojevic, R. Adams, J. Li, D. V. Plant, and L. R. Chen, "Wavelength multicasting at 22-GBaud 16-QAM in a silicon nanowire using four-wave mixing," IEEE Photonics Technology Letters **27**, 860–863 (2015).

[32] R. Adams, M. Spasojevic, M. Chagnon, M. Malekiha, J. Li, D. V. Plant, and L. R. Chen, "Wavelength conversion of 28 GBaud 16-QAM signals based on four-wave mixing in a silicon nanowire," Optics Express **22**, 4083–4090 (2014).

[33] C. Li, C. Gui, J. Wang, Q. Yang, S. Yu, and X. Xiao, "On-chip all-optical wavelength conversion of multicarrier, multilevel modulation (OFDM m-QAM) signals using a silicon waveguide," Optics Letters **39**, 4583–4586 (2014).

[34] C. Lacava, M. A. Ettabib, I. Cristiani, J. M. Fedeli, D. J. Richardson, and P. Petropoulos, "Ultra-compact amorphous silicon waveguide for wavelength conversion," IEEE Photonics Technology Letters **28**, 410–413 (2016).

[35] Y. Long, J. Liu, X. Hu, A. Wang, L. Zhou, K. Zou, Y. Zhu, F. Zhang, and J. Wang, "All-optical multi-channel wavelength conversion of Nyquist 16 QAM signal using a silicon waveguide," Optics Letters **40**, 5475–5478 (2015).

[36] A. Bogris, A. Kapsalis, D. Syvridis, F. Parmigiani, K. Hammani, L. Jones, M. Brun, M. A. Ettabib, P. Petropoulos, P. Labeye, and S. Nicoletti, "FWM-based wavelength conversion of 40 Gbaud PSK signals in a silicon germanium waveguide," Optics Express **21**, 16683–16689 (2013).

[37] A. C. Peacock, U. J. Gibson, and J. Ballato, "Silicon optical fibres–past, present, and future," Advances in Physics: X **1**, 114–127 (2016).

[38] K. Shimamura, S. Uda, T. Yamada, S. Sakaguchi, and T. Fukuda, "Silicon single crystal fiber growth by micro pulling down method," Japanese Journal of Applied Physics **35**, 793–795 (1996).

[39] P. J. A. Sazio, A. Amezcua-Correa, C. E. Finlayson, J. R. Hayes, T. J. Scheidemantel, N. F. Baril, B. R. Jackson, D.-J. Won, F. Zhang, E. R. Margine, V. Gopalan, V. H. Crespi, and J. V. Badding, "Microstructured optical fibers as high-pressure microfluidic reactors," Science **311**, 1583–1586 (2006).

[40] C. E. Finlayson, A. Amezcua-Correa, P. J. Sazio, N. F. Baril, and J. V. Badding, "Electrical and Raman characterization of silicon and germanium-filled microstructured optical fibers," Applied Physics Letters **90**, 1321101–1321104 (2007).

[41] L. Lagonigro, N. Healy, J. R. Sparks, N. F. Baril, P. J. A. Sazio, J. V. Badding, and A. C. Peacock, "Low loss silicon fibers for photonics applications," Applied Physics Letters **96**, 1–3 (2010).

[42] N. F. Baril, R. He, T. D. Day, J. R. Sparks, B. Keshavarzi, M. Krishnamurthi, A. Borhan, V. Gopalan, A. C. Peacock, N. Healy, P. J. A. Sazio, and J. V. Badding, "Confined high-pressure chemical deposition of hydrogenated amorphous silicon," Journal of the American Chemical Society **134**, 19–22 (2012).

[43] P. Mehta, N. Healy, N. F. Baril, P. J. A. Sazio, J. V. Badding, and A. C. Peacock, "Nonlinear transmission properties of hydrogenated amorphous silicon core optical fibers," Optics Express **18**, 16826–16831 (2010).

[44] J. Ballato, T. Hawkins, P. Foy, R. Stolen, B. Kokuoz, M. Ellison, C. McMillen, J. Reppert, A. M. Rao, M. Daw, S. R. Sharma, R. Shori, O. Stafsudd, R. R. Rice, and D. R. Powers, "Silicon optical fiber," Optics Express **16**, 18675–18683 (2008).

[45] A. C. Peacock, J. Campling, A. F. J. Runge, H. Ren, L. Shen, O. Aktas, P. Horak, N. Healy, U. J. Gibson, and J. Ballato, "Wavelength conversion and supercontinuum generation in silicon optical fibers," IEEE Journal of Selected Topics in Quantum Electronics **24**, 5–6 (2018).

[46] B. L. Scott, K. Wang, and G. Pickrell, "Fabrication of n-type silicon optical fibers," IEEE Photonics Technology Letters **21**, 1798–1800 (2009).

[47] N. Healy, L. Lagonigro, J. R. Sparks, S. Boden, P. J. A. Sazio, J. V. Badding, and A. C. Peacock, "Polycrystalline silicon optical fibers with atomically smooth surfaces." Optics letters **36**, 2480–2482 (2011).

[48] S. Morris, C. McMillen, T. Hawkins, P. Foy, R. Stolen, J. Ballato, and R. Rice, "The influence of core geometry on the crystallography of silicon optical fiber," Journal of Crystal Growth **352**, 53–58 (2012).

[49] S. Morris, T. Hawkins, P. Foy, J. Hudson, L. Zhu, R. Stolen, R. Rice, and J. Ballato, "On loss in silicon core optical fibers," Optical Materials Express **2**, 1511–1519 (2012).

[50] E. F. Nordstrand, A. N. Dibbs, A. J. Eraker, and U. J. Gibson, "Alkaline oxide interface modifiers for silicon fiber production," Optical Materials Express **3**, 651–657 (2013).

[51] A. Gumennik, L. Wei, G. Lestoquoy, A. M. Stolyarov, X. Jia, P. H. Rekemeyer, M. J. Smith, X. Liang, B. J. B. Grena, S. G. Johnson, S. Gradečak, A. F. Abouraddy, J. D. Joannopoulos, and Y. Fink, "Silicon-in-silica spheres via axial thermal gradient in-fibre capillary instabilities," Nature Communications **4**, 1–8 (2013).

[52] N. Healy, J. R. Sparks, P. J. Sazio, J. V. Badding, and A. C. Peacock, "Tapered silicon optical fibers," Optics Express **18**, 7596–7601 (2010).

[53] F. H. Suhailin, L. Shen, N. Healy, L. Xiao, M. Jones, T. Hawkins, J. Ballato, U. J. Gibson, and A. C. Peacock, "Tapered polysilicon core fibers for nonlinear photonics," Optics Letters **41**, 1360–1363 (2016).

[54] Y. Franz, A. F. J. Runge, H. Ren, N. Healy, K. Ignatyev, M. Jones, T. Hawkins, J. Ballato, U. J. Gibson, and A. C. Peacock, "Material properties of tapered crystalline silicon core fibers," Optical Materials Express **7**, 2055–2061 (2017).

[55] H. Ren, L. Shen, D. Wu, O. Aktas, T. Hawkins, J. Ballato, U. J. Gibson, and A. C. Peacock, "Nonlinear optical properties of polycrystalline silicon core fibers from telecom wavelengths into the mid-infrared spectral region," Optical Materials Express **9**, 1271–1279 (2019).

[56] S. Zhang, Z. Zhao, N. Chen, F. Pang, Z. Chen, Y. Liu, and T. Wang, "Temperature characteristics of silicon core optical fiber Fabry–Perot interferometer," Optics Letters **40**, 1362–1365 (2015).

[57] H. Ren, O. Aktas, Y. Franz, A. F. J. Runge, T. Hawkins, J. Ballato, U. J. Gibson, A. C. Peacock, and T. Hawkins, "Tapered silicon core fibers with nano-spikes for optical coupling via spliced silica fibers," Optics Express **25**, 24157–24163 (2017).

[58] M. Fokine, A. Theodosiou, S. Song, T. Hawkins, J. Ballato, K. Kalli, and U. J. Gibson, "Laser structuring, stress modification and Bragg grating inscription in silicon-core glass fibers," Optical Materials Express **7**, 1589–1597 (2017).

[59] F. A. Martinsen, J. Ballato, T. Hawkins, and U. J. Gibson, "Bulk fabrication and properties of solar grade silicon microwires," APL Materials **2**, 1161081–1161087 (2014).

[60] F. A. Martinsen, B. K. Smeltzer, J. Ballato, T. Hawkins, M. Jones, and U. J. Gibson, "Light trapping in horizontally aligned silicon microwire solar cells," Optics Express **23**, A1463–A1471 (2015).

[61] F. A. Martinsen, B. K. Smeltzer, M. Nord, T. Hawkins, J. Ballato, and U. J. Gibson, "Silicon-core glass fibres as microwire radial-junction solar cells," Scientific Reports **4**, 1–7 (2014).

[62] Y. P. Huang and L. A. Wang, "In-line silicon Schottky photodetectors on silicon cored fibers working in 1550nm wavelength regimes," Applied Physics Letters **106**, 1–5 (2015).

[63] D. J. Won, M. O. Ramirez, H. Kang, V. Gopalan, N. F. Baril, J. Calkins, J. V. Badding, and P. J. Sazio, "All-optical modulation of laser light in amorphous silicon-filled microstructured optical fibers," Applied Physics Letters **91**, 1611121–161113 (2007).

[64] P. Mehta, N. Healy, T. D. Day, J. R. Sparks, P. J. A. Sazio, J. V. Badding, and A. C. Peacock, "All-optical modulation using two-photon absorption in silicon core optical fibers," Opt. Express **19**, 19078–19083 (2011).

[65] P. Mehta, N. Healy, T. D. Day, J. V. Badding, and A. C. Peacock, "Ultrafast wavelength conversion via cross-phase modulation in hydrogenated amorphous silicon optical fibers," Optics Express **20**, 26110–26116 (2012).

[66] F. H. Suhailin, N. Healy, Y. Franz, M. Sumetsky, J. Ballato, A. N. Dibbs, U. J. Gibson, and A. C. Peacock, "Kerr nonlinear switching in a hybrid silica-silicon microspherical resonator," Optics Express **23**, 17263–17268 (2015).

[67] A. Peacock and N. Healy, "Parabolic pulse generation in tapered silicon fibers," Optics Letters **35**, 1780–1782 (2010).

[68] A. C. Peacock, "Soliton propagation in tapered silicon core fibers," Optics Letters **35**, 3697–3699 (2010).

[69] A. C. Peacock, "Mid-IR soliton compression in silicon optical fibers and fiber tapers," Optics Letters **37**, 818–820 (2012).

[70] L. Shen, N. Healy, L. Xu, H. Y. Cheng, T. D. Day, J. H. V. Price, J. V. Badding, and A. C. Peacock, "Four-wave mixing and octave-spanning supercontinuum generation in a small core hydrogenated amorphous silicon fiber pumped in the mid-infrared," Optics Letters **39**, 5721–5724 (2014).

[71] K. Okamoto, *Fundamentals of Optical Waveguides (Google eBook)* (Elsevier Inc. All, 2010), 2nd ed.

[72] G. P. Agrawal, *Nonlinear Fibre Optics* (Academic Press, 2000).

[73] B. J. Frey, D. B. Leviton, and T. J. Madison, "Temperature dependent reflactive index of silicon and germanium," Optomechanical Technologies for Astronomy, Pts 1 and 2, **6273**, J2732 (2006).

[74] H. H. Li, "Refractive index of silicon and germanium and its wavelength and temperature derivatives," Journal of Physical and Chemical Reference Data **9**, 561–658 (1980).

[75] Y. Franz, "Polycrystalline silicon waveguides for intergrated photonics," Ph.D. thesis, University of Southampton (2018).

[76] L. Shen, "Semiconductor Waveguides for Mid-infrared Photonics," Ph.D. thesis, University of Southampton (2015).

[77] B. Kuyken, P. Verheyen, P. Tannouri, X. Liu, J. Van Campenhout, R. Baets, W. M. J. Green, and G. Roelkens, "Generation of 3.6 μm radiation and telecom-band amplification by four-wave mixing in a silicon waveguide with normal group velocity dispersion." Optics letters **39**, 1349–1352 (2014).

[78] J. W. Choi, B. U. Sohn, G. F. R. Chen, D. K. T. Ng, and D. T. H. Tan, "Broadband incoherent four-wave mixing and 27 dB idler conversion efficiency using ultra-silicon rich nitride devices," Applied Physics Letters **112**, 2–8 (2018).

[79] L. Shen, N. Healy, P. Mehta, T. D. Day, J. R. Sparks, J. V. Badding, and A. C. Peacock, "Nonlinear transmission properties of hydrogenated amorphous silicon core fibers towards the mid-infrared regime," Optics Express **21**, 13075–13083 (2013).

[80] L. Yin and G. P. Agrawal, "Impact of two-photon absorption on self-phase modulation in silicon waveguides," Optics Letters **32**, 2031–2033 (2007).

[81] B. L. Scott and G. R. Pickrell, "Silicon optical fiber diameter dependent grain size," Journal of Crystal Growth **371**, 134–141 (2013).

[82] J. Ballato, T. Hawkins, P. Foy, S. Morris, N. K. Hon, B. Jalali, and R. Rice, "Silica-clad crystalline germanium core optical fibers," Optics Letters **36**, 687–688 (2011).

[83] C. Hou, X. Jia, L. Wei, S.-c. C. Tan, X. Zhao, J. D. Joannopoulos, and Y. Fink, "Crystalline silicon core fibres from aluminium core preforms," Nature Communications **6**, 1–6 (2015).

[84] D. A. Coucheron, M. Fokine, N. Patil, D. W. Breiby, O. T. Buset, N. Healy, A. C. Peacock, T. Hawkins, M. Jones, J. Ballato, and U. J. Gibson, "SiGe-core fibres," Nature Publishing Group **7**, 1–9 (2016).

[85] N. Healy, M. Fokine, Y. Franz, T. Hawkins, M. Jones, J. Ballato, A. C. Peacock, and U. J. Gibson, "CO2 laser-induced directional recrystallization to produce single crystal silicon-core optical fibers with low loss," Advanced Optical Materials **4**, 1004–1008 (2016).

[86] N. Gupta, C. McMillen, R. Singh, R. Podila, A. M. Rao, T. Hawkins, P. Foy, S. Morris, R. Rice, K. F. Poole, L. Zhu, and J. Ballato, "Annealing of silicon optical fibers," Journal of Applied Physics **110**, 0931071 – 0931076 (2011).

[87] N. Healy, J. R. Sparks, P. J. A. Sazio, J. V. Badding and A. C. Peacock, "Tapered silicon optical fibers," Optics Express **18**, 7596–7601 (2010).

[88] H. Ren, "Fiberised silicon photonics for infrared nonlinear photonics," Ph.D. thesis, University of Southampton (2019).

[89] A. D. Bristow, N. Rotenberg, and H. M. Van Driel, "Two-photon absorption and Kerr coefficients of silicon for 850-2200 nm," Applied Physics Letters **90**, 191101–191104 (2007).

[90] Q. Lin, J. Zhang, G. Piredda, R. W. Boyd, P. M. Fauchet, and G. P. Agrawal, "Dispersion of silicon nonlinearities in the near infrared region," Applied Physics Letters **91**, 0211111–0211113 (2007).

[91] A. Felipe, G. Esp, H. J. Kalinowski, A. S. Lima, and A. S. Paterno, "Stepwise fabrication of arbitrary fiber optic tapers," Optics Express **20**, 19893–19904 (2012).

[92] F. Da Ros, E. Porto Da Silva, D. Zibar, S. T. Chu, B. E. Little, R. Morandotti, M. Galili, D. J. Moss, and L. K. Oxenløwe, "Wavelength conversion of QAM signals in a low loss CMOS compatible spiral waveguide," APL Photonics **2**, 1–9 (2017).

[93] E. Stassen, C. Kim, D. Kong, H. Hu, M. Galili, L. K. Oxenløwe, K. Yvind, and M. Pu, "Ultra-low power all-optical wavelength conversion of high-speed data signals in high-confinement AlGaAs-on-insulator microresonators," APL Photonics **4**, 1008041–1008046 (2019).

[94] G. Agrawal, *Highly Nonlinear Fibers* (2013).

[95] A. Trita, C. Lacava, P. Minzioni, J. P. Colonna, P. Gautier, J. M. Fedeli, and I. Cristiani, "Ultra-high four wave mixing efficiency in slot waveguides with silicon nanocrystals," Applied Physics Letters **99**, 1–4 (2011).

[96] V. Eckhouse, I. Cestier, G. Eisenstein, S. Combrié, P. Colman, A. D. Rossi, M. Santagiustina, C. G. Someda, and G. Vadalà, "Highly efficient four wave mixing in GaInP photonic crystal waveguides," Opt. Lett. **35**, 1440–1442 (2010).

[97] M. Hirano, T. Nakanishi, T. Okuno, and M. Onishi, "Silica-Based Highly Nonlinear Fibers and Their Application," IEEE Journal of Selected Topics in Quantum Electronics **15**, 103–113 (2009).

[98] R. L. Espinola, J. I. Dadap, R. M. Osgood, Jr., S. J. McNab, and Y. A. Vlasov, "C-band wavelength conversion in silicon photonic wire waveguides," Optics Express **13**, 4341–4349 (2005).

[99] X. Sang and O. Boyraz, "Gain and noise characteristics of high-bit-rate silicon parametric amplifiers," Optics Express **16**, 13122–13132 (2008).

[100] Z. Wang, H. Liu, N. Huang, Q. Sun, and J. Wen, "Influence of spectral broadening on femtosecond wavelength conversion based on four-wave mixing in silicon waveguides," Applied Optics **50**, 5430–5436 (2011).

[101] Q. Lin, J. Zhang, P. M. Fauchet, and G. P. Agrawal, "Ultrabroadband parametric generation and wavelength conversion in silicon waveguides," Optics Express **14**, 4786–4799 (2006).

[102] X. Liu, "Nonlinear Applications using Silicon Nanophotonic Wires," Ph.D. thesis, Columbia University (2011).

[103] I. Aldaya, A. Gil-Molina, J. L. Pita, L. H. Gabrielli, H. L. Fragnito, and P. Dainese, "Nonlinear carrier dynamics in silicon nano-waveguides," Optica **4**, 1219–1227 (2017).

[104] A. Hosseini, D. Kwong, J. Covey, R. T. Chen, X. Xu, and Y. Zhang, "Ultralow-loss polycrystalline silicon waveguides and high uniformity 1x12 MMI fanout for 3D photonic integration," Optics Express **20**, 21722–21728 (2012).

[105] X. Liu, R. M. O. Jr, Y. A. Vlasov, and W. M. J. Green, "Mid-infrared optical parametric amplifier using silicon nanophotonic waveguides," Nature Photonics **4**, 557–560 (2010).

[106] R. J. Kruhlak, G. K. L. Wong, J. S. Y. Chen, S. G. Murdoch, R. Leonhardt, and J. D. Harvey, "Polarization modulation instability in dispersion-engineered photonic crystal fibers," Optics Letters **31**, 1379–1381 (2006).

[107] S. Shaudhuri, J. R. Sparks, X. Ji, M. Krishnamurthi, L. Shen, N. Healy, A. C. Peacock, V. Gopalan, and J. V. Badding, "Crystalline silicon optical fibers with low optical loss," ACS Photonics **3**, 378–384 (2016).

[108] M. Huang, H. Ren, O. Aktas, L. Shen, J. Wang, T. W. Hawkins, J. Ballato, U. J. Gibson, and A. C. Peacock, "Fiber integrated wavelength converter based on a silicon core fiber with a nano-spike coupler," IEEE Photonics Technology Letters **31**, 1561–1564 (2019).